

2017 NSF/REU

**RESEARCH EXPERIENCE
FOR UNDERGRADUATES
IN PHYSICS**



STUDENT RESEARCH PAPERS

VOLUME 28 PART 1



**REU DIRECTOR
UMESH GARG, PH.D.**

REU Student Research Papers – Summer 2017
University of Notre Dame – Department of Physics

Student	Research Title	Page No.
Joseph Arroyo Illinois Institute of Technology	Testing HECTOR's Efficiency Post Collimator Addition	1
Ariella Atencio Rutgers State University of New Jersey	Studies of Electron Reconstruction for the Track Trigger Upgrade for the HL-LHC	11
Connor Bagwell University of Notre Dame	Accelerator Mass Spectrometry Radiocarbon Dating: Refining the Procedure at the University of Notre Dame	21
Julie Butler Erskine College	Rotational Analysis of Beryllium Isotopes Using JISP16 and Daejeon16 Interactions	31
Bridgette Davey Monmouth College	Developing an Electron Beam Heater for Scanning Tunneling Microscopy	41
Iliana De La Cruz St. Mary's University	Effects of Summer Camp on Participants' Affective Views of Science	49
Lauren Delgado Vassar College	Calculating Electron Drift Velocity & Completing Components of ND Cube	59
Cecilia Fasano University of Notre Dame	PIXE and XRF Analysis of Roman Denarii	71
William Feltman Adrian College	Experimental Determination of the Angular Acceptance of the STrong: Gradient Electromagnetic Online Recoil Separator for Capture Gamma Ray Experiment (St. George) and Observation of Quadrupole Field Reproducibility	81
James Frisby University of Dallas	Energy Resolution Difficulties of the Deep Underground Neutrino Experiment	91
Emmanuel Garcia University of Puerto Rico Maya	Commissioning of a Faraday Cup for the Solenoid Spectrometer for Nuclear Astrophysics (SSNAP)	101
Jazmine Jefferson University of Kansas	Identification of candidate metal-poor stars from the HK survey by pruning with the Gaia DR-1 data release	111
David Kalamarides University of Notre Dame	Determining the Effect of Stellar Evolution on Carbon Abundances	121
Michael Kurkowski University of Notre Dame	Analysis of Colonial Paper Currency	127
Keenan Lambert Chicago State University	The use of RF carpets in Helium gas	131
Joseph Levano University of Notre Dame	MicroMegas Design	141

Biying Liu Xi'an Jiaotong University	Off-line Commissioning and Improvement of the Notre Dame MR-TOF	149
Andrew McEllistrim Univeristy College Cork	The Evolution of Cooperation in Flowing Media	161
Patrick McGuire University of Notre Dame	Using X-Ray Fluorescence (XRF) to Detect Lead in Urban Environments	171
Tyler McMaken Case Western Reserve University	Evidence for Two-Phonon Transverse Wobbling in ^{135}Pr	181
Hannah Olds SUNY College at Oneonta	Particle-Induced Gamma-ray Emission Spectroscopy Over a Broad Range of Elements	191
Allison Olshefke University of Notre Dame	Investigating Implicit Bias in Letters of Recommendation for a High School Physics Camp	203
William Porter University of Notre Dame	Analysis of Phase-Imaging Ion-Cyclotron-Resonance Mass Measurements at Argonne National Lab	213
Cian Roche University College Cork	SN 1992A Progenitor Investigation Through Late Time Light Curve Analysis	221
Anne Stratman University of Notre Dame	Calculating Absolute Transition Probabilities for Nuclei in the Rare-Earth Region	231
Di Tian Xi'an Jiaotong University	A Chemical Perspective of Stars in Dwarf Galaxies & Converting Coordinates	241
Laura Troyer Greenville College	AMS Radiocarbon Dating Wooden Artwork from the Snite Museum of Art	251
John Walker University of St. Thomas	Controlling Electronic States with Strain Engineering	261
Wei Zha Xi'an Jiaotong University	Simulation of an Atmospheric Pressure Plasma Jet via COMSOL	271
Xucheng Zhang Xi'an Jiaotong University	Ferromagnetic Resonance in III-Mn-V Nanostructures	279

Testing HECTOR's Efficiency Post Collimator Addition

Joe Arroyo

Advisor: Anna Simon

2017 NSF REU

Department of Physics, Notre Dame University

I. Introduction:

Various stellar nuclear processes have been widely accepted as being responsible for the creation and relative abundances of nuclides observed in the solar system and distant stars (Burbidge *et al*, 1957). The various burning stages a star undergoes throughout its lifetime are sufficient for the production of all nuclides up to iron. The decrease in binding energy per nucleon of higher mass nuclides prevents further fusion from maintaining hydrostatic equilibrium between gravity and the inner core processes (Bradley W. Carroll, Dale A. Ostile, 2017).

From this point, neutron capture and subsequent β^- decay accounts for many of the heavier stable nuclides. This is broken down into two processes that differ by the timescale of neutron captures. Stellar environments may be dense and hot enough to allow for neutron capture that occurs on time scales longer than the half life of the unstable nuclide that receives the neutron. This is considered slow neutron capture and is given the alias the s-process, as the now $(A + 1)$ nuclide will on average β^- decay before another neutron is captured. In an even more virulent environment, neutrons may bombard nuclides at a rate that is faster than the beta-decay rate. This rapid neutron capture is aptly named the r-process, and subsequent β^- decays from the end process neutron rich isotope fill in the stable larger mass number nuclides. Both of these processes do extremely well predicting the abundances of these nuclides through stellar modelling. (F. Kappeler *et al*, 2010 & M. Mumpower *et al*, 2015)

With neutron rich nuclides well accounted for, there still remains few proton rich nuclides with extremely low abundances. These nuclides are effectively “blocked” by stable nuclides preventing β^- decay to provide a pathway for creation of these rare stable isotopes. As such, a new process must be used to create a model that both forges these nuclides and predicts their relative abundances accurately. A potential candidate is the p-process, sometimes also referred to as the γ -process. This is the process by

which, given a high enough flux of gamma rays, photodisintegration allows for the destruction of nucleons that carve a pathway to the rarer isotopes. Products of the s-process are thought to be the seed nuclides for the p-process. Supernovae are the proposed environment for these seeds due to the large flux of gamma rays. If supernovae were not already difficult enough to model, now all relevant information to the p-process must be taken into account in complex network calculations to arrive at proper relative abundances.

Assisting in an experiment to measure the desired characteristics of certain seed nuclides to feed into these network calculations was the main focus of this project. Cross-section measurements of the (p, γ) channel for ^{102}Pd , ^{108}Cd , and ^{110}Cd were taken during a one week run with a proton beam at Notre Dame's Nuclear Science Lab (NSL) using the FN 10MV Tandem Van de Graaff Accelerator. The High Efficiency Total absorption spectrometer (HECTOR) was used to measure the gamma rays of interest. Part way through the experiment, a tantalum collimator was added to allow for the acquisition of a tighter beam spread and for ease of beam tuning. With the addition of this new component to HECTOR, the efficiency of the high efficiency detector is affected and the effect is unknown. Calibration runs were taken with ^{60}Co with and without the collimator, as well as a known (p, γ) resonance of ^{27}Al . The task during the NSF Notre Dame Physics REU was to analyze this data to determine the effect of the collimator on HECTOR's efficiency.

II. Experimental Methods:

The FN 10MV Tandem Accelerator was used to accelerate a beam of protons towards the targets of interest. A series of bending magnets, quadrupole magnets, and Einzel lenses are tuned to keep the beam current on target and as tight as possible. As the energy of the proton beam is changed throughout the experiment, these must be adjusted to keep the beam tune as tight and on target as possible.

The beam was incident upon targets located at the center of HECTOR. HECTOR measures the gamma rays of interest using 16 4x8x8 inch NaI(Tl) scintillating crystals, each equipped with two photomultiplier tubes (PMT). The segments are arranged to form a cubic array surrounding the target. Energy deposited in each crystal is recorded individually during the experiment and summed up to form one complete spectrum for analysis. This summing procedure requires each PMT to be properly gain matched and calibrated offline in order to make sure gamma ray energies are consistent between each PMT and appear in the proper location on the energy spectrum. The summing of these component spectrums into one sum spectrum allows for nearly 4π steradian coverage of emitted gamma rays with high efficiency.

The measured gamma rays were products of the (p, γ) reactions on ^{102}Pd , ^{108}Cd , ^{110}Cd , ^{27}Al , targets as well as calibration runs with ^{60}Co . Following the week of beam time in the NSL, more data was taken to ensure proper spectrums for ^{60}Co due to inconsistent set up of HECTOR between collimator and no-collimator runs. The inconsistency was different trigger thresholds between runs. This difference in triggering thresholds caused different amounts of the low energy portion of the sum spectrum to be suppressed, causing unwanted artifacts during the analysis of the data.

III. Simulations:

To ensure that the experimental results are consistent with what is expected, Geant4 was used to simulate HECTOR with and without the collimator. Geant4 is used to simulate the passage of particles through matter. For these simulations, gamma rays are sent through the simulated HECTOR and have a chance to be absorbed by the NaI(Tl) crystals and recorded in the output sum spectrum.

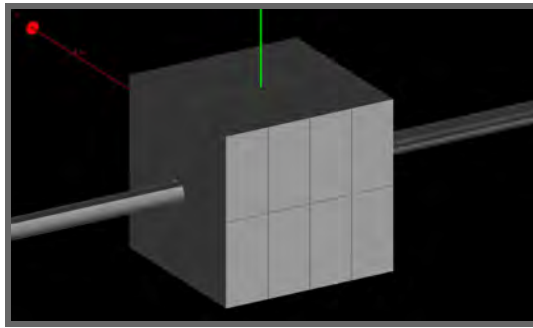


Fig.1 : HECTOR in Geant4

For this project, a detailed collimator was created using boolean object subtraction in Geant4. This is done by defining a base collimator logical volume and borehole logical volumes in the location of boreholes of the collimator. The logical volume is then augmented by successive subtractions in the desired locations to create a tantalum collimator with correct screw holes.

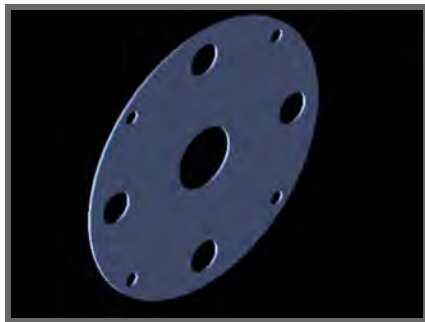


Fig. 2: The completed Collimator

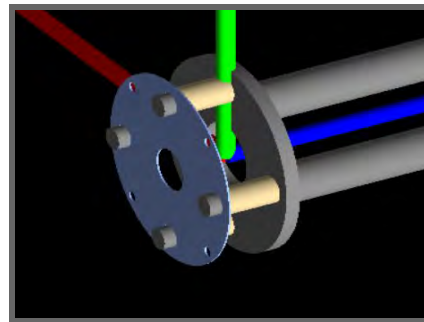


Fig. 3: The Collimator mounted onto the target holder

Stainless steel screws were created using the opposite method, boolean object addition. This was done by fusing together two cylinders, a screw head and a screw body, together. These mount the collimator onto the target holder via ceramic nuts, which were creating using simple cylinders.

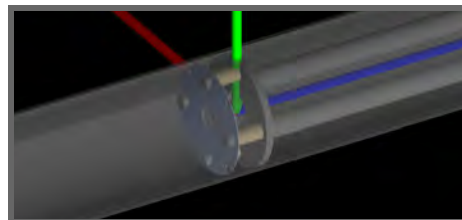


Fig. 4: The collimator in the correct position in the beam pipe.

IV. Analysis:

Analysis of the simulated and experimental data was done using C++ and ROOT, a robust object oriented data analysis framework. To determine the efficiency of the detector, the area under the sum peak of interest must be calculated. This involves elimination of background counts that may bloat the counts of the sum peak and elimination of the Compton Continuum that may skew the sum peak.

Background elimination was achieved by taking background runs near the time of the runs of interest for time lengths sufficient enough to ensure good statistics. From there, scaling of the background was done either by amplitude of the low energy regime in the spectrum or by total recorded charge from the experiment. Amplitude scaling was done for the calibration sources, whereas the resonance was scaled by total recorded charge. Once scaled, subtraction of a background spectrum from a sum peak spectrum is a simple exercise.

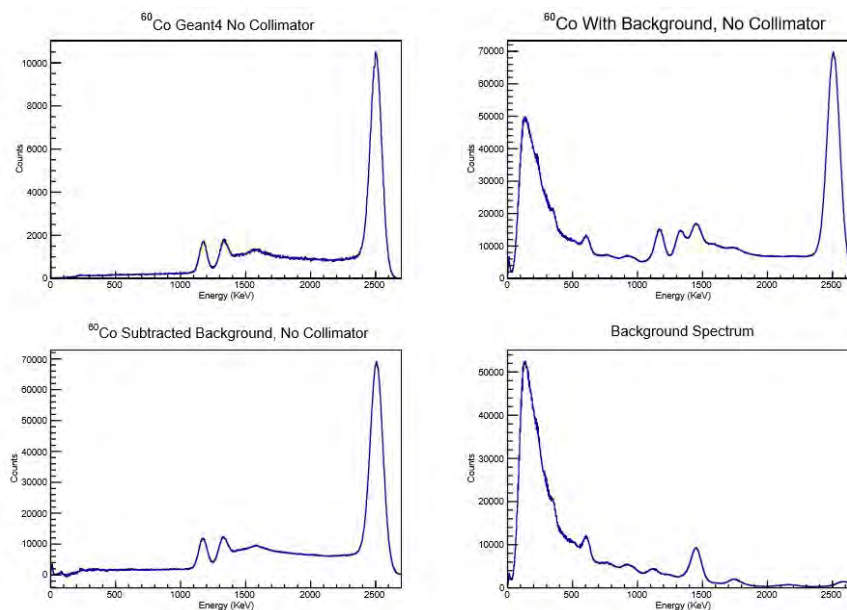


Fig. 5: Background subtraction and comparison with a simulated spectrum

Compton Continuum elimination was achieved by creating a fitting function that first fits a gaussian on the tail end of the sum peak to ignore most of the lower energy Compton component. After

this fit has converged, the best fit for the standard deviation is used as an estimate for the energy width of the secondary fitting routine. This routine fits a linear background, representative of the Compton contribution, and a gaussian atop this background, representative of the actual sum peak, over a $\pm 3\sigma$ region about the first fits sum peak energy. Once this fit has converged, the linear background is subtracted and the histogram's sum peak is integrated over this region to find the number of counts contained in the sum peak.

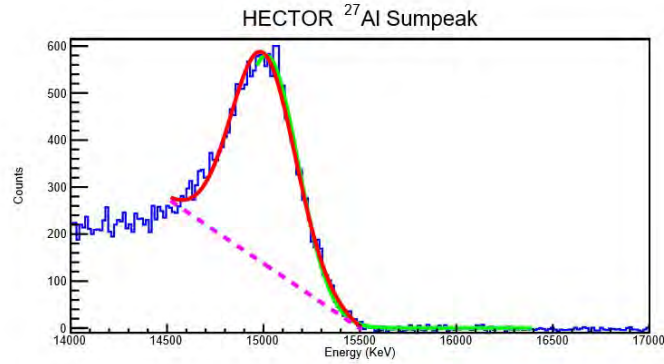


Fig. 6: fitting procedure for an ^{27}Al sum peak resonance. Green shows the initial rough gaussian fit, red is the gaussian and linear background fit, and magenta is the linear background to be subtracted before sum peak integration

An expected value for the total counts must also be calculated to get the efficiency of these runs. For calibration data, this is done by looking at the last known activity measurement and using the half life to calculate the activity of the source the day of the measurements. For the resonance runs, using the expected sum peak yield, the efficiency can be shown to be as follows,

$$\varepsilon = \frac{A_\gamma}{\omega_\gamma \frac{\lambda^2}{2} n}$$

where ε is the efficiency, $A_\gamma = \frac{N_{\text{sumpeak}}}{N_{\text{source}}}$ is the sum peak yield, λ is the de Broglie Wavelength of the beam, ω_γ is the resonance strength, and n is the stopping power of the target material (Christian Iliadis, 2007).

V. Results and Discussion:

The simulated spectra are in a very good agreement with the experimental data. When more closely examining individual sum peaks, it appears that the standard deviation of the simulation does not quite match the experimental data. This can be adjusted by creating a more accurate functional form for the σ function within the Geant4 simulation itself, which generates the spread about sum peaks as a function of the energy of the sum peak. While this slight difference was not a hindrance to the analysis of this project, it is an area of improvement for the simulation as a whole.

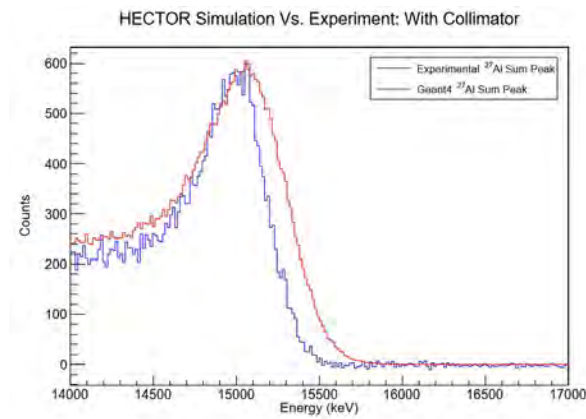


Fig. 7: Simulation vs. Experimental ^{27}Al resonance.
There is a slight difference between the spread of these sum peaks

The change in efficiency between collimator and no collimator for simulation and experiment agrees very strongly. This shows that the addition of the collimator within the simulation was implemented successfully and that there is a good handle on the expected drop in efficiency experimentally, allowing cross-section data that was taken post-collimator addition to be analyzed with confidence.

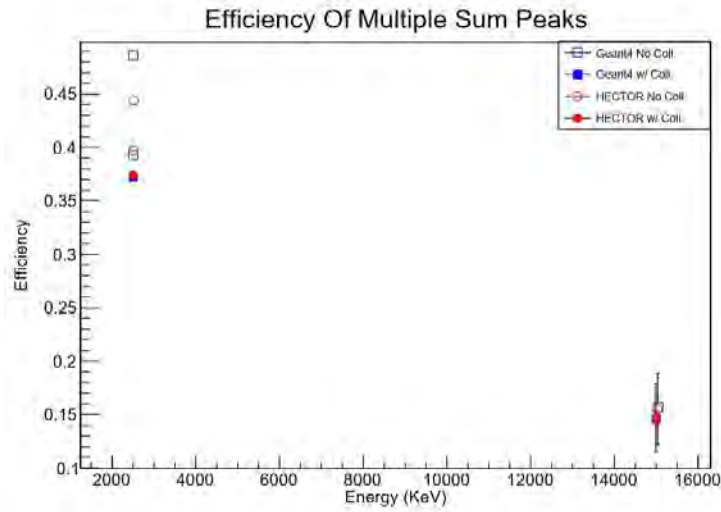


Fig. 8: Efficiency for cobalt (left cluster) and aluminum (right cluster) for simulated and experimental sum peaks.

VI. Conclusion:

The addition of the collimator was successfully implemented and the efficiency calculations between simulation and experiment match strongly. The sources of error on ^{60}Co calibration runs are essentially negligible. The error bars on the ^{27}Al data arise from propagation of error in calculation of the resonance strength from parameters in the efficiency equation. Given the errors, the agreement is well within the $\pm 0.4\%$ discrepancy between most experimental and simulated data. The two outliers with higher efficiency resulted from simulating a ^{60}Co source without the beam pipe in HECTOR. This discrepancy is most likely due to a difference in vertical offset of sources between experiment and simulation. This can be accounted for in the geant for simulation, but that was just outside the allotted time for this project.

This will be useful for analysis to come on cross-section measurements that were taken for (p, γ) channels. Not only was the analysis and simulation improvement a success, it also revealed a few points of improvement within the simulation that may be a component to future REU projects.

VII. References:

1. K. Margaret Burbidge, G. R. Burbidge, William A. Fowler, F. Hoyle. *Synthesis of Elements In Stars*. Reviews of Modern Physics, 29-4 (1957).
2. Bradley W. Carroll, Dale A. Ostlie. *Introduction to Modern Astrophysics, An, 2nd Edition*. Pearson (2007).
3. F. Kappeler, R. Gallino, S. Bisterzo, Wako Aoki. *The s-Process: Nuclear Physics, Stellar Models, Observations*. arXiv:1012.5218v1 (2010).
4. M.R. Mumpower, R. Surman, D.-L. Fang, M. Beard, P. Moller, T. Kawano, A. Aprahamian. *The impact of individual nuclear masses on r-process abundances*. arXiv:1505.07789v1 (2015).
5. Christian Iliadis. *Nuclear Physics of Stars*. Wiley-VCH Verlag GmbH & Co. (2015).

Studies of Electron Reconstruction For the Track Trigger Upgrade For the HL-LHC

Ariella Atencio

2017 NSF/REU Program

Physics Department, University of Notre Dame

Advisors:

Professor Kevin Lannon

Professor Mike Hildreth

26 July, 2017

The world's largest and most powerful particle accelerator, the Large Hadron Collider (LHC) has been running since September of 2008. The LHC consists of a 27 kilometer ring of superconducting magnets with many accelerating structures to boost the energy of the particles along the way. Inside the accelerator, two high energy particle beams travel close to the speed of light and are then collided. The two beams travel in opposite directions in separate beam pipes kept at ultrahigh vacuum. All of the controls for the accelerator are kept at the CERN Control Centre, where the beams inside LHC are made to collide at four locations corresponding to the four particle detectors which are ATLAS, CMS, ALICE, and LHCb. [1]

The LHC smashes groups of protons together near the speed of light. Many of these collisions are just glancing blows but some will be "head on" very energetic collisions. Some of this energy from the collisions is turned into mass in the form of previously unobserved, short-lived particles. This could give clues into how nature behaves at a fundamental level. The CMS is a particle detector and high performance system designed to see a wide range of particles and phenomena produced in high-energy collisions in the LHC, it is particularly good for detecting and measuring muons. The detector has many layers to it, each of which measures all of the different particles, and this data is used to build a picture of events in the heart of the collision. This data is used by Scientists to help answer questions such as: What is the Universe made of? What gives everything substance? The CMS will also be used to measure the properties of previously discovered particles with incredible precision. [2]

There are several layers to the CMS detector. The tracking layer measures charged particles and outside that there are the calorimeters for measuring energy and the muon system for identifying muons. A very strong magnet is used to measure momentum. The higher a

charged particle's momentum, the less its path is curved in the magnetic field. The large magnet allows many layers of muon detectors to use the magnetic field so the momentum can be measured both inside and outside the coil. The "S" in "CMS" stands for solenoid, which refers to the coil of superconducting wire that creates a magnetic field when electricity flows through it. When a collision happens, a particle emerging from the collision first encounters the tracking system which is made up of silicon pixels and silicon strip detectors. This accurately measures the positions of passing charged particles to reconstruct their tracks. Charged particles follow spiral paths in the magnetic field. The curvature of the path reveals their momenta. The particles flying out of the collisions have such high energies that it takes big distances to absorb them. The bigger the detector, the more measurements can be taken in "tracking" the particle, meaning more accuracy in the momentum calculation.

The LHC will soon get an upgrade known as the High-Luminosity Large Hadron Collider (HL-LHC). This upgrade, which should be finished by 2023, will increase luminosity and therefore collisions rate by a factor of ten.. Since the LHC is getting an upgrade, the CMS will also need an upgrade to accommodate the larger number of collisions occurring. If the CMS cannot accurately detect all of the interesting collisions, then the HL-LHC upgrade will be useless. In order to get the most out of this increase in collision frequency, the CMS will need to be able to quickly and accurately sift through the large amounts of data. The trigger (which decides what data to keep) in the CMS currently can't use the tracking information, but using the tracking information in the trigger would be very helpful with managing the higher collision rates. The track trigger we have been working on would work great for muons, but not so much

for electrons. Although we know in principle how to make the trigger work well for electrons, the struggle is in making a practical algorithm that can work in microseconds.

Efficiencies of electrons is significantly worse than muons, with muons at least 95% efficient and electrons sometimes dropping as low as 80% efficient. This is due to Bremsstrahlung radiation and electron scattering. Bremsstrahlung radiation can lead to large discrete energy loss. It is caused by acceleration due to interaction with coulomb field of nuclei. It is the dominant energy loss mechanism for electrons and positrons. Also, light particles like electrons are more deflected by their interaction with atoms in the detector than heavier particles like muons, which is known as electron scattering. Because of the radiation and scattering, stubs aren't where the algorithm expect them to be. So the question is raised, can we recover any of those electrons that aren't reconstructed and improve efficiency? In order to accomplish this we need to find patterns in the missed electron tracks and use them to redesign the tracking algorithm.

A track is a parametric representation of a charged particle's trajectory. Charged particles follow a curved trajectory in a magnetic field due to the Lorentz force. The radius of curvature is inversely proportional to momentum. So, we need to measure the radius of curvature, but radius measurement implies knowing where the particle is at several points along its trajectory. Tracking detectors use ionization of the detector material to register the positions where the particle passes through the detector, allowing a reconstruction of the particle trajectory. The tracking algorithm is explained in detail in reference [3].

The motivation of this project is that electron tracking is worse because of Bremsstrahlung radiation, which causes them to lose momentum, curves more, and as a result

doesn't match the expected pattern. In other words, we can't reconstruct electrons that brem because their stubs don't end up where you'd expect them to be based on a particle that isn't radiating and losing momentum. We tried to study this further by looking at how far the actual electron stubs are away from their expected positions. To check the inaccuracy of the electron tracking, a simulation was used to calculate the actual tracking particle path (giving the location of where the stubs should be) which was compared to where we see the stubs. The main coordinates we use in this comparison are $\Delta r\Phi$ and Δz . $\Delta r\Phi$ is the difference between the actual tracking particle position radius times the angle and the measured stub radius times the angle. Δz is the difference along the path of the CMS detector between the actual tracking particle and the measured stub. These equations are given in the following equations.

$r = \sqrt{x^2 + y^2}$	The variables used in these equations are described as follows:
$\Phi = \arctan(\frac{y}{x})$	x and y are the x,y-coordinates of the stub
$z_{exp} = r * \sinh(\eta) + z_0$	r is the radius of the stub. Φ is the angle of the stub in the x,y plane, z_{exp} is the expected z-coordinate of the stub, eta is the
$R = \frac{p_t}{1.14}$	pseudo-rapidity, and z_0 is the z value for the point along the track
$\Phi_{exp} = \arcsin(\frac{r}{2R}) + \Phi_{tp}$	closest to the center. R is the radius of the track's curvature, p_t is
$\Delta z = z_{stub} - z_{exp}$	the transverse momentum of the tracking particle. Φ_{tp} is the angle
$\Delta r\Phi = r * (\Phi - \Phi_{exp})$	in the x,y plane of the tracking particle. Φ_{exp} is the expected phi value of the tracking particle. Δz is the difference between the z-coordinate of the stub and the expected z-coordinate. $\Delta r\Phi$ is the difference between phi and the expected phi times r.

This approach was validated by looking at muons, whose actual paths were well-represented by their stubs.

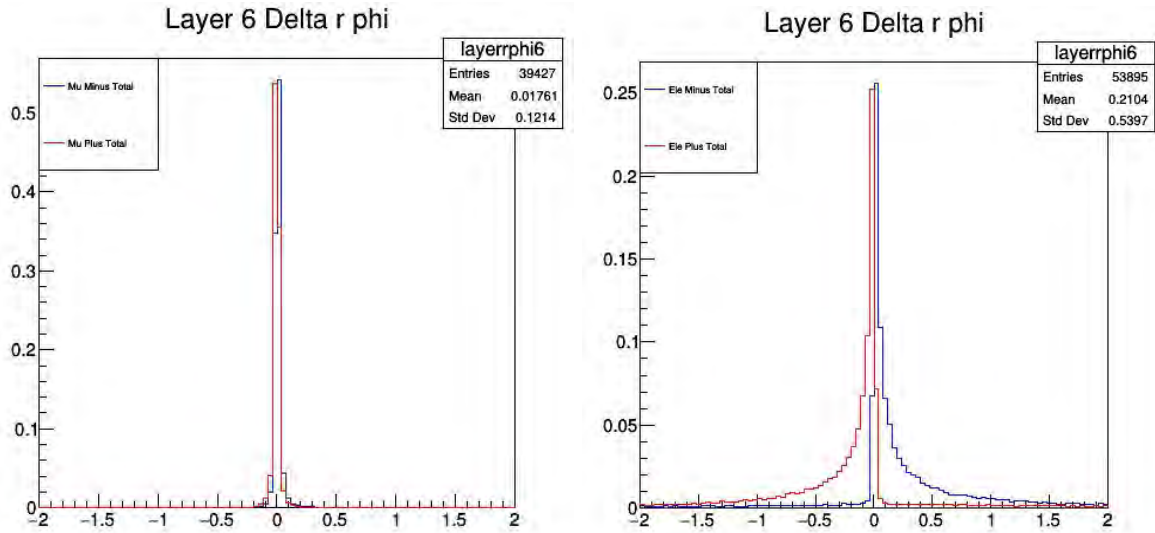


Figure 1.1: Left: $\Delta r\Phi$ for 100,000 events of Muons, in layer 6. Right: $\Delta r\Phi$ for 100,000 events of Electrons, in layer 6.

In histograms for the $\Delta r\Phi$ of muons, they tend to stay close to zero in all layers and for both positive and negative muons. For the same histograms of electrons, however, $\Delta r\Phi$ increases with each layer, with tails going into the positive or negative direction depending on the charge of the electron.

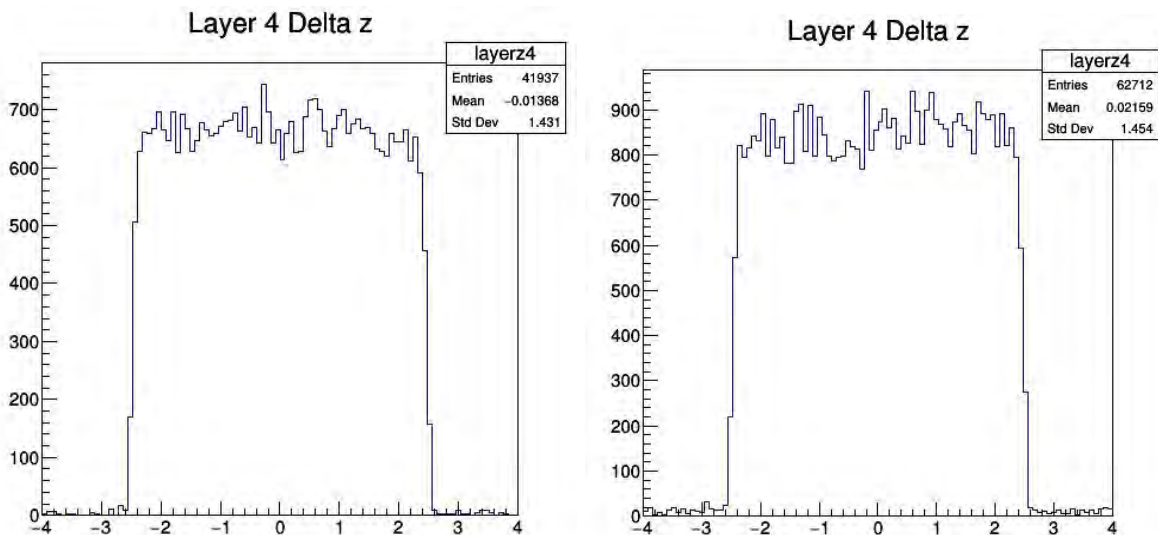


Figure 1.3: On the left, Δz in layer 4 for negative muons. On the right, Δz in layer 4 for negative electrons.

In Δz , both muons and electrons have values in the expected window. This makes sense because Bremsstrahlung radiation only affects the curvature of the tracking particle path in the $\Delta r\Phi$ plane, not in the z direction which the magnetic field does not affect.

One known issue with electrons is that the bremsstrahlung photons can pair convert, creating additional electron-positron pairs that also leave stubs. When a histogram for the number of stubs per event was made, it was discovered that some events had as many as fifty stubs in one track. This was surprising because only about six stubs were expected for each track (one for each layer of the CMS). Also, it was pointed out that the more stubs an event has, the more likely the track is to not be found. So events where the electron track is not reconstructed can be confusing because there could be many stubs. To try to remove that confusion, we focus on only the nearest stub for the rest of the discussion.

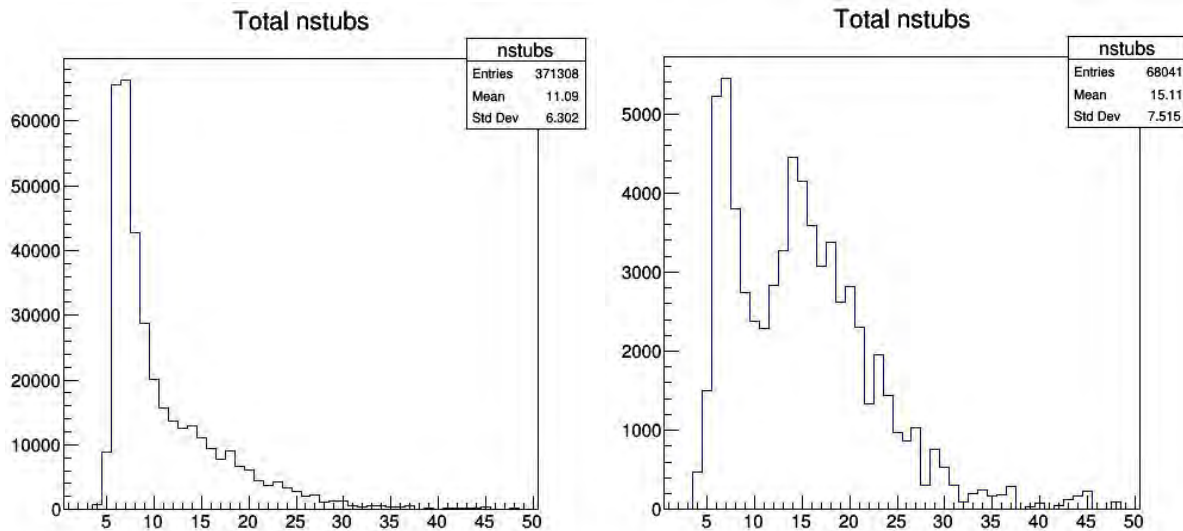


Figure 1.4: On the left, the number of stubs per event for single track negative electrons with 100,000 events. On the right, the number of stubs per event for single track negative electrons with 100,000 events when the track was not found.

Further investigation revealed that in the inner three layers, the stubs are mostly where they're expected, while after that, they are more and more likely to be far away. So the problem is to find the stubs when they're far away from where they're supposed to be.

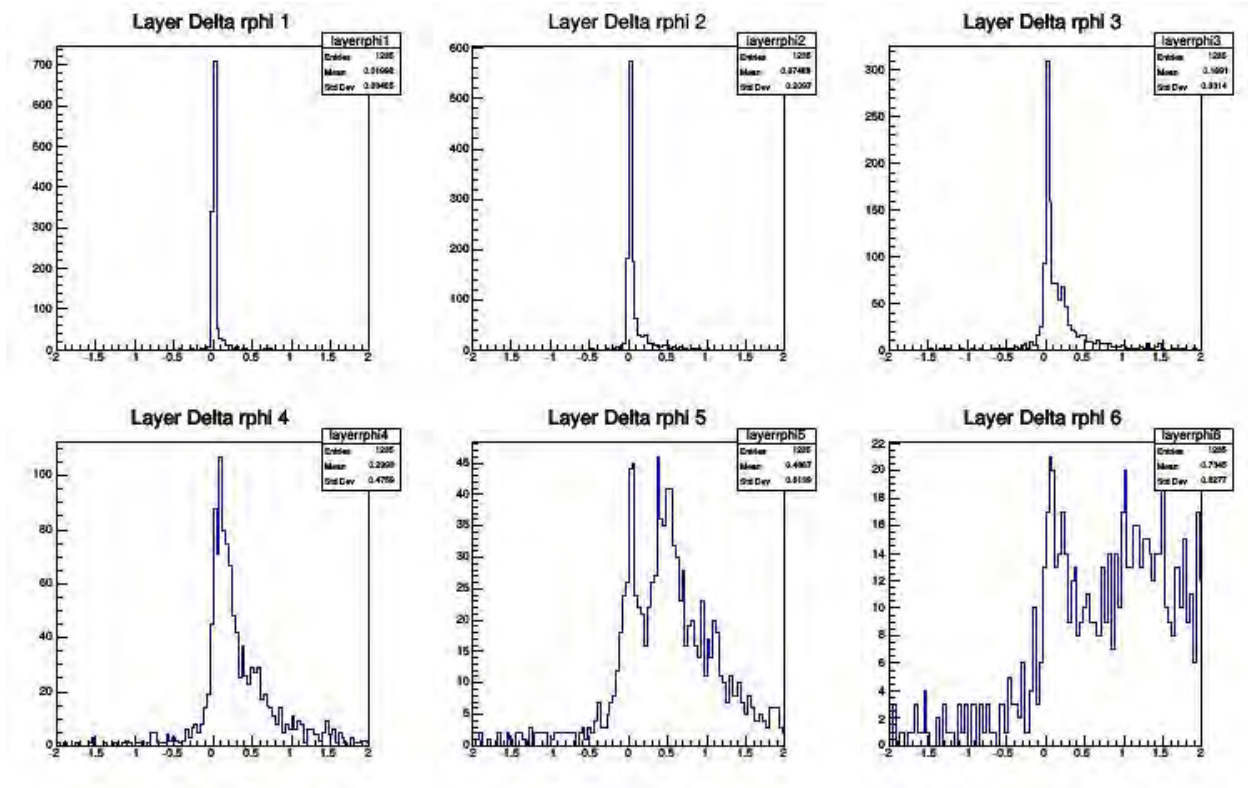


Figure 1.5: Histograms of $\Delta r\Phi$ for single track negative electrons in 100,000 events. These are the data for the stub with the smallest $\Delta r\Phi$ per event when the track was not found. Each histogram represents a different layer of the CMS.

In two-dimensional histograms comparing the $\Delta r\Phi$ of one layer to the next, we see a correlation across layers.

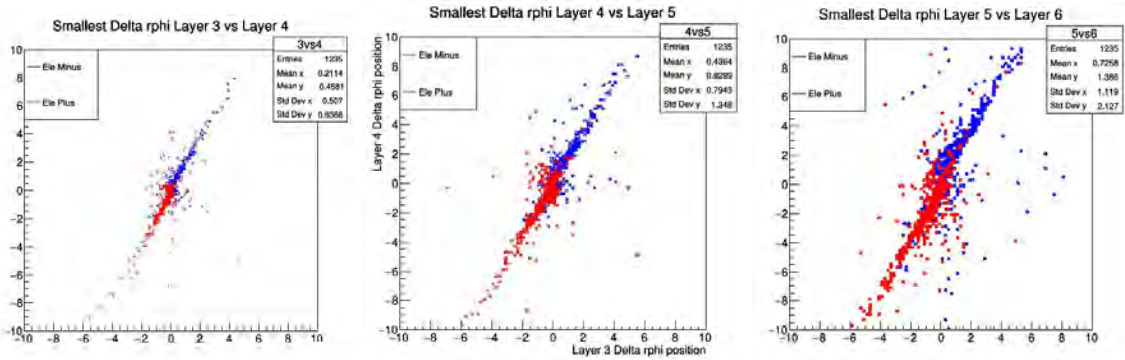


Figure 1.6: Two-dimensional histograms of $\Delta r\Phi$. To the left: layer 3 on the x-axis versus layer 4 on the y-axis for single track negative electrons in 100,000 events. In the center: Layer 4 vs Layer 5, and to the right: Layer 5 vs Layer 6. This is the data for the stub with the smallest $\Delta r\Phi$ per event when the track was not found.

When the stubs are off target, they're off target in a way that is correlated between layers. So, if someone told you how far off you are in layer 3, you should be able to determine how far off the next stub will be in layer 4. Perhaps, this pattern could be used to re-write the tracking algorithm.

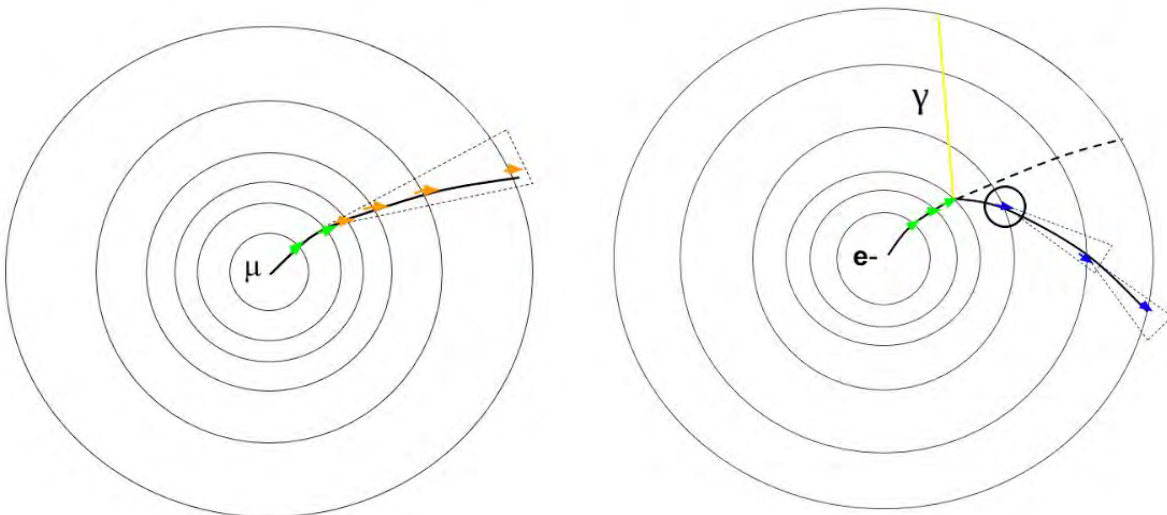


Figure 1.6: On the left, a cartoon depicting the current setup for the tracking algorithm. On the right, a cartoon representation of a hypothetical tracking system that could correct for Bremsstrahlung radiation.

Rather than simply widening the window of possibilities for the next stub, perhaps the tracker could use the most recent stub to change the position of the window so that it might look more

accurately for the next stub. If the window is more accurately positioned, more electron tracks could be found even if they Bremsstrahlung radiate.

The algorithm suggested above would definitely work in theory, but it may not be practical. The next steps in this research will be to explore whether there is a feasible way to implement this algorithm that would work for the trigger.

References

[1] “The Large Hadron Collider” *CERN, Accelerating Science*

<http://home.cern/topics/large-hadron-collider>

[2] Lucas Taylor “What is CMS?” 2011-11-23, <http://cms.web.cern.ch/news/what-cms>

[3] Ben Cote and Patrick Shields “Feasibility Studies For the Proposed CMS L1 Track Trigger Upgrade” August 5th, 2016

Accelerator Mass Spectrometry Radiocarbon Dating:

Refining the Procedure at the University of Notre Dame

Connor Bagwell

University of Notre Dame, Department of Physics

Research Experience for Undergraduates

28 July 2017

Principal Investigator:

Professor Philippe Collon

Coauthors:

Tyler Anderson, Adam Clark, Austin Nelson, Michael Skulski, Laura Troyer

Abstract

Accelerator Mass Spectrometry (AMS) is a highly sensitive technique for measuring trace isotopic ratios, making it perfectly suited for radiocarbon dating. AMS radiocarbon dating deviates from decay activity measurements, which measure isotopic decay activity in a sample over time and are unable to measure extremely low isotopic abundances, such as ^{14}C to stable carbon (10^{-12} or lower), without taking prohibitively large samples or periods of time. AMS uses minute sample sizes, making the technique much less destructive.

The use of an entire accelerator system to discriminate from background is orders of magnitude more sensitive in small samples than both decay activity measurements and traditional mass spectrometry methods [1]. AMS measures the specific number of events of ^{14}C detected from the beams of both unknown graphitized carbon and known standards and calculates the number of total carbon ions from the beam current. The isotopic concentration of the sample is then calculated from this set of measurements, and the measured concentrations are calibrated with known historical concentration data, producing date ranges and associated probabilities for that sample [2]. The Smithe Museum of Art provided the AMS group with samples from five wooden art pieces as the unknowns to be graphitized and measured.

The Technique: Accelerator Mass Spectrometry

Accelerator Mass Spectrometry (AMS) is referred to as the “needle in the haystack method” because it deals with detecting trace isotopes amongst a spread of more abundant isotopes. These isotopes, often radioactive, are measured in ratios of 10^{-10} to 10^{-16} [3]. In the case of radiocarbon dating, ^{14}C is the isotope of interest and has an isotopic ratio to stable carbon of 10^{-12} . These less abundant isotopes require entire accelerator systems to discriminate from background noise and unwanted contaminations, since accelerators offer numerous, highly sensitive adjustments that can be tuned to detect only the nuclide of interest.

AMS begins with some sample to be measured, inherently comprised of many different elements and isotopes, and attempts to measure the current isotopic ratio of interest. The technique incorporates several

methods of filtration to differentiate between desired counts and background noise. The 11 MV FN tandem accelerator and AMS beamline at the University of Notre Dame's Nuclear Science Laboratory (NSL) was used for these experiments. The FN incorporates several magnets, an electrostatic analyzer, and a Wein filter to reduce isobaric contaminants, making it suitable for measuring several long-lived isotopes [4].

AMS applications are many and diverse. Nuclear forensics, for example, measures the distribution of isotopes for the elements known to be used in nuclear weaponry manufacturing or as the byproduct of nuclear bomb reactions [5]. There exists a natural distribution of unstable isotopes, and if the measured distribution is found to be significantly different than that natural distribution, governments can identify those parties in violation of disarmament treaties. Additionally, nuclear reactor accidents can be studied using AMS to discover future warning signs and hidden failures [5]. In biomedical research, the highly sensitive measurements using AMS are used to detect the effects of micro-doses of man-made radioisotopes during tests for new drugs [5]. In archaeology, calcium dating is an attractive frontier of AMS research, which would allow researchers to date events beyond the human-scale of activity, measured by radiocarbon dating [5]. Further applications extend to astrophysics, glacial changes, atmospheric data, and numerous others.

AMS Radiocarbon Dating

One of the most useful applications of AMS is radiocarbon dating, which relies on the carbon life cycle. The atmosphere contains a broad mixture of elements, of which carbon is the fourth most abundant. The most abundant element is nitrogen, of which most is stable ^{14}N . Thermal neutrons created from cosmic ray interactions collide with ^{14}N to create ^{14}C , as shown in the following reaction:



Figure 1 A nitrogen-14 atom reacts with an incoming neutron in the atmosphere to produce carbon-14 and a proton.

The ^{14}C eventually beta decays back into ^{14}N , releasing an electron and an antineutrino.

Carbon dioxide in the air, containing a ratio of ^{14}C to stable carbon isotopes, is absorbed by plants, undergoing isotopic fractionation. Isotopic fractionation, stated simply, says that heavier isotopes of an element will undergo chemical processes slower than lighter isotopes [6]. During photosynthesis, for example, there is a higher uptake of ^{12}C than ^{13}C . The carbon then either continues to build in the plant or is eaten by an animal or other consumer. The animal not only takes in carbon by consuming, but also by breathing. The moment of death of an organism is the point at which the radiocarbon clock starts; this is time zero. The organism is no longer taking in any new carbon and therefore equilibrates with the environment.

The idea is that while alive, the organism, be it a tree, a bug, or an animal, has roughly the same isotopic ratios of carbon as the atmosphere, to within a correction [1]. At time zero, the organism is no longer equilibrating with the environment, and its distribution of carbon isotopes will be set, while the radioactive carbon isotopes will begin to decay away from this atmospheric concentration [1]. Using the exponential decay law and a thorough set of known historical atmospheric concentration data, one can calculate the age of the sample in question.

A set of historical concentration data has been collected and published by the scientific community for reference and use in calibration curves for dating purposes [5]. The input to the calibration is the measured concentration of ^{14}C to stable carbon (^{12}C and ^{13}C), in the form of units called fraction of modern (F_{14}) [7]. F_{14} refers to the fraction of ^{14}C at present to the ^{14}C on 1 January 1950, the universally accepted “modern” concentration of ^{14}C to stable carbon [6]. Measurements made since then have added to the data set past “modern” levels, and precise measurements of samples from trees with well-defined ages, given by their tree rings, allow this precise atmospheric concentration data to reach back well past 1950 [6]. The calibration software used in these experiments was OxCal, the radiocarbon calibration tool developed by the Oxford Radiocarbon Accelerator Unit [2].

Graphitization: From Carbon Based Life to Coal

The most effective form of carbon to use in an accelerator system is pure graphite [7]. Graphitization is the process of forming ideally pure graphite from a source of carbon. In the case of this experiment, the carbon came from the wood shavings from internal samples of the art pieces. The process can be broken down simply into the following steps: treatment of the iron matrix, combustion and transfer of the sample, reduction of carbon dioxide to carbon monoxide, and graphitization of carbon monoxide to graphite. The pressure versus time chart of the process is outlined in Figure 2.

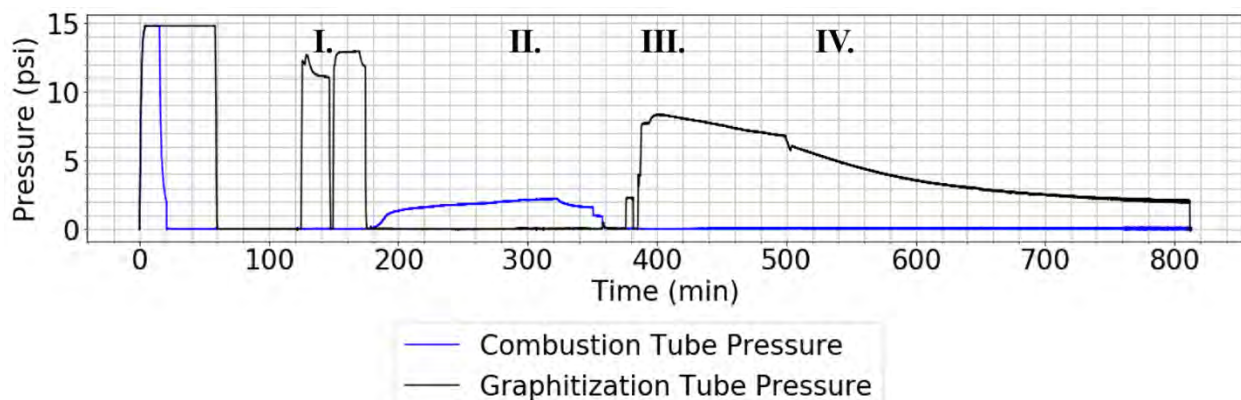


Figure 2 The standard pressure reading throughout the graphitization process, including readings from two pressure gauges: the combustion tube and the iron treatment and graphitization tube.

I. Treatment of the Iron Matrix:

The carrier for the graphite is an iron matrix, 2-3 mg of iron powder. The iron is oxidized at atmosphere using an oven at 900 °C, then baked at vacuum, each for 30 minutes. The iron is then treated twice with 12.3 psi of hydrogen, 15 minutes a piece, at 815 °C, until the iron is brilliantly light in color, as shown in Figure 3. A liquid nitrogen cold finger is applied to the system to draw out any water vapor.

II. Combustion and Transfer of the Sample:

Combustion of the sample releases carbon dioxide, which is captured and chemically reduced to graphite. A measured 3.6 mg of wood

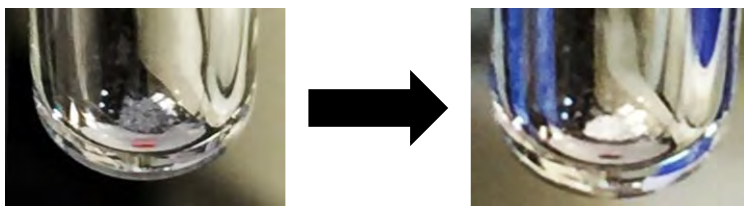


Figure 3 The iron undergoes two hydrogen treatments, resulting in a lighter and brighter colored iron matrix in the isolated system.

sample is combusted in a quartz tube for an hour with 480 mg of copper oxide. The copper oxide is the source of oxygen in the combustion which is heated to 900 °C. The leftover oxygen produced by the copper oxide

reduces back onto the copper until the pressure levels off. The gas produced by combustion is then transferred through a water trap of ethanol and dry ice slush mixture, through which water freezes and carbon dioxide passes. The transfer is made by a temperature gradient to the graphitization tube, where the treated iron matrix is sitting. The temperature difference is created by placing liquid nitrogen over the graphitization tube, which is cold enough to freeze the carbon dioxide. Once pressures level off, the graphitization tube is sealed and the carbon is now in dry ice form, as seen in Figure 4. The remaining gases are pumped away before continuing.



Figure 4 From left to right, wood shavings from the artwork, carbon dioxide crystals in the graphitization tube, and carbon dioxide condensed on the sides of the graphitization tube.

III. Reduction

A ratio of 2.3:1 of hydrogen to carbon dioxide pressure is added to the system. The first stage of graphitization chemically reduces carbon dioxide to carbon monoxide, by the reaction in Figure 5.



Figure 5 Carbon dioxide and hydrogen gas reduce to carbon monoxide and water.

The oven is set to 915 °C, at which point the reduction takes place. The reaction continues for 90 minutes with the ethanol and dry ice slush mixture on the cold finger. By the end of this process, ideally, the carbon dioxide will have reduced to carbon monoxide, without creation of methane, and the water will have been trapped in the cold finger.

IV. Graphitization

In the second stage of graphitization, the following reaction dominates:

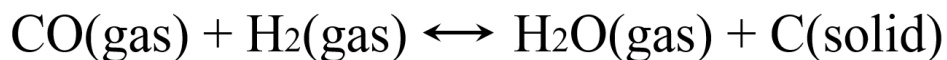


Figure 6 Carbon monoxide and hydrogen gas reduce to water and graphite, the latter of which embeds itself into the iron matrix.

The oven is set to 600 °C and liquid nitrogen is placed around the cold finger to freeze any methane and water created or residual carbon dioxide. This final stage takes roughly six hours to fully react, during which time the graphite embeds within the iron matrix. The final product is a black powder comprised of graphite and iron.

The 11 MV FN Tandem Accelerator

The samples are loaded into aluminum sample holders, called cathodes for the function they serve in the ion source. The cathodes are then loaded into a forty-cathode wheel, and mounted in the source of negative ions via cesium sputtering (SNICS) chamber. Cesium is heated to form a gas and coats the electrostatic plates in the chamber. During heating, the cesium releases its loose electrons, and the cesium becomes positively charged. The cesium accelerates towards the cathode, collides, and produces singly charged negative ions of carbon. These carbon ions accelerate toward and past the electrostatic plates coated in positively charged cesium into the accelerator. The ion's path is outlined in Figure 7.

The accelerator system sorts first by kinetic energy in the electrostatic analyzer (ESA), requiring the kinetic energy of an ion of ^{14}C accelerated from the SNICS to pass. The beam is sorted by mass in the SNICS magnet, using the principle of the Lorentz force. The particles are accelerated through the main tank and stripped of electrons using a carbon foil. The carbon occupies a distribution around the +3 charge state, i.e., the carbon ions are missing, on average, three electrons. So, the beam passes through the analyzing magnet to select only the +3 charge state. In the target room, the beam passes through a Wien filter, utilizing the Lorentz principle and only allowing past the particles with the

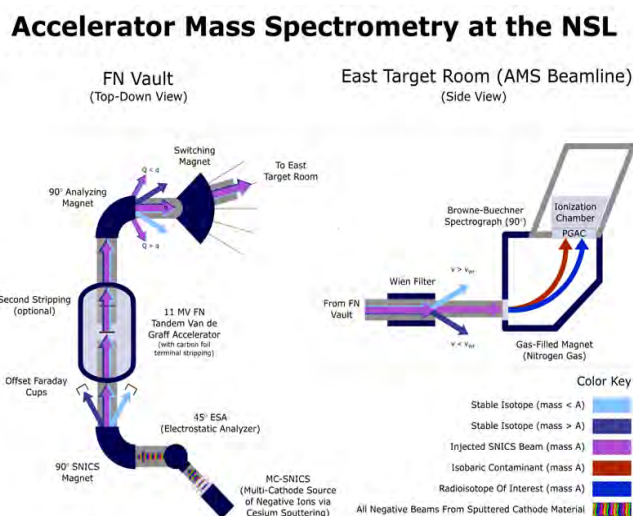


Figure 7 The NSL FN tandem accelerator, AMS beamline, filtration techniques, and parallel grid avalanche counter (PGAC) outlined.

correct velocity, calculated from the desired charge and mass. The particles finally hit the parallel grid avalanche counter (PGAC) and ionization chamber, which detect the events of ^{14}C . At this point, AMS measurements would typically employ an ionization chamber, which forces the beam to collide with a gas and, on average, take on different charges based on the number of protons within the isotope. This filtration technique allows one to sort out isobaric contaminations, which would have successfully passed through the discrimination methods. One major benefit of AMS radiocarbon dating is that ^{14}C does not require this last filter since its isobar, ^{14}N , cannot form negative ions in the SNICS to begin with.

Data & Conclusion

Table I: African Art Date Ranges, 20 July 2017

Sample	Graphitization Date	Probability	Run-Averaged Age Range	Probability	Time-Averaged Age Range
Museum 1	July 6, 2017	95.4%	848 BC - 1085 AD	95.4%	866 BC - 1067 AD
	June 28, 2017	79.5%	Pre-1893	79.5%	Pre-1893
		15.9%	1906-1954	15.9%	1906-1954
Museum 2	July 2, 2017	32.0%	1664-1787	34.5%	1664-1787
		48.0%	1791-1958	50.8%	1790-1958
		15.4%	Post-1987	10.1%	Post-1990
	June 29, 2017	35.1%	1664-1788	34.9%	1664-1788
		51.1%	1789-1958	50.8%	1789-1958
Museum 3	July 8, 2017	9.2%	Post-1990	9.7%	Post-1990
		16.9%	1957-1962	16.0%	1957-1962
		78.5%	1979-2006	79.2%	1979-2007
			0.2%	2008	
	July 8, 2017	95.4%	1882 BC - 265 AD	95.4%	1914 BC - 232 AD
Museum 4	June 20, 2017	95.4%	1199 BC - 914 AD	95.4%	1151 BC - 964 AD
	July 10, 2017	95.4%	Pre-1655	95.4%	Pre-1655
		July 1, 2017	43.2%	Pre-1669	54.5%
Museum 5	July 12, 2017	38.8%	1781-1798	40.9%	1783-1796
		13.5%	1945-1951		
		4.2%	1681-1738	3.6%	1681-1738
	0.2%	1745-1748	0.4%	1755-1762	
		0.7%	1750-1763		
June 26, 2017	10.2%	1802-1938	8.8%	1803-1937	
	12.5%	1802-1938	13.3%	1952-1962	
	67.6%	Post-1976	69.4%	Post-1976	
	95.4%	1262	95.4%	2241 BC - 477 BC	

Table I Data collected from the accelerator run made on 20 July 2017 and processed through the OxCal calibration software to output date ranges and associated probabilities for the five pieces of African Art.

The results from the data obtained from the 20 July 2017 University of Notre Dame NSL FN tandem accelerator run are shown in Table I, laid out by museum piece, separated into the multiple graphitizations produced for each sample. The raw data obtained consisted in part of ^{14}C events and both run-average and

time-average beam current, which are used to calculate the raw measured concentration. This concentration is normalized with our measured standards, giving us a corrected concentration, which, after corrections outlined in Donahue [8] for isotope fractionation, allows for the calculation of fraction modern. The OxCal software takes this input, fits the data along its calibration curve comprised of historical isotopic concentration data, and outputs the calibrated date ranges with their associated probabilities, a product of their “wiggles fitting” program [2].

Easily seen is the magnitude of error in this data set, rendering the date ranges inconclusive. The intent of the summer research was to continue improvements upon and refinements to the graphitization process at the University of Notre Dame. The amount of beam current achieved in July 2017 (10^1 microamps) was two orders of magnitude higher than the original attempts at graphitizing wooden samples in the NSL (10^2 nanoamps). This improvement was brought about by several changes made to the process. The AMS group doubled the hydrogen treatments to the iron matrix to two, began graphitizing on the same day as the iron was treated, allowing the oxygen to react with the copper after combustion to reoxidize into copper-oxide, increasing the duration of transferring gas after combustion, and improving lab discipline regarding note keeping for future use of information on lab procedures and trials.

This AMS group will further refine the procedure until the NSL is able to replicate significant results in radiocarbon dating. AMS requires extreme precision and sensitivity in the four principles of AMS defined in Synal [9] as the suppression of nuclear isobaric ions, suppression of equal mass molecules, provision of sufficient abundance sensitivity, and establishment of reliable normalization procedure, which are key to any AMS measurement technique.

Acknowledgements

The REU at Notre Dame is funded by the National Science Foundation. My summer would not have been possible without the generosity and financial aid of the Department of Physics. In cooperation with

ISNAP, JINA-CEE, and Notre Dame physics faculty, the ND AMS group brought this humble author through the principles of AMS, making me a passable amateur nuclear physicist. Special thanks to the graduate students Tyler Anderson, Adam Clark, Austin Nelson, and Michael Skulski for showing me how brilliant Notre Dame graduate students are. To my colleague, Laura Troyer, for learning with me the whole way. And to my advisor, Professor Philippe Collon, for guiding and encouraging me these last two years.

References

- [1] Kutschera, Walter. *Applications of accelerator mass spectrometry*. International Journal of Mass Spectrometry, 349-350 (2013) 203-218.
- [2] OxCal, Oxford Radiocarbon Accelerator Unit. *Radiocarbon Calibration*.
<https://c14.arch.ox.ac.uk/calibration.html>
- [3] Litherland, A. E. *Ultrasensitive Mass Spectrometry with Accelerators*. Annual Review of Nuclear Particle Science, 1980.30 (1980) 437-473.
- [4] Bowers, Matthew R. *A Study of ^{36}Cl Production in the Early Solar System*. University of Notre Dame (2013).
- [5] Kutschera, Walter; Michael Paul. *Accelerator Mass Spectrometry in Nuclear Physics and Astrophysics*. Annual Review of Nuclear Particle Science, 1990.40 (1990) 411-438.
- [6] Stenström, Kristina Eriksson; Göran Skog, Elisavet Georgiadou, Johan Genberg, Anette Johansson. *A Guide to Radiocarbon Units and Calculations*. Lund University (2011).
- [7] McNichol, A.P.; A.J.T. Jull. *Converting AMS Data to Radiocarbon Values: Considerations and Conventions*. Radiocarbon, Vol. 43, 313-320 (2001).
- [8] Donahue, D.J.; T.W. Linick, A.J.T. Jull. *Isotope-Ratio and Background Corrections for Accelerator Mass Spectrometry Radiocarbon Measurements*. Radiocarbon, Vol. 32, No. 2. (1990) 135-142.
- [9] Synal, Hans-Arno. *Developments in accelerator mass spectrometry*. International Journal of Mass Spectrometry 349-350 (2013) 192-202.

Rotational Analysis of Beryllium Isotopes Using JISP16 and Daejeon16 Interactions

Julie Butler

2017 NSF/REU Program
Physics Department, University of Notre Dame

ADVISOR: Mark A. Caprio

July 28, 2017

Abstract

Rotational bands emerge in *ab initio* no core configuration interaction (NCCI) calculations in several beryllium isotopes. This is shown by rotational patterns in excitation energies, electromagnetic moments, and electromagnetic transitions as functions of the angular momentum. In order for NCCI calculations to correctly describe the nucleus, the NCCI calculation must be based on a realistic nucleon-nucleon interaction. The nucleon-nucleon interaction JISP16 has been previously used to calculate the rotational bands in beryllium isotopes. However, a new nucleon-nucleon interaction, Daejeon16, has been shown to provide more accurate ground state energies of light nuclei. This research compares the ability of the two nucleon-nucleon interactions, JISP16 and Daejeon16, to describe rotational bands of the beryllium isotopes ${}^7\text{Be}$, ${}^8\text{Be}$, and ${}^9\text{Be}$. For each isotope and interaction, rotational bands are determined using a range of basis parameters to determine which interaction yields rotational band parameters which most closely match experimental values. Various methods of extrapolation are used to determine converged values of rotational band parameters.

Introduction

Ab initio no-core configuration interaction (NCCI) calculations are used to identify rotational bands in p-shell nuclei. These rotational bands are identified by rotational patterns in energies, electromagnetic moments, and electromagnetic transitions as functions of angular momentum.¹ NCCI calculations are able to calculate properties of many light nuclei with masses up to $A = 16$.² In order for the NCCI calculation to accurately describe the nucleus, it must be based on a realistic nucleon-nucleon interaction. Two such nucleon-nucleon interactions are known as JISP16 and Daejeon16. This paper will compare the ability of both JISP16 and Daejeon16 to calculate the rotational bands in the beryllium isotopes ${}^7\text{Be}$ and ${}^8\text{Be}$. The dependence of rotational bands on the NCCI calculation parameters $\hbar\omega$ and N_{max} is also explored. In order to determine the accuracy of each nucleon-nucleon interaction, rotational band parameters are extracted and compared to experimental results. Various extrapolation techniques are utilized to attempt to estimate the rotational parameters of converged calculations for the rotational bands.

Nucleon-Nucleon Interactions

J-matrix Inverse Scattering Potential, JISP16, is a nucleon-nucleon interaction which been proven to be successful in describing light nuclei, since it was fit not only to nucleon-nucleon scattering data, but also to the binding energies of nuclei with three or more nucleons. However, the fit for JISP16 was performed in 2006, using bases which are small compared to the bases used today. In addition, JISP16 has been found to be less accurate for nuclei with more than twelve nucleons and some exotic, light nuclei, which are far from the $Z = N$ line.² Daejeon16 is a new nucleon-nucleon interaction. It was constructed in a similar way as JISP16, but has more accurate fitting to nuclear binding energies. This is due to the use of extrapolation techniques in the fitting. Daejeon16 appears to have a faster convergence than JISP16 and is also able to achieve the same precision in binding energy with a smaller bases set when compared to JISP16. Daejeon16 also appears to be better able to calculate the binding energies and excitation energies of light nuclei.²

Background on Rotation

A rotational band is made of nuclear states which have the same intrinsic state, but differing angular momentum, J . Within a rotational band, the angular momentum values are greater than or equal to the angular momentum projection along the intrinsic symmetry axis.¹

When energy is plotted against total angular momentum, rotational bands emerge. These rotational bands follow certain patterns with respect to energy. The following equation can be used to describe energy as a function of angular momentum.¹

$$E(J) = E_0 + A[J(J + 1)] \quad (1)$$

In the above equation, A is known as the rotational constant, which is inversely related to the moment of inertia of the intrinsic state. For bands where $K = 1/2$, there is a Coriolis contribution to the kinetic energy, which causes staggering in the rotational band. For $K=1/2$ bands, the above equation is modified with a Coriolis decoupling parameter, a , which reflects the staggering in energy with respect to angular momentum.¹

$$E(J) = E_0 + A[J(J + 1) + a(-1)^{J+1/2}(J + 1/2)] \quad (2)$$

In NCCI calculations, the many-body Schrödinger equation is formulated as Hamiltonian matrix diagonalization problem.³ The Hamiltonian is represented with respect to a basis of antisymmetrized products of single-particle states, typically harmonic oscillator states. Due to computational limitations, NCCI calculations are carried out in truncated space, defined by the maximum number of allowed oscillator excitations, N_{max} . Convergence to exact results could be obtained by increasing N_{max} . However, computational limitations place limits on the maximum accessible value of N_{max} . Because of this, the calculated results depend not only on the length parameter b for the oscillator basis function, typically specified by the oscillator energy $\hbar\omega$, but also on the basis truncation N_{max} .^{2,3}

Extrapolation Methods

Due to computational limitations, NCCI calculations must be carried out in truncated space. This limits the convergence of the results. Converged results can be estimated using various methods of extrapolation. Though these extrapolation methods are still in their formative stages, two of these methods, exponential extrapolation and infrared extrapolation, are explored in this paper to estimate the converged energies for the ground and excited states of the beryllium nuclei.

Table 1: The two extrapolation schemes explored in this research: exponential extrapolation and infrared extrapolation.

Exponential Extrapolation ³	Infrared Extrapolation ^{4,5,6}
$E(N_{max}) = c_0 + c_1 e^{-c_2 N_{max}}$ Converged Energy: c_0	$\Lambda_{UV} = [2(N_{max} + 3/2)]^{1/2}(\hbar/b(\hbar\omega))$ $b(\hbar\omega) = \hbar c / [(m_N c^2)(\hbar\omega)]^{1/2}$ $L_2(N_{max}, \hbar\omega) = [2(N_{max} + \Delta N_{max} + 3/2)]^{1/2} b(\hbar\omega)$ $E(L) = E_\infty + a_0 e^{-2k_\infty L}$ Converged Energy: E_∞

For each nucleon-nucleon interaction, the optimal UV cutoff can be determined from the N_{max} and $\hbar\omega$ values that were used to fit the data. The UV cutoff of the JISP16 interaction was estimated to Ref. [4] to be approximately $800 \text{ MeV}/c$, obtained from the fact that the JISP16 interaction was fit using data obtained from $N_{max} = 8$ and $\hbar\omega = 40 \text{ MeV}$.⁴ Dajeon16 was fit with data obtained at a $\hbar\omega$ value of 25 MeV , so its UV cutoff will be lower than the

UV cutoff of the JISP16 interaction. UV cutoffs of $550\text{MeV}/c$ and $800\text{MeV}/c$ are explored in this paper.

Results

NCCI calculations were performed with both the Daejeon16 and JISP16 nucleon-nucleon interactions using the code MFDn.^{7,8}

Rotational bands become evident in the beryllium isotopes when the energy of the ground and excited states are plotted as a function of angular momentum, denoted by J . The angular momentum axis is scaled as $J(J+1)$. Figure 1 shows these rotational plots for the beryllium isotopes ${}^7\text{Be}$ and ${}^8\text{Be}$, with the JISP16 interaction.

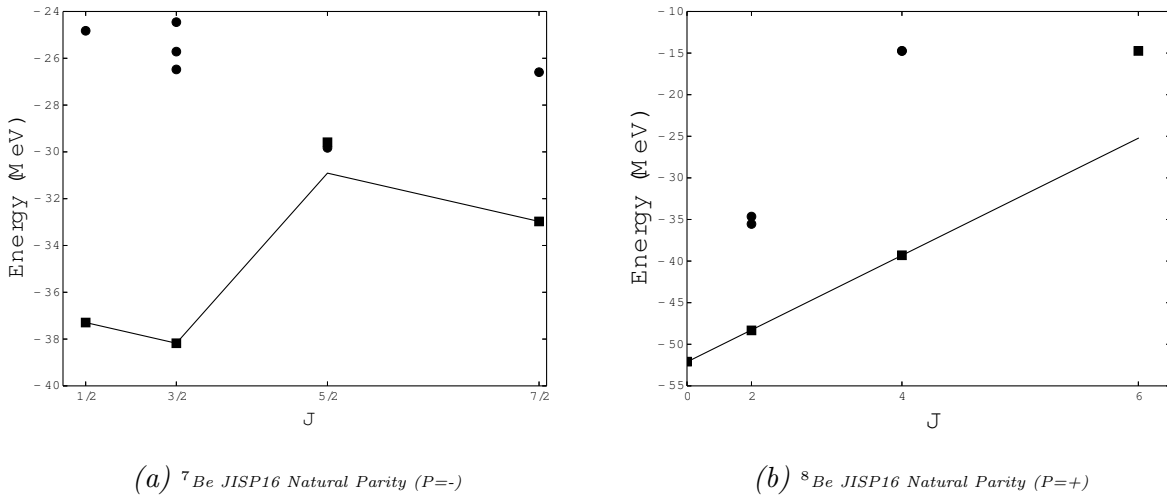


Figure 1: Energy eigenvalues obtained for states in the natural parity and unnatural parity spaces for ${}^7\text{Be}$ and ${}^8\text{Be}$. Energy is plotted as a function of angular momentum, scaled as $J(J+1)$ to allow for identification of rotational energy patterns. Square symbols represent band member candidates. Plots shown here were made with results obtained using a $\hbar\omega$ of 20MeV and an N_{max} value of 8.

The yrast band for Beryllium-7 and Beryllium-8 are shown above in Figure 1. The yrast band generally connects the lowest energies with respect to different angular momentum values. As shown above, the yrast band of Beryllium-7 is staggered, indicating that it has a non-zero Coriolis decoupling parameter, which will be used later in determining the rotational band parameters.

Candidate band members are identified visually using the plots shown above. The band

members are confirmed through analysis of electromagnetic quadrupole moments; members of the same rotational band have electromagnetic quadrupole moments of similar magnitude and sign. For example in the Beryllium-7 plots shown above in Figure 2, for both JISP16 and Daejeon16, the first $J=5/2$ state visually appears to be the band member. However, the second $J=5/2$ state has an electromagnetic quadrupole moment which more closely matches the moments of the other three candidate band members. Therefore, the second $J=5/2$ state was chosen as the band member for Beryllium-7.

There appears to be little difference between the yrast bands calculated with the two different nucleon-nucleon interactions, but there are slight difference in energy. The band members calculated with the Daejeon16 interaction are typically lower in energy than the corresponding band member calculated with the JISP16 interaction, calculated at the same N_{max} and $\hbar\omega$ values. This could indicate that the Daejeon16 interaction has a faster convergence than the JISP16 interaction, or that the Daejeon16 interaction predicts lower values for the energies.

Due to computational limitations, NCCI calculations must be carried out in truncated space. Due to this, the value of the calculated energies depends on the truncated, and thus, on the value of N_{max} . Shown below in Figure 2(a) and Figure 2(b), the yrast band of ^8Be is shown, calculated using both the JISP16 interaction, in Figure 2(a), and the Daejeon16 interaction, in Figure 2(b). In each plot, the yrast band is shown as calculated using four different values of N_{max} , ranging from $N_{max} = 4$ to $N_{max} = 10$. In addition, the figures also show the results of the extrapolated band members in attempts to calculate the converged energies of the band members. The results of three different exponential extrapolations are shown, as well as the results from two different infrared extrapolation.

As N_{max} increases, the ground state energy and the excitation energies decrease, eventually appearing to converge. However, even at an N_{max} value of 10, the highest value of N_{max} explored in this paper, the energies do not appear to be converged. The rotational bands calculated using the JISP16 interaction have a wider spread when rotational bands from successive N_{max} values are plotted. This appears to indicate that the Daejeon16 interaction has faster convergence with respect to N_{max} .

The three exponential extrapolations are tightly clustered near what appears to be the

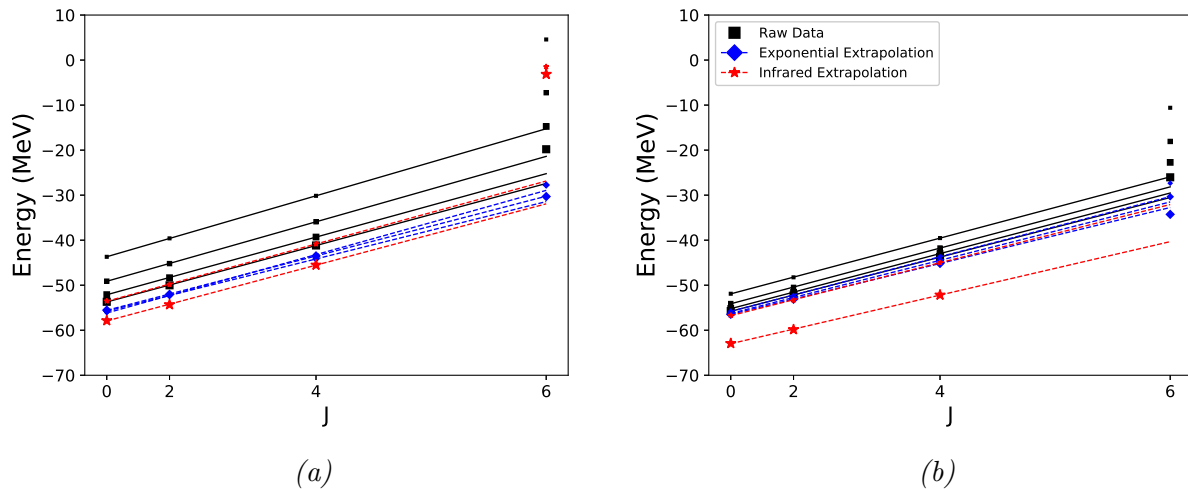


Figure 2: The above figures demonstrate how N_{max} and the energy of the rotational bands are related. All calculations were performed $\hbar\omega = 20$. the figures depict the yrast rotational band of beryllium-8, with the JISP interaction on the left and the Daejeon16 interaction on the right.

converged value in both interaction. In addition, for both interactions, exponential extrapolations using larger N_{max} values bring the energy of the $J=6$ point lower, bringing it closer to lying on the rotational band.

The infrared extrapolations on the rotational bands calculated using the JISP16 interaction are not closely spaced, both with respect to each other and with respect to the exponential extrapolations. The $\Lambda_{UV} = 800 \text{ MeV}/c$ is expected to be the proper UV cutoff for an infrared extrapolation with JISP16. The rotational band extrapolated with a UV cutoff of $800 \text{ MeV}/c$ lies lower than the rotational bands calculated with the exponential extrapolations. This indicates that either the infrared extrapolation is overestimating the energy of the rotational band, or the converged energy of the rotational band is lower than the exponential extrapolations predict. For the rotational bands calculated using the Daejeon16 interaction, the infrared extrapolation calculated using a UV cutoff of $550 \text{ MeV}/c$ is expected to predict the converged energy. This appears to be correct, as the rotational band calculated with the infrared extrapolation lies just below the energies predicted by the exponential extrapolations. The $\Lambda_{UV} = 800 \text{ MeV}/c$ extrapolation does not appear to be the best method of extrapolation for rotational bands when the Daejeon16 interaction is used.

The yrast bands for both beryllium isotopes are fit using the equations described in the

introduction. From these fits, the band parameters E_0 , A are extracted. In addition, the Coriolis decoupling parameter, a , is extracted from Beryllium-7. These parameters can be compared to experimental values to determine how accurately NCCI calculations with the two nucleon-nucleon interactions can calculate the rotational bands. The fits are performed using only the three band members with the lowest energies. For Beryllium-7, these states occur at $J = 1/2$, $J = 3/2$, and $J = 7/2$. For Beryllium-8, the three lowest energy band members occur at $J = 0$, $J = 2$, and $J = 4$. Fits are performed both on the raw rotational bands and on the extrapolated rotational bands. Figure 3 shows the evolution of the band parameters with both N_{max} and $\hbar\omega$. The band parameters extracted from the exponential extrapolations are shown offset from the raw data, and the band parameters extracted from the infrared extrapolation is shown with dashed lines. Experimental band parameters are shown with solid lines for comparison.^{9,10}

All three band parameters appear to have both a $\hbar\omega$ dependence and a N_{max} dependence, as indicated by the curved shapes of the raw data points within an N_{max} , and the convergence of band parameters within a $\hbar\omega$. There appears to be less variance with N_{max} in the band parameters calculated using the Daejeon16 interaction. This indicates that Daejeon16 has a faster converge than JISP16 with respect to N_{max} , at least within Variances in the band parameters between N_{max} for the Daejeon16 interaction do occur, but at high values of $\hbar\omega$. This is possibly due to the fact that Daejeon16 was fit using data calculated at $\hbar\omega = 25\text{MeV}$. For Beryllium-7, the rotational bands generated using the Daejeon16 interaction were fit with E_0 and A values that more closely matched experimental values. The only exception are the E_0 and A fit parameters calculated using an infrared extrapolation with $\Lambda_{UV} = 800\text{MeV}/c$. Here, the rotational bands calculated using the JISP16 interaction had E_0 value that more closely matches the experimental value. As seen above, an infrared extrapolation using a UV cutoff of $800\text{ MeV}/c$ does not appear to work well with Daejeon16 rotational bands. This same pattern with E_0 and A hold for Beryllium-8. JISP16 more accurately calculates the Coriolis decoupling parameter, when compared to the rotational parameters calculated using the Daejeon16 interaction. Though both interactions predict a value that is nearly double the experimental value.

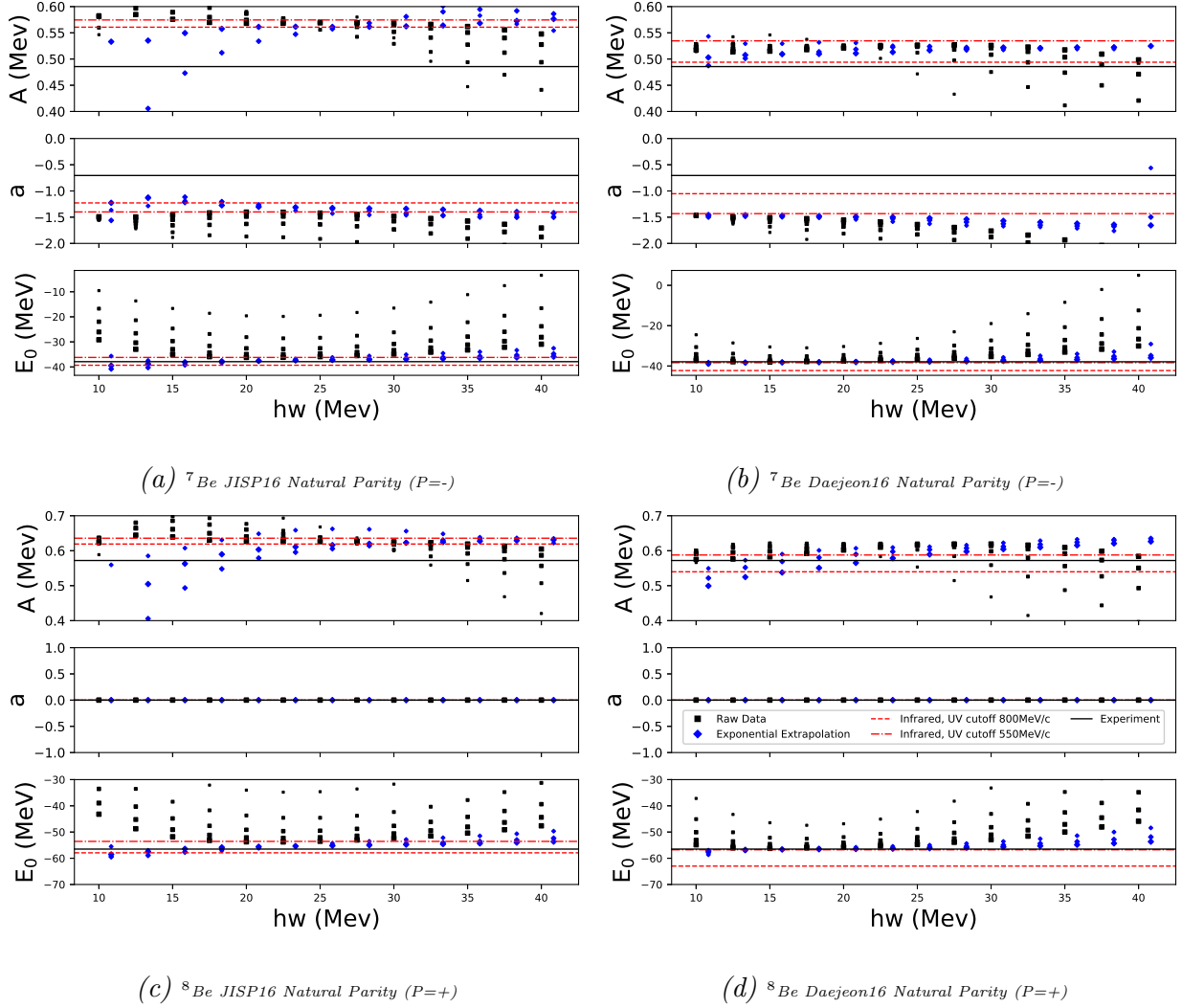


Figure 3: The above graphs analyze the dependence of the rotational band parameters on both $\hbar\omega$ and N_{max} . Beryllium-7 is depicted on the top row and Beryllium-8 is shown on the bottom row. Daejeon16 band parameters were calculated at $\hbar\omega = 25\text{MeV}$ and JISP16 band parameters were calculated at $\hbar\omega = 40\text{MeV}$. The $\hbar\omega$ values were chosen at the variational minimum for each interaction.

Conclusion

In summary, the Daejeon16 interaction causes more rapid convergence of rotational bands with respect to N_{max} . In addition, both exponential and infrared extrapolations appear to be able to more accurately estimate the converged rotational bands when the rotational bands are calculated the Daejeon16 interaction. The rotational band parameters, E_0 and A , extracted from rotational bands calculated from the Daejeon16 interaction more closely

match experimental values then those calculated from the JISP16 interaction. In addition, the application of extrapolation methods bring the band parameters even closer to the experimental values. However, the Coriolis decoupling parameter, a , is better calculated using the JISP16 interaction. However, both interactions predict a Coriolis decoupling parameter that is roughly double the experimental value.

Acknowledgements

Supported by the US DOE under Award Nos. DE-FG02-95ER-40934, DESC0008485 (SciDAC/NUCLEI), and DE-FG02-87ER40371 and the US NSF under Award No. NSF- PHY05- 52843. Computational resources provided by NERSC (US DOE Contract DE-AC02- 05CH11231) and the Notre Dame Center for Research Computing. Patrick Fasano, Anna McCoy, and Valentino Constantinou are thanked for the assistance in this research. Some of the data used in this research was calculated by James Vary and Pieter Maris, who are gratefully thanked for their permission to use the data.

References

1. M.A. Caprio, P. Maris, J.P. Vary, and R. Smith, *Int. J. Mod. Phys. E.* 25, 1541002 (2015).
2. A.M. Shirokov, I.J. Shin, M. Sosnkina, P. Maris, and J.P. Vary, *Phys. Lett. B.* 716, 87 (2016).
3. P. Maris, M.A. Caprio, and J.P. Vary, *Phys. Rev. C.* 91, 179 (2015).
4. Ch. Constantinou et al. In preparation. arXiv:1605.04976.
5. P. Maris, J. P. Vary, and A. M. Shirokov *Phys. Rev. C* 79, 014308 (2009).
6. R.J. Furnstahl, G. Hagen, T. Papenbrock, and K.A. Wendt, *J. Phys. G. Nucl. Part. Phys.* 42, 034032 (2015).
7. P. Maris, M. Sosonkina, J. P. Vary, E. Ng, and C. Yang, *Procedia Comput. Sci.* 1, 97 (2010).
8. H. M. Aktulga, C. Yang, E. G. Ng, P. Maris, and J. P. Vary, *Concurrency Computat.: Pract. Exper.* 26, 2631 (2013).
9. P. Maris and J.P. Vary, *Int. J. Mod. Phys. E.* 22, 1330016 (2013).
10. P. Maris, M.A. Caprio, and J.P. Vary, *Phys. Rev. C.* 91 (2015) 014310.

Developing an Electron Beam Heater for Scanning Tunneling Microscopy

Bridgette Davey

2017 NSF/REU Program

Physics Department, University of Notre Dame

Advisor: Morten Eskildsen

Abstract

Scanning Tunneling Microscopy is using a high resolution instrument to image a sample surface at an atomic level. An electron beam heater (e-beam heater) is an instrument that utilizes beams of electrons to heat a source target. Electron beam heaters have specific application in scanning tunneling microscopy which include tip and sample preparation. An ongoing project exists to engineer an electron beam heater to remove tip contamination, assist in sample preparation, and allow for the removal of protective oxide layer often used when moving samples from one institution to another.

Introduction

Scanning tunneling microscopy includes the process of taking real-space images on an atomic scale. Scanning tunneling microscopes make it possible to take the image of a sample as well as get the electrical properties provided the insulating layers are thin enough to permit electron tunneling [1]. The physics behind STM involves electron tunneling. In this case electrons tunnel through a medium (vacuum between the tip and sample being measured) that in classical mechanics they would otherwise be unable to [2]. With STM microscopes a tip, or very thin wire, that is conducting is brought very close to a surface to be examined. A bias is then applied between the sample and the tip. This bias is what allows electrons to tunnel through the space between the two, hence the term electron tunneling. This stream of electrons tunneling between the tip and the sample is known as the tunneling current. Tunneling current is a function of the applied voltage, tip position, and local density of states of the sample [3]. The current

between the tip and the sample is measured and converted into an image as the tip scans across the surface of the sample.

An electronic beam heater is an instrument that uses a stream of electrons to heat a source object. There are two main types of electron beam heater [4]. One operates purely through passing a current directly through the sample being heated and the other operates through thermionic radiation from a filament close to the sample holder. In both cases resistive heating is utilized. An electron beam heater using a filament has been built in this case due to the conductive nature of the samples. A large amount of current is required to heat the samples due to the very low resistance.

Application

There are two common problems in the field of scanning tunneling microscopy that an electron beam heater addresses. One is sample contamination and another is tip contamination.

Tips are usually made from Tungsten, Gold, or Platinum-Iridium. Inside the lab the tip is created through an electrochemical etching method. A mixture of potassium hydroxide is used with a voltage of 4 volts running through it. The tip is coated in a plastic material and submerged in the solution just beneath the top of the plastic. The solution will then etch away at the metal until it drops to the bottom of the beaker and a sharp “tip” has formed. The tip is covered by a thin native oxide layer that needs to be removed in order to maintain stable tunneling conditions inside the STM [4]. Heating the tip using an electron beam heater removes the oxide layer. Tips may also become contaminated from transferral from the air into the vacuum chamber. An

electron beam heater can remove these contaminants that would otherwise interfere in taking current measurements.

Another application of an e-beam heater is in the preparation of a sample. Samples may become contaminated as well through exposure to air or by other means. In order to prevent this many samples are coated in a protective oxide layer when being transported from one facility to another. Placing the sample on an electron beam heater and heating it to the appropriate temperature removes this protective coating.

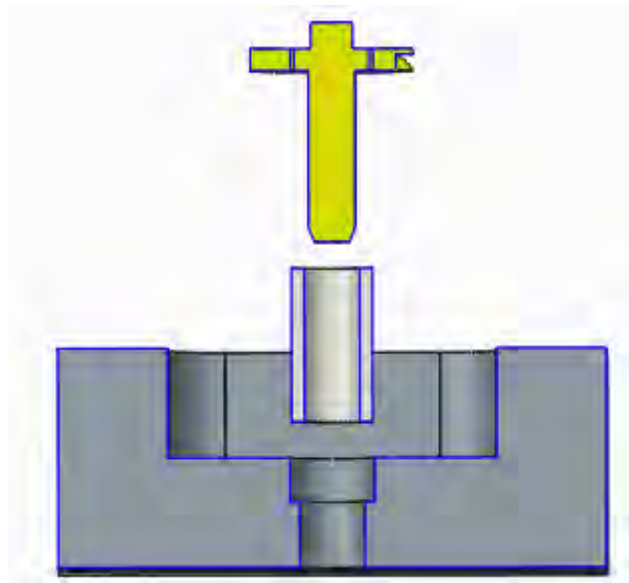
Design

The current working model of the electron beam heater is shown below.



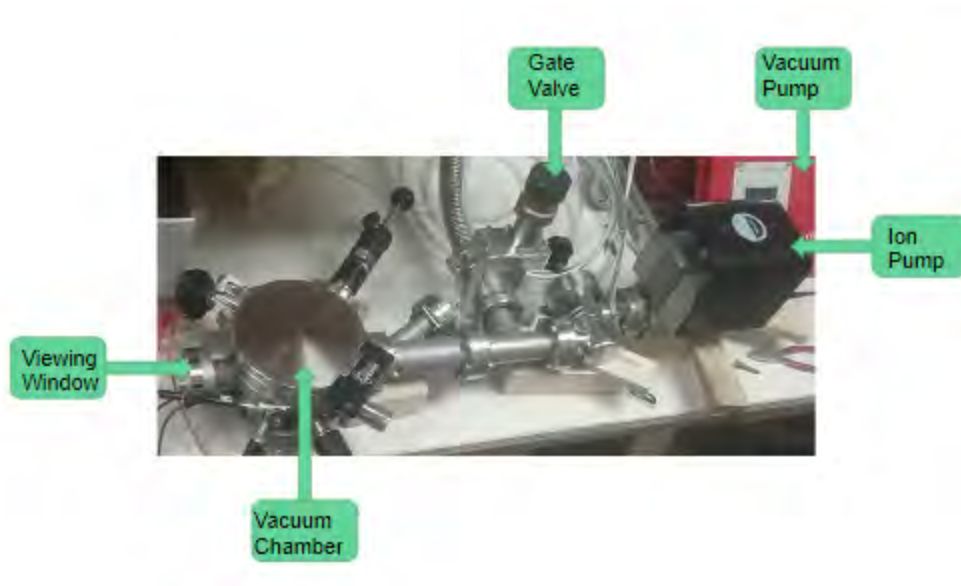
A stainless steel block is provided as the base. The entire electron beam heater is inside of a cavity in the base. This is to allow for a cover to be slipped over top with just the sample holder sitting above it to further force the electrons from the filament to the sample holder. The filament is made out of tungsten wire and is arranged in the path it is to allow for the maximum amount of coils and consequently the maximum length of wire. The electron beam heater uses the concept of Ohm's Law, Power equals current squared times resistance. The greater the length of wire the more resistance there is. A greater resistance leads to a lower current being needed to reach the same thermionic emission from the filament.

A potential difference is applied between the filament and the sample holder. The kinetic energy of the electrons generated is used to heat the sample holder. The electrons are generated through resistive heating the filament itself instead of the other type of electron beam heater which involves running a current directly through the sample. These electrons are attracted to the sample holder and fly into it and deposit kinetic energy as heat.



As the previous diagram illustrates, the sample holder is mounted on a ceramic tube to both prevent the holder from touching the base and prevent the holder from falling through a hole cut for a connection point for the high voltage line.

Testing



The first step in testing the current electron beam heating design is mounting the instrument inside of a vacuum chamber as it will have to function under vacuum conditions. The layout of the system used to test it is shown above. A viewing window exists to the side of the chamber to provide visual contact. The combination of the vacuum and ion pump can bring pressure inside the vacuum chamber down to 10^{-7} mbar.

After the heater is mounted inside of the vacuum and connected through the ports in the side to the ground, voltmeter, and high voltage line the vacuum is pumped down to a minimum

of 10^{-6} mbar. Once pumped down a current is applied to the filament with a voltage of 1000 volts running through it. The filament begins to glow (as we have in fact created a lightbulb, a tungsten filament in vacuum). The sample holder itself only begins to heat up when high voltage has been turned on as can be demonstrated in the images below.

High Voltage Off



High Voltage On



Further Steps

Developing an electron beam heater is an ongoing process. Some aspects to take into consideration in the future are trying to get the current even lower to attain the same heating capabilities it has now at 1000 volts. One possibility would be in using a different type of wire with a similar melting point to tungsten. A wire such as stainless steel is relatively useless as it would melt almost instantly. Another possibility is trying a thinner wire with the same parallel path and working to get more wire length through a greater number of spirals. Eliminating the screws and finding a way to hold the filament up with just the tungsten wire would also be ideal as the screws are giant heatsinks. All in all an electronic beam heater is a useful instrument in addressing three problems in scanning tunneling microscopy: tip contamination, sample preparation, and removing protective packaging on samples.

Acknowledgements

I wish to thank my advisor Dr. Morten Eskilden and graduate students Allan Leishman and David Green for working with me this summer. I have learned a great deal this summer that without their support and seemingly unending patience would have been impossible. I would like to thank David Green specifically for teaching me how to use Creo Parametric and working with/giving me the background knowledge to design a helium recovery system. I wish to thank Allan Leishman specifically for working with/giving me the background knowledge to work on designing the e-beam heater. Last but certainly not least I would like to thank Dr. Umesh Garg for the impossibly wonderful chance to do an REU and research here at Notre Dame, and Lori Fuson and Nell Collins for program coordination.

References and Notes

1. Binnig, G., & Rohrer, H. (1983). Scanning Tunneling Microscopy. *Surface Science*, 126(1-3), 236-244.
2. Binnig, G., & Rohrer, H. (2000). Scanning Tunneling Microscopy. *IBM Journal of Research and Development*, 44(1), 279-293.
3. Julian Chen, C. (1993). *Introduction to Scanning Tunneling Microscopy*. Oxford University Press. 0-19-507, 150-6.
4. Ding, H. F., et al. (2005). Electron-beam Tip/sample Heating Device for a Scanning Tunneling Microscopy. *Review of Scientific Instruments* 76.12, 123703.
5. Behrisch, R. (1981). *Sputtering by Particle Bombardment*. Berlin, Springer. Vol 1.

EFFECTS OF SUMMER CAMP ON PARTICIPANTS' AFFECTIVE VIEWS OF
SCIENCE

Iliana De La Cruz

2017 NSF/REU Program

Physics Department, University of Notre Dame

ADVISOR: Dr. Micha Kilburn

ABSTRACT

There exists a movement to draw more diverse groups of students to science, technology, engineering, and math (STEM) careers with recent data suggesting students select STEM tracks as early as high school with influence starting as early as middle school. Yet, limited research exists on K-12 students and how their affective views of science are influenced by outreach. This research quantitatively examines the effect of a summer camp on participants' affective views of science by age, gender, and career aspirations. Camp participants were offered a survey at the beginning and end of each week long camp asking them to rate how much they like art, science, math and engineering, their career aspirations, and which words they associate to science or art from a predetermined list. Researchers analyzed four years of these programmatic surveys seeking any relation between words associated to participants' age, gender, and career aspirations. This summer, researchers also interviewed camp participants to further understand their perspectives during the survey and word associating process to evaluate the effectiveness of the survey itself. Preliminary statistical analysis suggests the camp significantly affects participants' career choice with regard to STEM careers. Interview results also highlighted points of confusion in younger students and different interpretations of words amongst older students, which can be used to redesign the survey instrument to better assess the effect of the camp experience.

Keywords: informal education, outreach, affective views, word associations, science summer camp

1 Introduction

Since 2011, the Joint Institute for Nuclear Astrophysics, Center for the Evolution of Elements (JINA-CEE) has sponsored the “Art 2 Science Summer Camp” hosted at the University of Notre Dame. Camp intended to introduce students from ages 8-12 to science they would not usually see in the classroom via a variety of art forms and creative experiments and to instill a greater sense of hands-on science. Art 2 Science hosts approximately 100-180 student participants, 25 teenage junior counselors, 12 adult counselors, and 15 adult activity leaders throughout one week. Students submit applications and are accepted until reaching maximum occupancy and camps fees are based on a sliding scale according to household lunch fees.¹ At the start of camp participants are asked to complete anonymous surveys with the option to not fill one out, this action is repeated at the end of the camp as well. The pre-camp survey asks for the participant’s gender, career aspirations, preferred school subjects, rate on how much they like art, science, math, and building things on a scale of 1-10, and to circle words that sound like science or triangle words that sound like art or both. The post survey is identical but also asks participants to rate activities. Dates of birth, are utilized only for matching pre-post and are deleted afterwards to maintain anonymity.

Data was collected from pre and post surveys over the 2013-2016 summers and recorded in an Excel sheet. Using software such as Root and Excel to populate comparative histograms and statistical analysis we questioned:

1. Do students have a significantly more favorable view of science after camp?
2. What defines a favorable view of science?
3. Does there exist a significant relation between words associated to science and participants’ age, gender, or career choice?

After analyzing data accumulated across the four years, researchers also asked:

4. How are students interpreting the questions and words from the surveys?
 - a. Is the survey effectively measuring camp goals?

These questions were the forefront of the interviewing process. Under Notre Dame IRB approval, the 2017 Art 2 Science Camp also had researchers conducting interviews with participants who had both parental and participant consent. Researchers questioned participants' understanding of the survey, reasoning behind career choice, explanation for science and math ratings, and further explanation for their word associations and how the instructions/words were interpreted. The purpose of conducting interviews was to get more insight for trends seen in preliminary 2013-2016 data analysis.

2 Methods

Survey responses were coded to categorize responses in a numerical way to then translate data to plain text files and read into Root code. For example, careers were categorized as STEM (on account of degree required), sports, artistic, medical/health related, miscellaneous, and unsure.

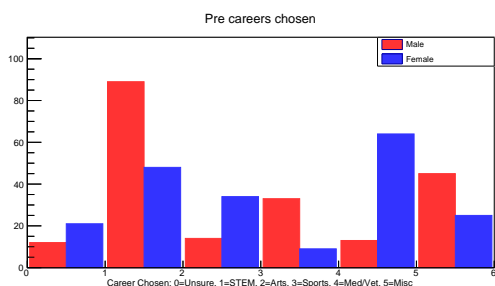


(Figure 1)

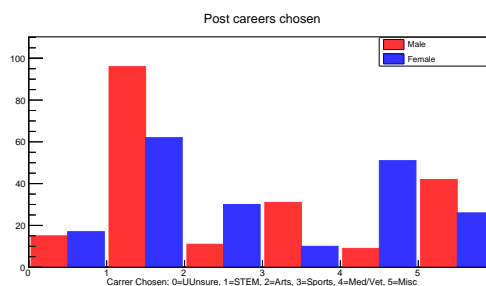


(Figure 2)

Bar charts with *standard mean error* were used to estimate the percentages of participants associating a specific word to science grouped by age (Figure 3). But standard with human studies, reporting error bars are only

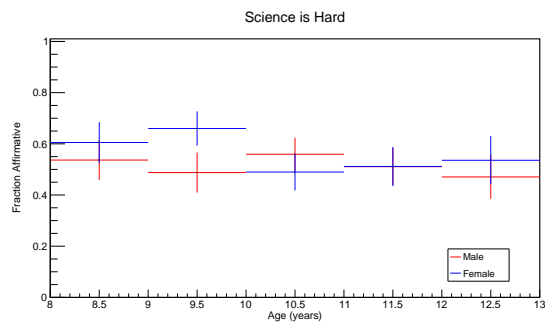


Figure 3

tentative and cannot take into account all possible factors. Associated word bar charts were utilized in analyzing data from across the four years to realize trends or queries to further inspect with statistical analysis. Only words repeated throughout the four years were analyzed for consistency which narrowed analysis to fifteen words.

Analysis compared data in search of statistical significant change i.e. if camp affected participants' survey responses or if specific groups of students had significantly different word associations. Statistical significance was calculated using a two tailed t-test comparing the pre to post survey responses. Calculating the significance between participant markers like gender, age, and career and the words associated in either pre or post surveys was done using a Chi-squared statistic. P values were calculated using the CHISQ.TEST in Excel comparing gender to words associated in both pre and post surveys, comparing gender to words but specifically in smaller age groups, and in comparing gender to words within only STEM majors. In comparing pre survey data with post survey data p values were calculated using the T.TEST function in Excel. Both tests were analyzed with the standard significance value of 0.05 in search of a $p < 0.05$.

Interviews were conducted with volunteered participants who submitted both parental and participant consent on the first day of camp. Interview questions were geared toward understanding the participants' perceptions of the survey questions. Analyzing graphs for word associations brought up questions about participants paradoxically associating antonyms. Volunteered participants were asked for clarification regarding the words they selected for science, especially words seeming to contradict each other and words researchers perceived potentially misunderstood or interpreted differently such as 'elderly', 'reading', 'same', and 'future'. Participants were also asked regarding the ratings they gave science and math after noting a discrepancy in the 2016 survey data between participants' ratings of science and liking math (Figures 4 and 5). As a last interview question, students were asked to

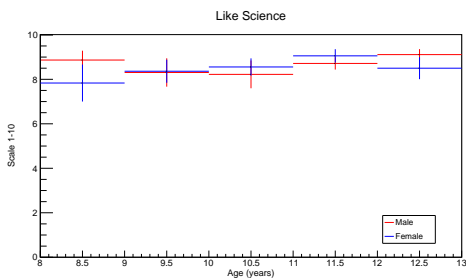


Figure 4

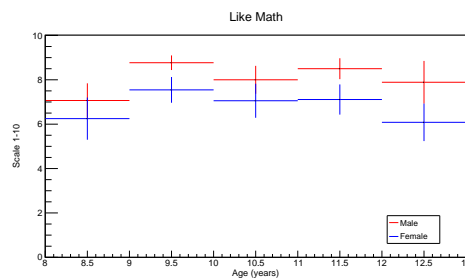


Figure 5

re-select words they thought a scientist would associate to science. This question was asked to gain a foundational understanding of how participants abstractly viewed science.

3 Results

Histograms showed gender gaps in word associations and also in pre-post career choices (Figures 1 and 2). Statistical analysis was used to determine if student characteristic such as age, gender, or career aspiration affected word associations. Also, interview results provided insight

about how camp participants were interpreting the surveys and also revealed survey takers' thought process on associating words.

3.1 Histogram results

Histograms revealed gender and age gaps in some word associations. As seen in Figure 6, some words demonstrated consistent gender gaps in percentages of students associating 'different' to science. Other words

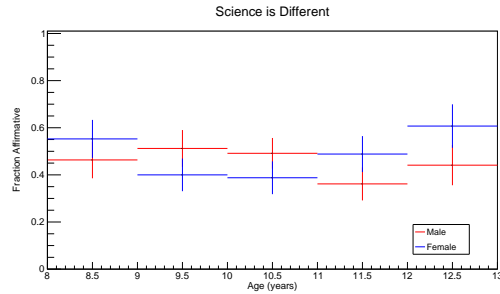


Figure 6

demonstrating similar gender gaps included 'making', 'reading', and 'boring' (Figures 7-9).

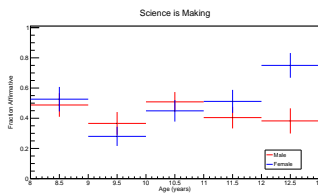


Figure 7

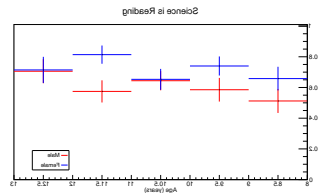


Figure 8

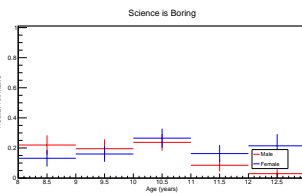


Figure 9

Gaps in gender were also seen seemingly related to participant age as seen in Figure 7 in the association of 'making'. These trends in word associations of gaps existing between genders and

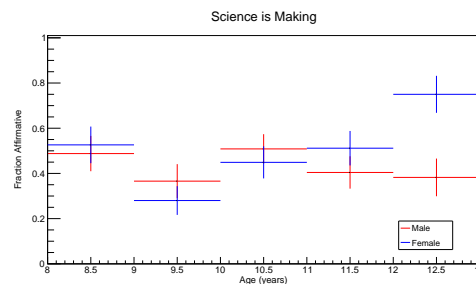


Figure 7

ages led to validity questions of whether researchers could say the gender of students affected associations or if ages affect associations. Tests were then run discovering changes of pre-post surveys and affects gender potentially had on word associations in either pre or post surveys.

3.2 Significant results

Statistical analysis suggests gender affected participants' association of the word 'different' to science and camp affected participants' associations of 'fun' and 'making'. Using the CHISQ.TEST function in Excel, researchers found $p < 0.05$ thus leading to rejecting the null hypothesis, H_0 , in gender to post-survey associations of 'different' suggesting post associations were affected by the gender of the participant. The T.TEST Excel function comparing post-surveys to pre-surveys found p values less than .04 for words 'fun' and 'making' therefore leading to a rejection of H_0 for pre associations of the words are not independent of the post associations suggesting camp does affect participant associations. In comparing pre to post associations and gender to pre/post associations researchers discovered significant p values for only these three words out of the fifteen repeated words. This evidence led to further questions about potential gender effects to associations within smaller age groups of participants. Questions about participants' understanding of words that might explain their differences in associations were addressed in the interviews conducted during the 2017 Art 2 Science camp.

3.3 Interview results

Interviews further explained participant understandings of individual words and survey questions. Younger students, aged 8-10, experienced difficulty understanding words used in 2016 and 2017 surveys 'youth' and 'elderly'. Some participants also made associations by considering inside and outside their classrooms; like when associating 'hard' and 'easy' students reflected science problems and ideas as hard but experiments and class projects as easy. Researchers also found most students consider varying aspects of science in associating 'new' and 'old' like understanding science has existed long before them and even today scientists are making discoveries. The youngest group of students, ages 8-9, did express misunderstandings of

the questions from the surveys. One example was associating words that rhyme with science because the words literally sounded like science. Other students expressed thinking all words on the survey had to be marked in some way even though there were words they did not understand and disagreed with. Interviews clarified reasons behind students seemingly associating paradoxical words but results also put the overall surveys into question since student interpretations of questions did not match with expected interpretations made by researchers

4 Conclusions

Histograms showed gender gaps in Figures 6-9 and also showed interesting changes between ages of participants and their word associations in describing science. Students appeared to have significantly changed views for the words ‘fun’ and ‘making’ when comparing pre-post surveys and gender was significant for the word ‘different’ associated in post-surveys. This leads to further questions on the relation between characteristics of participants such as age or career aspirations and their word associations and if any other connections show significant effects. Interview responses used to interpret student understandings bring validity of the current survey used into question so preliminary results lead researchers to expect changes to how questions of associations are phrased and possibly another change of listed words.

**CALCULATING ELECTRON DRIFT VELOCITY &
COMPLETING COMPONENTS OF ND CUBE**

Lauren Delgado
Advisor - Dr. Tan Ahn
2017 NSF/REU Program
Physics Department, University of Notre Dame

ABSTRACT

Calculations of drift velocity and ion straggling were obtained for a helium carbon dioxide mixture inside a time projection chamber (TPC). Because this gas detector could control parameters like electric field and pressure, these were altered to observe the relationships of those variables that could improve the quality of the experiment for studying cluster structure in nuclei. This collection of data would be significant for use in future analysis and comparison to experimental results. To use this detector, the construction of an electric field cage and feedthrough system were completed so that a test run could be made to gain preliminary results. These components will be tested for their efficiency by performing the experiment and examining whether the measurements produced results found computationally.

INTRODUCTION

Stars are formed from dust clouds containing hydrogen (H) and helium (He) collapsing into one another. Stars join the main sequence for about 90% of their lives, where they evolve depending on their mass. To focus on high mass stars, these stars ($> 8 M_{\odot}$) reach high enough temperatures to burn elements beyond helium like carbon, oxygen, and so on till iron. This type of reaction describes nucleosynthesis, which is the creation of new atomic nuclei. Atomic nuclei are a central focus within this project. The production of lighter nuclei and studying their interactions with light ions offers information. By analyzing the properties and behavior of nuclei, this allows us to "attain a deeper and more precise understanding of the many nuclear processes operating in astrophysical environment" (1). The goal is to understand what the structure of nuclei, by studying lighter nuclei, suggests about the formation of heavy metals beyond iron in some astrophysical scenarios.

GAS FILLED COUNTERS

Because the nucleus cannot be directly observed from its size ($1 \text{ \AA} \cdot 1.75 \cdot 10^{-15}$), information about the nucleus can be obtained through special equipment. This type of equipment has the capability of detecting radiation and also producing nuclei by accelerating charged particles. Within the scope of this experiment, the usage of gas proportional counters is crucial in order to measure particles of ionizing radiation. A gas proportional detector will bombard electrons with gas molecules frequent enough to create an avalanche of them to drift to the anode that will create a pulse. Usually in these detectors they are filled with noble gases since they are not electronegative. This device in this experiment will operate similarly.

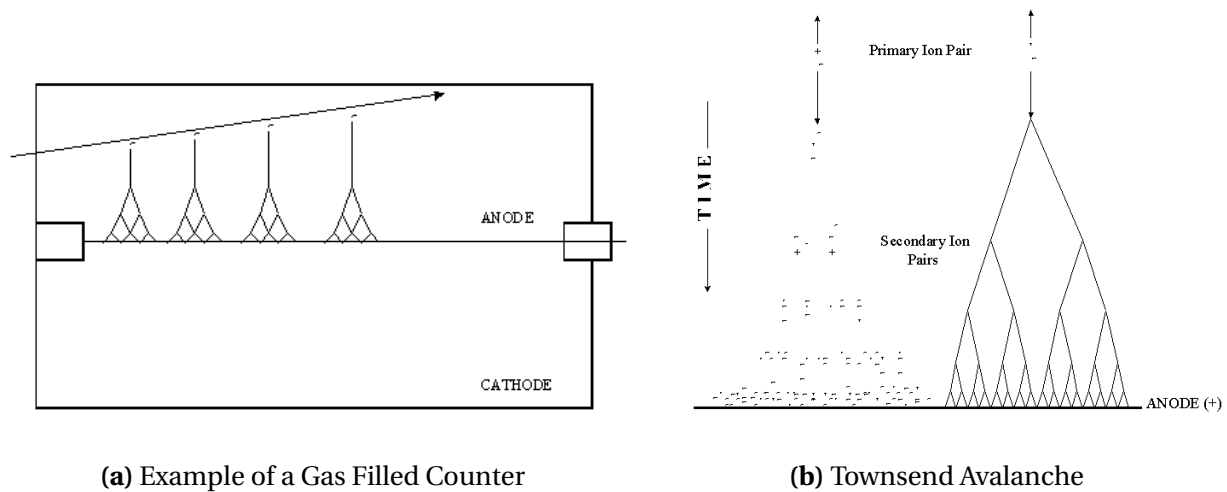


Figure 1: Looking at Gas Filled Counters (Credit to Oak Ridge Associated Universities Webpage on Proportional Counters)

ND CUBE FUNCTION

The ND Cube is a prototype TPC that is being used for this experiment. The cube stands out from normal gas detectors because it "uses a gas volume as [both] the target and tracking medium" (2). The dual use of the gas provides extreme precision for angle and energy measurements from charged-particle decays and higher areal densities that contain information about properties of those particles in the reaction. Thus, this device is advantageous for learning more about nuclear structure and looking at fusion.

METHOD OF USING ND CUBE

First, the ND Cube is filled with a gaseous mixture from a gas handling system it is connected to. Then heavy ion beams are sent into it where it interacts with the gas present inside. A large electric field is applied to the cage located inside. The heavy-ion beam ionizes the gas molecules as it collides with them. Free electrons begin to drift in the detector. Electrons drift to the bottom of the cube, towards a higher potential, at a constant velocity. At the bottom of the detector there is an amplification device (Micromegas) that collects these electrons and produces a signal from them and redirects this out to the front-end electronics. Within this specific experiment, drift velocity and straggling of ions are the focus because these parameters will affect the position of the identified radiation.

ELECTRON DRIFT VELOCITY

Calculations of drift velocity were made as a function of electric field and pressure for a helium carbon dioxide mixture. The results for velocities were obtained using a bash script that ran two programs named Magboltz (created by CERN) and Decode.

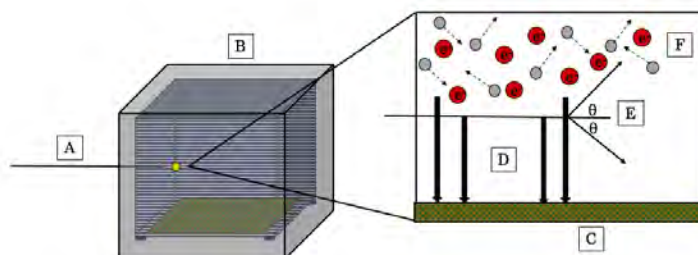


Figure 2: Components of Experimental Setup:

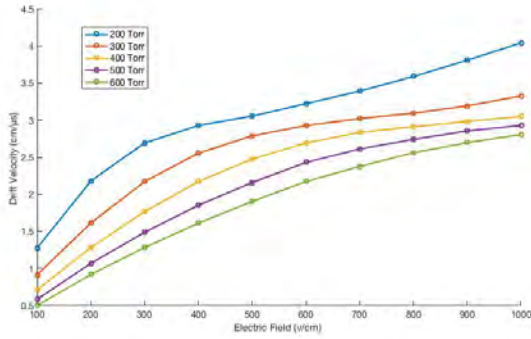
- (A). Incoming Beam
- (B). Electric Field Cage
- (C). Micromegas (Anode Pads)
- (D). Drifting Ions
- (E). Scattering of incoming radiation
- (F). Collisions between gas molecules and electrons

USING MAGBOLTZ & DECODE

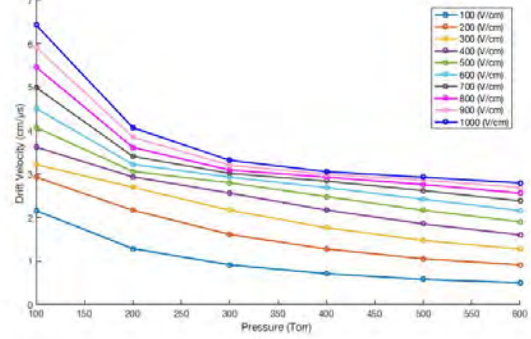
Magboltz uses input cards that denote certain values like number of gases, ratio of gases, pressure, temperature, and electric field. By entering in specific numbers into those cards, one can produce a list of outputs for ionization rates, collision frequencies, energy, and so on. Following that program, another one is called into the script called decode. Decode functions like a filter, to extract measurements crucial for data analysis.

DATA COLLECTION & ANALYSIS

For the purposes of this experiment, 5 sets of data were taken keeping pressure constant with varying electric field and incremented pressure for each set by 100 Torr. In addition, another 10 sets of data were taken keeping electric field constant with varying pressure. For each electric field set, the E field was incremented by $100 \frac{V}{cm}$. As seen by the Figure 3, increasing electric



(a) Varying Pressure in He:CO₂



(b) Varying Electric Field in He:CO₂

Figure 3: Effects of Pressure and Electric Field on Drift Velocity

field, also increases the drift velocity. However, another feature of the data shows that pressure increased slows the drift velocity. This inverse relationship illustrates that keeping pressure low would achieve higher drift velocities. Hypothetically, during performing the actual experiment, pressure would be fixed so the electric field strength needs to be varied to optimize the velocity.

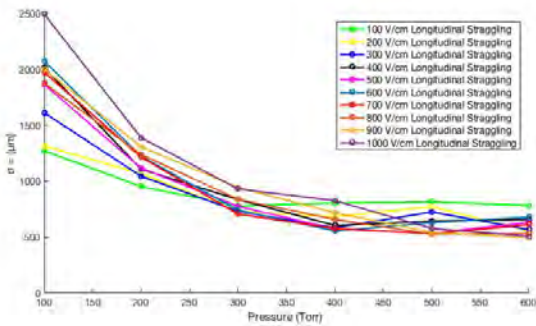
ION STRAGGLING

Information other than drift velocity, like the diffusion coefficient, was further analyzed. The diffusion coefficient, $diff_{co}$, offered information about the straggling of the ions, σ , when moving through the cube. Ions typically straggle when they enter another medium, meaning they deviate from their initial trajectory. Straggling is relevant because it should be minimized for this type of experiment. Both the longitudinal and transverse straggling were computed using diffusion coefficient, following this formula

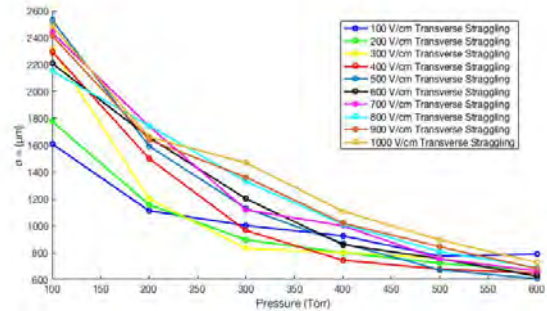
$$\sigma(\mu m) = diff_{co} \cdot \sqrt{length} \tag{1}$$

DATA COLLECTION & ANALYSIS

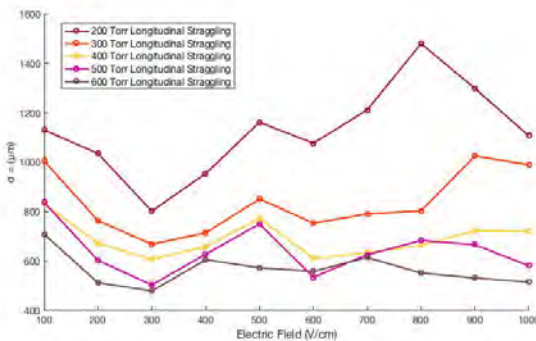
Similar to the data acquired for drift velocity, 5 sets of data were taken keeping pressure constant with varying electric field and incremented pressure for each set by 100 Torr. Then another 10 sets of data were taken keeping electric field constant with varying pressure. For each electric field set, the E field was incremented by $100 \frac{V}{cm}$. However, this produced twice the amount data because there were two types of straggling to examine: longitudinal (along the beam direction) and transverse (perpendicular to the beam direction). Figure 4 shows how changing pressure affects



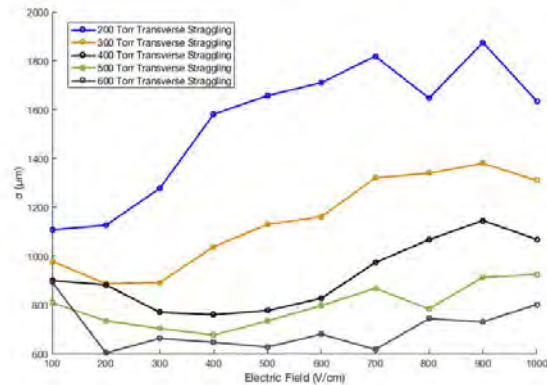
(a) Changing Pressure on Longitudinal Straggling



(b) Changing Pressure on Transverse Straggling



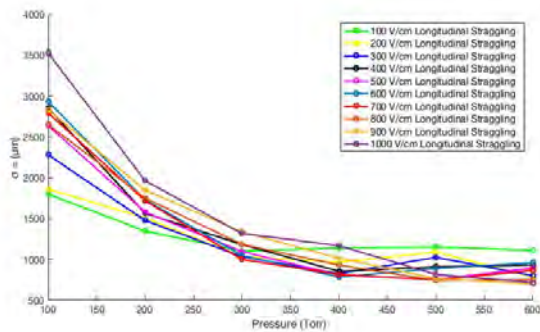
(c) Changing E-Field on Longitudinal Straggling



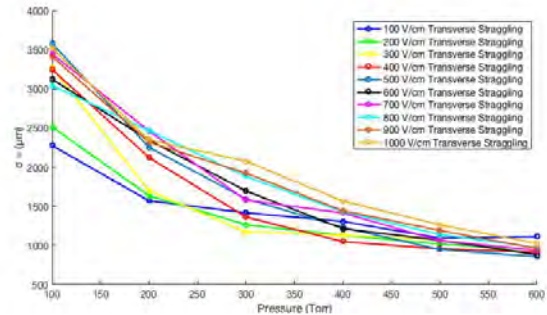
(d) Changing E-Field on Transverse Straggling

Figure 4: Effects of pressure and electric field on ion straggling in both the longitudinal and transverse directions. Length for ion travel is 10 cm in this run of data.

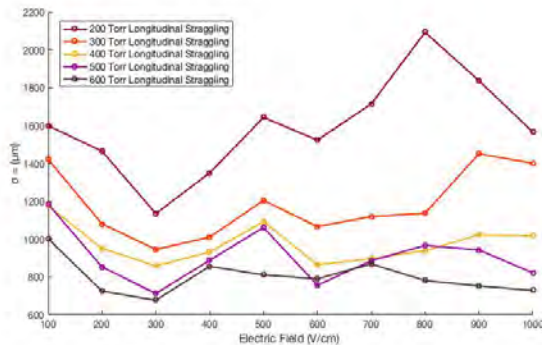
longitudinal and transverse straggling of ions when electric field is kept constant. Evidently, increasing pressure, lowers the amount of straggling of ions in either direction. Therefore, it would be optimal to secure the detector at a high enough pressure to reduce straggling. Electric field strength had no uniform effect on transverse and longitudinal straggling. Overall, frequently there were higher values for transverse straggling as opposed to longitudinal straggling in all sets of data. For each trial, 10 and 20 cm sample lengths were used to observe whether the



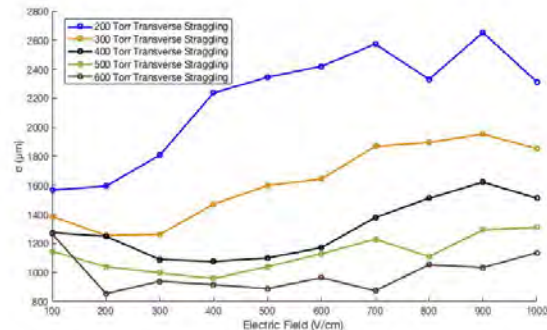
(a) Changing Pressure on Longitudinal Straggling



(b) Changing Pressure on Transverse Straggling



(c) Changing E-Field on Transverse Straggling



(d) Changing E-Field on Longitudinal Straggling

Figure 5: Effects of increased length for ion to travel on straggling in both the longitudinal and transverse directions. Length for ion travel is 20 cm in this run of data.

distance traveled by the ions affected the amount of ion straggling that would take place. The prediction was that the more distance the ions would have to travel, the more straggling would

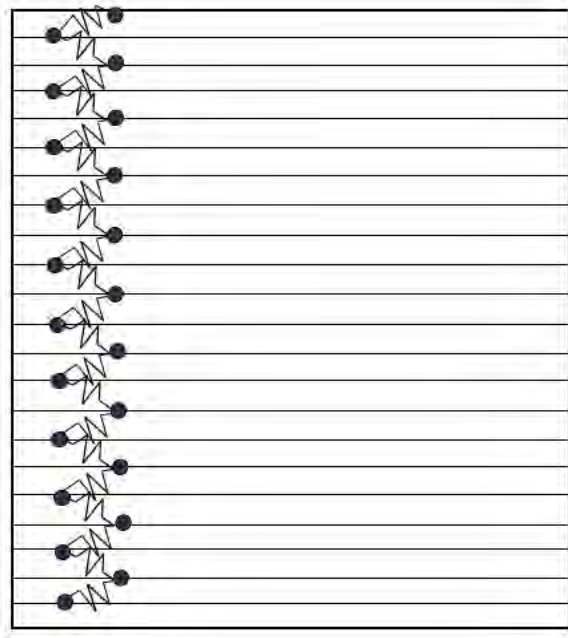
take place. This hypothesis was reflected accurately in the results collected. The highest value for longitudinal straggling in Figure 4 (a) for a 10 cm path reached 2500 μm , whereas the highest value for the 20 cm path was 3500 μm in Figure 5 (a). This trend was established throughout the other data too.

RESISTOR CHAIN

Inside the ND Cube, previous students had built an electric field cage with 21 metal conducting rings to produce a uniform electric field. Recently the resistor chain was completed as part of this project. This chain is crucial to the experiments because it provides the uniform electric field needed. This field is created by the even spacing of rings on the cage. Every ring will divide the voltage applied by the number of rings present. Therefore, the combination of the number of rings and even spacing between them maintains uniform field strength. The resistor chain was finished through soldering.

SOLDERING PROCESS

Soldering is a technique used to create permanent connections between electronic components. Each resistor within the chain had 20 megaohm resistance. First, two resistors were connected by placing them inside the same lug terminal and then those connections were crimped into place to stay secure. To successfully solder each connection properly without damaging the resistor itself, two clamps acting as heat sinks had to be placed where the ring and lug terminal met and where the wire of the resistor extended. Then, the electric field cage was turned on its side. With a soldering iron gun, the lug terminal was heated with metal wire, which solidified the connection. This was repeated multiple times until the chain was complete. After this was done,



(a) Resistor Chain Outlined Design



(b) Upclose Image of Resistor Chain

Figure 6: Resistor Chain Connections

a digital multimeter was used on every two resistor connections to check their resistance and make sure they were successfully connected by the soldering process.

FEEDTHROUGH SYSTEM

For the final leg of the project, the ND Cube required feedthroughs to make sure the electronics could receive the information from the experiment. For that reason, the final feedthrough design included a high voltage feedthrough entering from the top of the detector that connected to the cathode plate at the top of the electric field cage. Along with that, on the right side of the cube, five holes were made on an end cape for 3 BNC (coaxial) connectors and 2 SHV (high voltage) connectors. The design's practicality is that the single ended SHV connector from the top of

the cube can conveniently drop a wire down onto the cathode plate. The wire would not bend and could attach easily. The bottom 2 SHV connections are significant because they are located closely to the Micromegas, but can also reach the second to last ring where the field cage is grounded. Because of that placement, signals from the cube can reach out from the electronics into a computer located beside it.

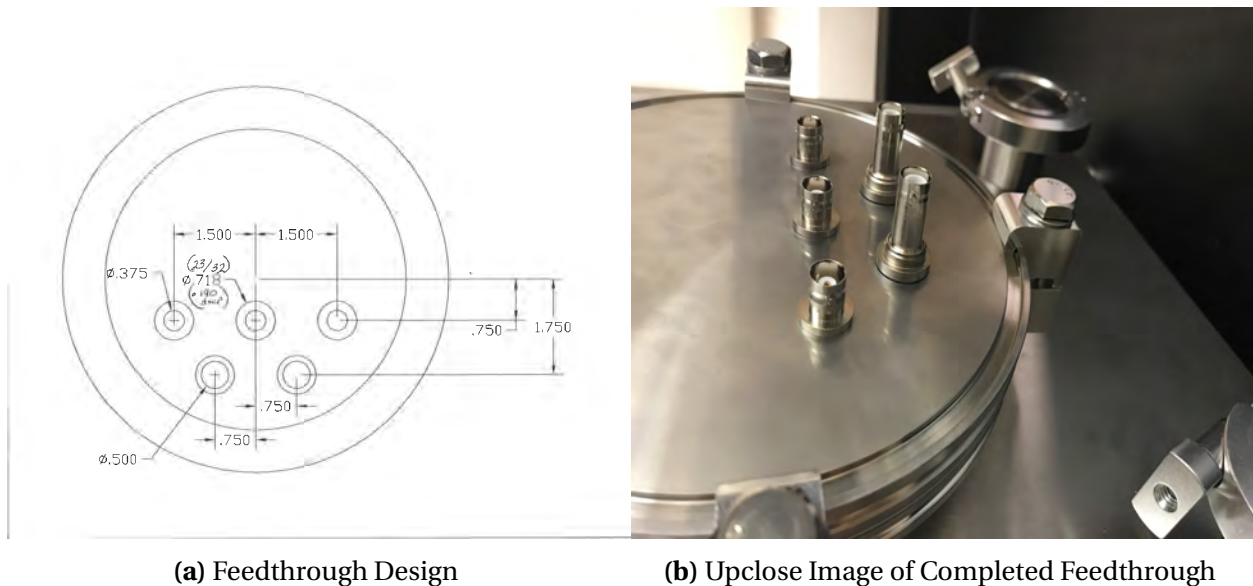


Figure 7: Feedthrough System

REFERENCES

1. Claus E. Rolfs and William Rodney, *Cauldrons in the Cosmos: Nuclear Astrophysics by Claus*, (XVI)
2. University of Notre Dame: ISNAP Experimental Setups Page, "Prototype Active-Target Time-Projection-Chamber"

PIXE and RF Analysis of Roman Denarii

Cecilia Fasano, M. Raddell, K. Manukyan, E. Stech, M. Wiescher

Notre Dame Department of Physics / July 2017

Abstract:

A set of Roman Denarii from the republican to the imperial period (140BC-240AD) has been studied using X-ray fluorescent (XRF) scanning and proton induced x-ray emission (PIXE) techniques. XRF and PIXE are commonly used in the study of cultural heritage objects because they are nondestructive. The combination of these two methods is also unique because of the ability to penetrate the sample with a broader spectrum of depths and energies than either could achieve on its own. The coins are from a large span of Roman history and their analysis serves to follow the economic and political change of the era using the relative silver and copper contents in each sample. In addition to analyzing the samples, the study sought to compare these two common analysis techniques and to explore the use of a standard to examine any shortcomings in either of the methods. Data sets were compared and then adjusted to a calibration curve which was created from the analysis of a number of standard solutions. The concentrations of the standard solutions were confirmed using inductively coupled plasma spectroscopy. Through this we were able to assemble results which will progress the basis of understanding of PIXE and XRF techniques as well as increase the wealth of knowledge of Ancient Roman currency.

Introduction:

Through the use of micro-XRF and PIXE, data of the relative elemental compositions of a number of Roman Denarii from 140BC-240AD were collected and analyzed. The data were then analyzed to give specific quantifications, by weight, of the bulk elements and trace elements of the coins. From these data we were able to create a visual representation of the changing silver and copper contents throughout the entire timeline of the samples.

The Silver Denarius was introduced in 201 BC after the Punic wars as the new silver standard coinage of the Roman republic. The Denarius was minted from virtually pure metal (99-99.5% fine). With an initial standard of 72 Denarii (4.5g) minted from one pound of silver (322.5g) it proved to be stable enough to help finance the expansion of the empire (200-91BC) and the challenges of the civil wars of the first century (90-31BC). During the civil wars devaluation occurred by gradually reducing the weight so that 84 Denarii of 3.8g each were minted from one pound of silver. This value was established as a new standard of the Augustan currency reform. The Denarius continued to be used as standard coinage during the first 200 years of the imperial period but was devalued several times by reduction of the silver content.

Experimental Arrangements:

For the PIXE analysis of the coins, the experiments were performed at the 10 MV FN Pelletron Tandem accelerator at the Nuclear Science Laboratory (NSL) of the University of Notre Dame. Proton beams with less than 5 nA intensities were used after penetrating through a 6 μm thick

aluminized mylar window to probe the coins, which were positioned at a distance of 2.6 cm from the exit window. The x-rays were analyzed using a Ortec SLP Series Lithium-Drifted Silicon detector with a 0.5 mm Be window and an active diameter of 10 mm positioned at a 40 degree backward angle with respect to the beam direction.

For the XRF analysis of the coins, the experiments were performed in part on the Bruker Handheld XRF at the NSL at the University of Notre Dame and in part on the ORBIS XRF machine at the Center for Environmental Science & Technology (CEST) lab at the University of Notre Dame. The Bruker Handheld device contains a rubidium source and was used exclusively for single point analysis. Each coin was scanned three times for a duration of 180 seconds. The number of runs and the time duration were instrumental in ensuring a consistent result. The beam was approximately 1mm in size and the detector was positioned at a 45-degree angle. An aluminum filter was used to block out as much background as possible which allowed for a more accurate quantification.

The ORBIS XRF was used primarily for large scale mapping and a few single point analyses. It was run at a voltage of 40 kV and a current of 400 uA and was run each time with a 25 um Aluminum filter as to stay consistent with the handheld device. To do large scale mapping, the machine triggers the x-ray beam many hundreds of times over the entire specified area. A 30 micrometer beam was used and the spacing between each data point was between 70 and 95 um. This allowed for a large number of points to be taken and for a more accurate image to be created. The images, as part of figures 1 and 2 below, are color coded for each element. For single point analyses, a 1mm beam spot was used.

Table 1 lists the Denarii which were used in this study by their period of minting. The obverse and reverse sides of coins are shown in figures 1 and 2.

Lucretius Trio	136 BC		Marcus Aurelius	149 AD
Publius Clodius	42 BC		Commodus	189 AD
Markus Antonius	31 BC		Septimus Severus	197 AD
Tiberius			Septimus Severus	199 AD
Nero	65 AD		Geta (as Caesar)	200 AD
Vespasian	74 AD		Caracalla	213 AD
Trajan	107 AD		Elagabalus	220 AD
Trajan	115 AD		Severus Alexander	224 AD
Antoninus Pius	140-144 AD		Maximinus I	235 AD
Marcus Aurelius	145-146 AD		Gordian III	

The coins included three Denarii from the republican period. One was minted by the Gnaeus Lucretius Trio in 136 BC during the consulate of Sextus Atilius Serranus and Lucius Furius Philus. The second one was minted in 42 BC by Publius Clodius at the beginning of the second triumvirate

of Octavianus, Marcus Aemilius Lepidus and Marcus Antonius. The third Denarius was minted in 31 BC after the end of the second triumvirate, a so-called legionary Denarius by Marcus Antonius to pay for his legions in his struggle with Octavian for supremacy.

The coins minted during the first century of the Roman Empire and analyzed in this study include a Denarius minted in 65 AD towards the end of the reign of Nero (54 AD-68 AD), after he had reorganized the Roman mint to finance the rebuilding of Rome after the great fire in 64 AD; a Denarius struck in 74 AD during the last year of the reign of Vespasian (69AD-74AD); two Denarii struck in 107AD and 115 AD during the reign of Trajan (98AD-117AD) honoring his conquests of Dacia and Arabia.

Several of the Denarii included in the study came from the period of the reign of Antoninus Pius (138-161 AD), which characterized a very prosperous and peaceful time of the Roman Empire. One Denarius was minted during the early period 140-144 AD of his reign. Two coins from the same period were minted in 145AD and 149 AD by Markus Aurelius, who served as Caesar with Antoninus Pius before becoming himself emperor (161AD-180AD). The last Denarius from this period of the adoptive emperors was minted in 189 AD under Commodus (180-192 AD), who was the natural son of Marcus Aurelius.

Of particular interest are the coins minted during the period of the Severan emperors, which mostly ruled through military force. The investments in military salaries and the costs for the numerous military campaigns led to gradual debasement of the Denarius. This was investigated by the analysis of two coins minted 197 AD and 199 AD showing the image of Septimus Severus (193-211). During the period of the Severi emperors the silver currency underwent significant fluctuations as outlined before. This should be reflected in the silver content of the coins minted in 197 AD during the short co-reign of Geta (197-211), and in 213 AD during the reign of his brother Caracalla (198-217 AD). A sample of each was studied for this analysis. Also analyzed were Denarii minted during the final years of the Severan period, this included the analysis of Denarii minted under Elagabalus (218-222 AD), Severus Alexander (222-235 AD), and Maximius I (235-238 AD) that are expected to show considerable fluctuations as a consequence of debasement and stabilization policies followed by these emperors. During the reign of Maximius the Denarius was so devalued that his eventual successor Gordian III decided to replace the coin by the Antonianus, which was based on a lower silver content of 70% with respect to the Denarius. For comparison PIXE analysis was also performed at an Antonianus struck in 239-240 AD during the reign of Gordian III (238-244 AD).

PIXE measurements were performed with beam energies of 3.0 MeV for several spots at the obverse and reverse side of each coin for investigating the surface composition of the coins. Some spots were repeatedly measured to check the consistency of the experimental conditions. The results indicate that in most cases the silver-copper composition was consistent for both sides and agreed within less than 2% standard deviation. Only in cases of pronounced surface structure differences in X-ray intensity from the obverse and reverse sides were observed which

mounted up to 10% standard deviation. These discrepancies were related to differences in X-ray transmission and edge scatterings as confirmed by test measurements using different spot positions.

A depth profile of the silver-copper composition for a selected number of coins was mapped using PIXE by increasing the energy of the proton beam from 3 MeV to 9 MeV in 0.5 MeV steps. This corresponds to a penetration depth ranging from 35 to 350 μm . The silver copper bulk composition of each coin was measured using energies of 7 MeV which corresponds to a penetration depth of 140 μm . These measurements provide information about possible radial variations in the characteristic X-ray intensity. In addition, several random measurements were performed to check the consistency of the X-ray yield.

Data Analysis:

As stated earlier, the results of measurements at lower energies are restricted by surface corrosion and contamination effects. In addition, silver-copper alloys are restricted by surface enrichment of silver. PIXE measurements were performed for different energies to map the surface and bulk silver copper composition of the coins. Figure 1 shows the depth profile for the minted by Lucretius trio at 136 BC from the republican period and a coin from the imperial period of Elagabalus minted at 220 AD in the early third century. While the first coin shows no variation in the silver copper composition with depth, the second coin shows a slight 5% increase in silver with depth, which is correlated with a similar decrease in copper. This variation occurs in the 60 μm surface layer, the deeper layers show no variation in composition.

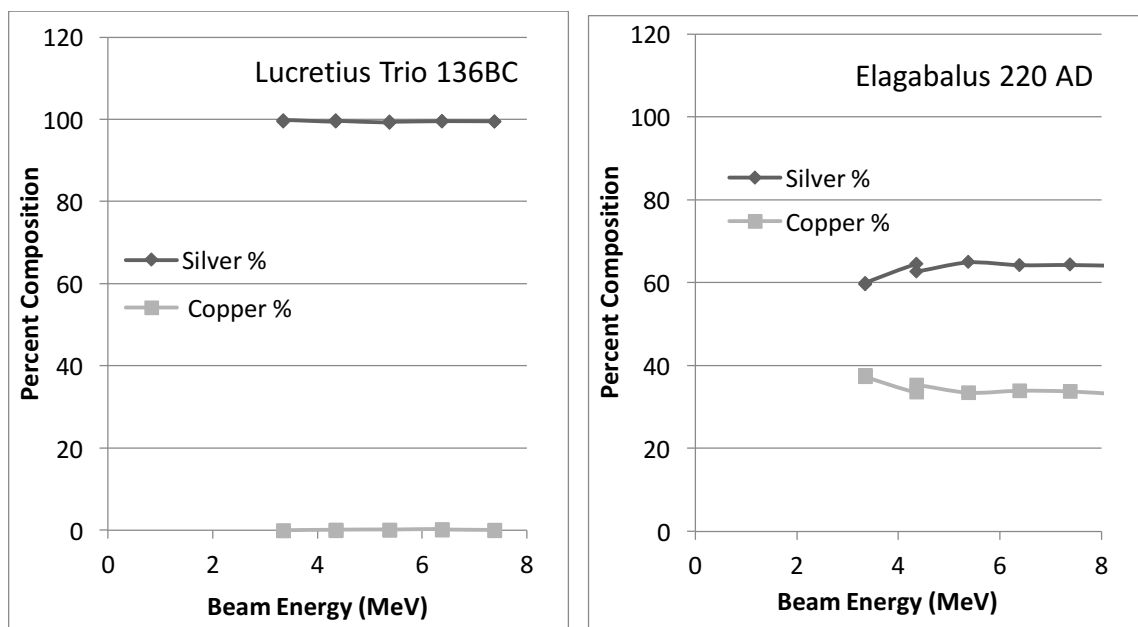


Figure 1: Depth profile of the silver copper composition of two Roman Denarii from the republican period and the imperial period of the early third century of the Roman Empire.

The results indicate that the bulk composition can be measured with proton beam energies for 6 MeV and more. To minimize absorption effects of the low energy X-rays; a beam energy of 7 MeV was chosen for studying the bulk composition of the coins at an average depth level of 140 μm .

To monitor the surface homogeneity of the coin composition a number of PIXE measurements were performed across the surface of each coin. The reverse side showed a more homogeneous pattern with variations between 5% standard deviation. The variation of the characteristic X-ray intensity was more pronounced when scanning the obverse site because of its more pronounced surface structure. The most pronounced variations of sometimes more than 20% deviation from the mean value were observed in the coins from the third century. These probably reflect inhomogeneities in the silver-copper alloy composition as a consequence of re-using coins from earlier rulers as it was frequently the case in the period of unrest in the early third century.

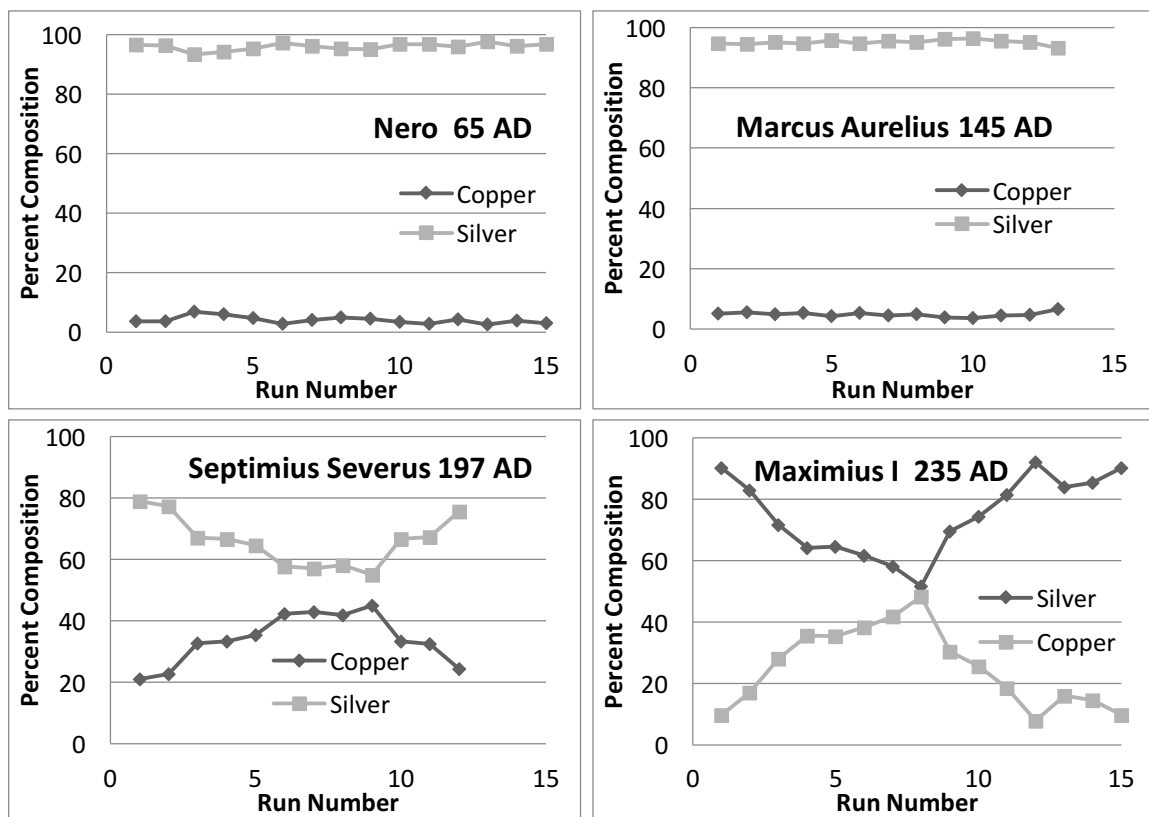


Figure 2: Cross sectional PIXE measurements of the Copper-Silver composition of four Roman Denarii from the first, second, and third century of the Roman Empire. The first two coins represent a homogeneous distribution in the composition within a 2% standard deviation, which reflects the economic and fiscal stability of the Empire after the monetary reform of Nero in 65 AD. The two coins from the early third century show dramatic variations with the silver content being significantly reduced in the central region of the coin. A similar pattern was observed for the coins minted during the reign of Caracalla and Elagabalus. This reflects the overall decline in the quality of the minting process due to

limitation to access to silver mines by external war and due to in-mixing of coins from earlier periods.

For single point analysis of the coins using XRF, we were not able to counter the effects of surface corrosion and silver surface enrichment by changing the energy of the beam as was done with the PIXE analysis. The way these issues were combatted with the XRF was by running the beam many different times on multiple locations on the coin. Even with these methods, though, we believe that the deviation between the results of our methods can be mostly attributed to silver surface enrichment and corrosion. As we found through large scale mapping, many of the coins have incredibly inconsistent surface compositions and an inability to penetrate beyond those surface blemishes leads to an inconsistency in the results of different methods and even the results on the same coin using the same method. The x-ray beam used in both the Bruker handheld device and the ORBIS large device was 1mm which only penetrated the coin to a depth of around 200 micrometers. At its deepest, silver surface enrichment can go as far as 500 micrometers into the surface of the coin. Based on these data, the average silver-copper composition has been determined for each of the studied coins and is recorded in Table 2. The references for the republican coinage (Cr) and imperial coinage (RIC) shown in the table relate to the traditional notation for identification of a particular coin as defined in the numismatic literature ^{i, ii}.

Coin	Notation	year	Avg %Cu PIXE	Avg %Ag PIXE	Avg % Cu ORBIS	Avg %Ag ORBIS
Lucretius	CR 237	136 BC	0.18	99.63	1.91	97.35
Publius Claudius	CR 494	42 BC	1.95	97.34	1.83	96.79
Marcus Antonius	CR 544	31 BC	5.73	92.69	4.01	94.11
Tiberius			~	~	0.22	98.64
Nero	RIC 67	65 AD	3.97	95.90	12.72	86.44
Vespasian	RIC 75	70 AD	9.61	89.38	2.52	96.77
Trajan	RIC 128	107 AD	4.02	94.73	3.99	94.12
Trajan	RIC 142	115 AD	7.80	91.23	12.1	87.06
Antonius Pius	RIC 63	140 AD	7.03	92.42	2.44	96.69
Marcus Aurelius	RIC 429	145 AD	4.01	95.94	2.51	96.77
Marcus Aurelius	RIC 448	149 AD	4.86	95.12	2.03	96.90
Commodus	RIC 192	180 AD	13.59	86.42	2.69	96.56
Septimus Severus	RIC 107	193 AD	33.98	66.02	7.24	91.96
Septimus Severus	RIC 136	197 AD	36.85	63.16	13.46	85.70
Geta	RIC 18	198 Ad	45.80	53.33	5.97	93.24
Caracalla	RIC 224	213 AD	14.59	85.40	3.94	95.28
Elagabalus	RIC 295	220 AD	34.97	63.64	3.93	95.31
Severus Alexander	RIC 44	224 AD	4.70	95.26	2.36	96.85
Maximus I	RIC 7	236 AD	25.15	74.85	18.85	79.84
Gordian III	RIC 70	240 AD	24.25	74.91	6.10	93.11

For the Bruker XRF device, the data was quantified by looking at the relative numbers of counts for each element and plotted for both silver and copper in chronological order as can be seen below.

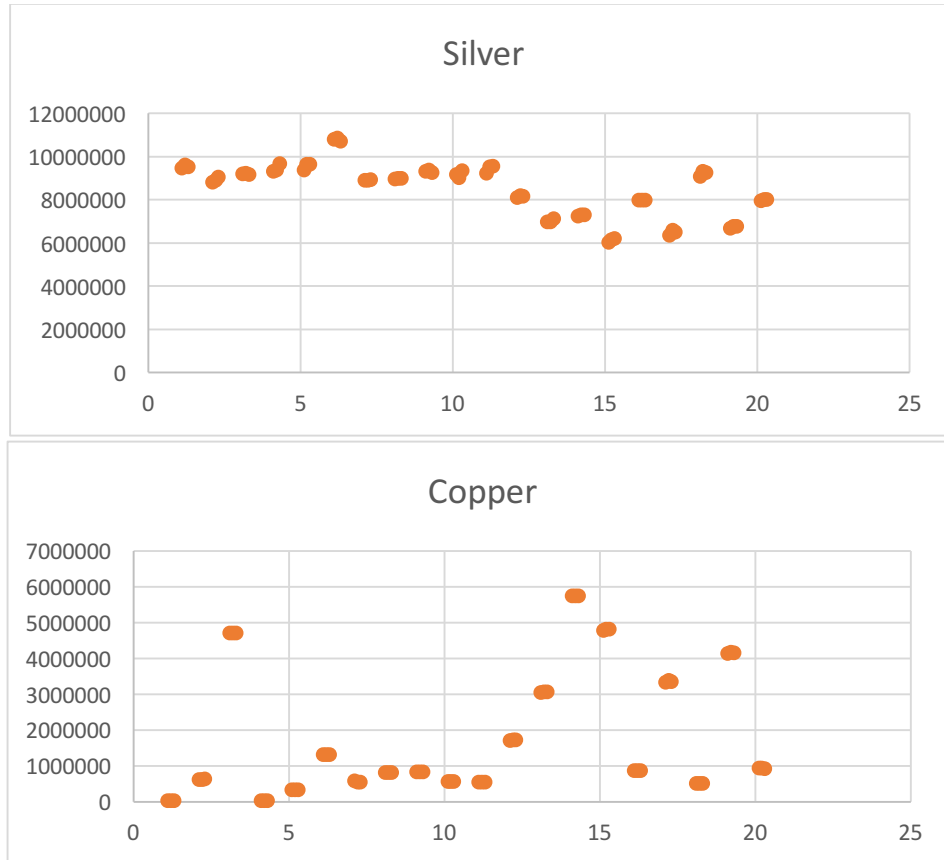


Figure 3, the relative counts of silver and copper in each coin as recorded by the handheld device. The bottom axis is the coin number and it is plotted against the number of counts recorded.

Those relative counts, for silver, were plotted with the weight percent compositions of silver from both the ORBIS and PIXE data sets to create a graph of the silver content of the coins across the total timeline. The left axis is number of counts as measured by the Bruker XRF. The right axis is the percent silver by weight. Each coin was assigned a number in chronological order and are shown on the x axis progressing as a function of time.

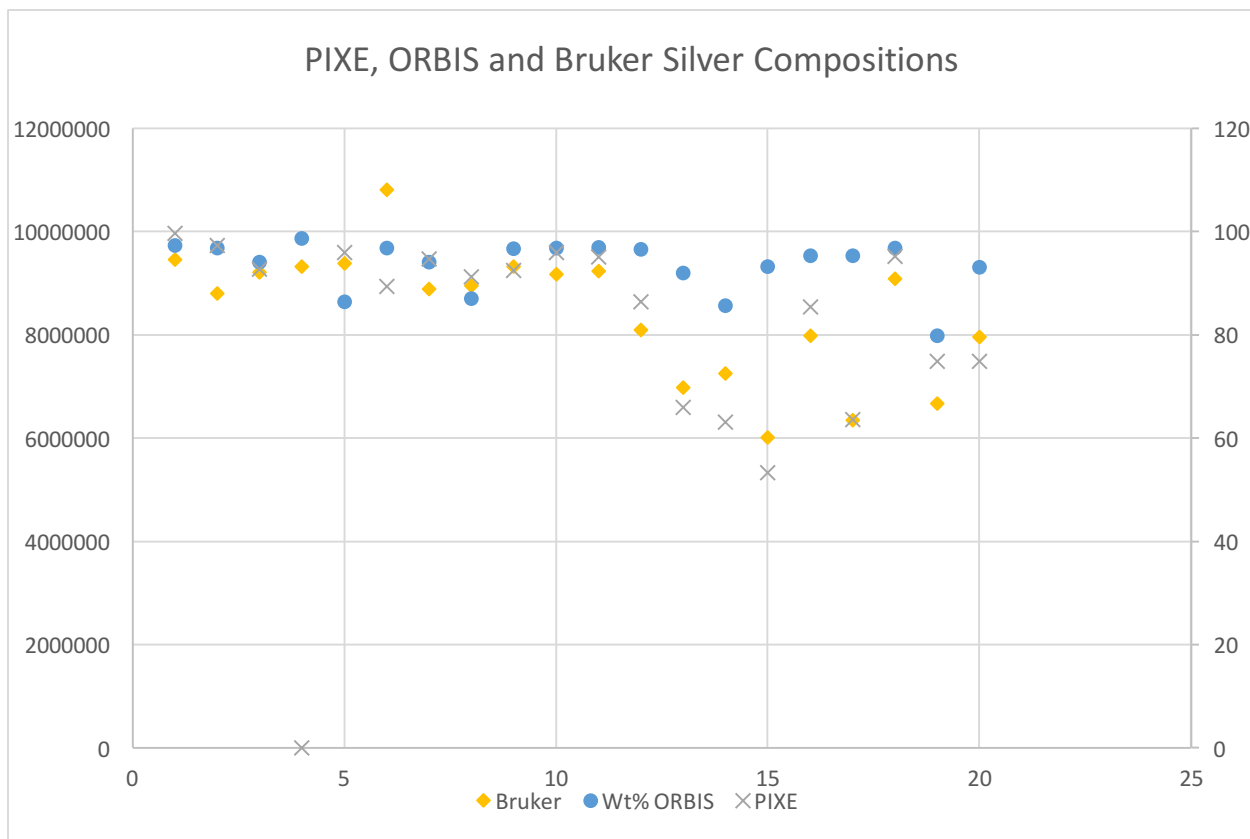


Figure 4, the Silver composition of each coin for each method where the bottom axis is the coin number, the left axis is number of counts, and the right axis is percent weight.

As can be seen in the graph, though there are a few inconsistencies, the general trend and shape of the data points is the same across all of the analysis methods. These trends lead us to believe that, within error bars, our data give an accurate representation of the change in elemental composition across the entire timeline of our sample set.

Conclusions: The figure clearly demonstrates the stability of the Roman silver coinage during the period of the Republic after the introduction of the Denarius despite the economic difficulties during the civil wars that led to the fall of the republic and the installation of the imperial system. The figure clearly demonstrates the two decisions for the reformation of the mint by Octavianus Augustus in 25 BC and the debasement by Nero in 65 AD. The silver-copper composition of the Denarius remained rather constant during the subsequent century, smaller fluctuations have been observed which relate to the debasements by Trajan and Marcus Aurelius.

The rapid decline in the silver content of the Denarius at the end of the second and first 40 years of the third century is clearly visible in the data recorded in Table 2 and shown in Figure 3. These drastic devaluation policies were primarily established under Septimus Severus and Geta driven by the costs for maintaining the army and for wars of expansion against the Germanic

tribes and the Parthian empire. The attempts of Severus Alexander for stabilizing the monetary stability is reflected in the increased silver content of the Denarius minted at that time. Also reflected in figure 6 is the drastic decline of the Denarius driven by the military expenditures of emperor Maximius I.

From this study, the following conclusions can be drawn. This data allows us to provide evidence for the historical literature and standards of the ancient Roman republic and empire. The silver content over the timeline of the coins matches quite well with the historical context of the era. The use of both PIXE and XRF also allows us to have confidence in the accuracy and precision of our results within our knowledge of the error in the equipment and the inconsistencies in the surface of ancient coins. Future work done in this area will help to more precisely tune and understand both the instruments used in cultural heritage investigation and the numismatics of Roman history.

(These are the sources from the original PIXE paper)

ⁱ K. W. Harl, *Coinage in the Roman Economy, 300 BC to AD 700*, John Hopkins University Press, Baltimore & London 1996

ⁱ A. Dacca, P. Prati, A. Zucchiatti, F. Luccarelli, P.A. Mando, P. Gemme, R. Parodi, R. Pera, *Nucl. Instr. Meth. B161* (2000) 743

ⁱ R. Klockenkämper, H. Bubert, K. Hasler, *Archaeometry* 41 (1999) 311.

ⁱ V. Kantarelou, F.J. Ager, D. Eugenidou, F. Chaves, A. Andreou, E. Kontou, N. Katsikosta, M.A. Respaldiza, P. Serafin, D. Sokaras, C. Zarkadas, K. Polikreti, A.G. Karydas, *Spectrochim. Act. B* 66 (2011) 681

ⁱ L. Beck, S. Bosonnet, S. Réveillon, D. Eliot, E. Pilon, *Nucl. Instr. Meth. B* 226 (2004) 153

ⁱ D. R. Walker, *The Metrology of the Roma Silver Coinage: Parts I-III*; *Brit. Archaeol. Rep. Suppl.* 5, 22, 40 (1976-1978)

ⁱ A. Denker, K. H. Maier, *Nucl. Instr. Meth. B* 161-163 (2000) 704-708

ⁱ GUPIX reference

ⁱ M. H. Crawford, *Roman Republican Coinage*, 2 Volumes, Cambridge University Press, Cambridge, UK 1974

ⁱ *Roman Imperial Coinage*, Vol. 1-9, eds. C.H.V. Sutherland, R.A.G. Carson, Spink & Son Ltd, London, UK

Experimental Determination of the Angular Acceptance of the Strong
Gradient Electromagnetic Online Recoil Separator for Capture Gamma
Ray Experiment (St. George) and Observation of Quadrupole Field
Reproducibility

Will Feltman

2017 NSF/REU Program

Physics Department, University of Notre Dame

Advisor: Dr. Manoel Couder

Graduate Students: Luis Morales, Chris Seymour, Gwen Gilardy, and Shane Moylan

Abstract:

The STrong Gradient Electromagnetic Online Recoil separator for capture Gamma ray Experiment (St. George) is in the process of determining its experimental limits. Currently the focus is on determining the angular acceptance of particles entering the St. George beam line. The demonstration of the current experimental angular acceptance is discussed in addition to the necessary procedure to ensure that St. George's quadrupoles generate consistent magnetic fields.

1. Introduction:

For the past centuries scientists have spent a considerable amount of time observing and studying various types of stars. Thanks to advances in modern science, they have managed to obtain a good understanding of how stars operate, such as what fuels their fiery existence, how they produce many chemical elements, and how they die. However, they don't currently have a complete understanding of all the various nuclear reactions that occur, which has led to the creation of new techniques to study stars and various stellar reactions.

Since it is currently impossible to create the conditions of a star in a laboratory, physicists had to think outside of the box to create a procedure to study the rare reactions that occur in and around stars. Frequently, nuclear reactions are studied by detecting the gamma rays released when the reaction occurs. However, with low energy nuclear reactions the gamma production levels can be so low that it is impossible to separate them from the overall background gamma radiation, making it necessary for other methods to be created. Inverse kinematics is one such method in which a heavy ion beam strikes a lighter target. For the reactions which St. George was designed to study, the sum of nucleons (A) in the beam is greater than four, and the target is often hydrogen or helium. The STrong Gradient Electromagnetic Online Recoil Separator for capture Gamma ray Experiment (St. George), located in the Nuclear Science Laboratory at the

University of Notre Dame, Notre Dame Indiana was designed and constructed to study nuclear reactions through the implantation of inverse kinematics.

The construction of St. George, was completed in 2010, and since then has been preparing to study rare (α,γ) reactions. St. George is composed of eleven quadrupole magnets (Qn), six dipole magnets (Bn), and a Wien Filter (WF), each of which serve a different purpose, in addition a series of detectors and viewing quarts have been installed to gather more information about the ion beam traveling through St. George. The dipole magnets are used to steer the reacted components through the St. George's beam line to detectors located at the end. The quadrupole magnets produce consistent magnetic fields, designed to focus in one spatial direction while defocusing in another. Magnets Q1, Q4, Q7, Q8, and Q11 focus in the Y direction while defocusing in the X and magnets Q2, Q3, Q5, Q6, Q9, and Q10 do the opposite. The Wien Filter, often called a Velocity filter, sorts particles based on their velocities, by employing both a magnetic and electric field only particles with velocities equal to the electric field divided by the magnetic field, are allowed to pass through uninhibited. The other particles that manage to enter the Wien Filter are pushed to the sides and discarded, this allows for only the particles of interest to be transmitted. A series of three quadrupoles called the triplet is located shortly before the HIPPO Gas target. This is used to help prepare the beam to enter St. George.

The beam provided for St. George comes from the 5 MV Stable Ion Accelerator for Nuclear Physics (5U) which was installed in 2012 and first ran in 2015. Since St. George has been able to receive beam, its experimental limits have been studied. Previously, the experimental limits of the energy acceptance of St. George was been determined. This was demonstrated by individual experiments in which eight different beams were delivered to St. George. An un-deflected transmission of each beam was observed, where it was found that 100%

of ions within +8% of the energy for which St. George was tuned to accept were able to reach the end [2]. Since then, efforts have shifted to focus on determining the angular acceptance, which has a theoretical value of ± 40 mrad.

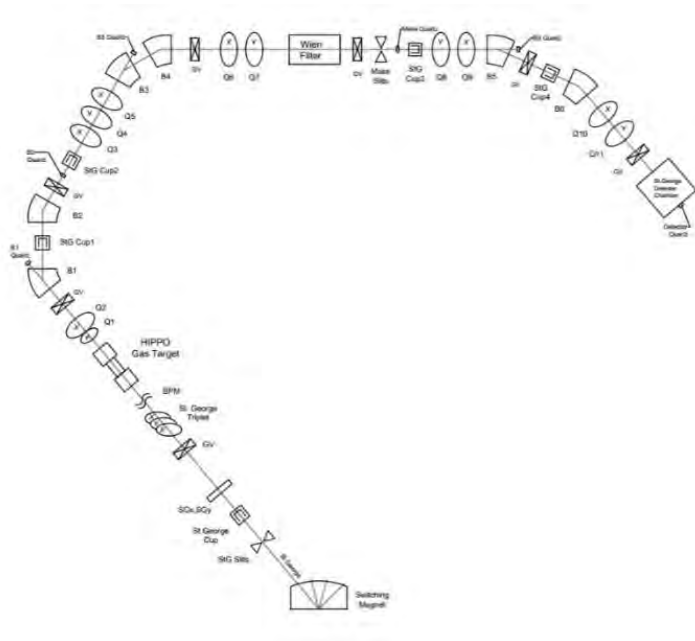


Figure 1 is a schematic of the St. George beam line. Everything that occurs before the HIPPO Gas target is used to assist in steering the beam into the target located in St. George

2. Problems and Procedures:

2.1 Angular Acceptance

The experiments that St. George is designed to perform, are expected to create reactants in very low quantities, approximately 1 part in 10^{15} [1]. This makes it necessary to accept the largest angular distribution of reactants possible, testing the maximum angles that particles could be traveling at to still be able to reach the detectors at the end of St. George is therefore crucial.

To determine the experimental angular acceptance, a plan was put in place to determine the transmission of particles with an angular spread of ± 40 mrad. The first component of this plan was to find a suitable source that would allow for meaningful data to be taken within a short amount of time. A very active americium source, which consistently released alpha particles was selected. The source was tested to determine the expected energy values for its released particles.

A collimator was then designed with the intent of limiting the angular spread of the source to ± 40 mrad and then tested. Using a silicon detector, it was determined how many alpha emissions were to be expected over a given time interval. This collimator-source component was then attempted to be inserted into the beam line of St. George through a linear motion device, located just past the HIPPO Gas target. However, unknown design constraints caused issues with its insertion.

Due to dimensional errors in its design, the component was too large to insert into the beam line, and was forced to be modified. Once inserted, a He 2+ beam was delivered to the St. George beam line from the 5U accelerator. The values of the dipoles were then modified to make sure that the beam was able to reach the end of St. George with minimal to no steering by the quadrupole magnets. It was then attempted to lower the source portion of the collimator into the beam line using the same linear motion device. Another design constraint, limited the insertion of the source completely into the beam line, so the collimator was carefully removed, modified, and reinserted. The He 2+ beam was then removed.

Using the values obtained from the testing of the americium source, and solid angle calculations the approximate number of expected counts was determined. Then using theoretical current values from the manufacturer of the quadrupoles, and COSY simulations, the current values controlling the magnetic field of the dipoles were modified to optimize transmission through St. George. Once these expected potentially successful values had been used, the best tune was selected and then modified. Using the linear motion device, the position of the collimator was changed by one millimeter increments to find the best possible transmission point.

A new He 2+ beam was then delivered to St. George from the 5U and the transmission of the beam was tested. The transmission percentage of the beam was determined using initial

values obtained from a Faraday Cup at the entrance to St. George and a second Faraday Cup located in the chamber at the end of the beam line.

Once the tests were completed with the new He 2+ beam, the collimated source was removed from the St. George beam line, allowing for additional tests to be run. With the design changed, the amount of expected counts was again recorded on the silicon detector. This time, the distance from the detector was varied to gain a better understanding of the angular spread provided by the collimator.

2.2 Quadrupole Magnetic Field Reproducibility

Since the majority of the magnets that compose St. George are quadrupoles, it is necessary to have the best possible understanding of the magnetic fields that they produce. Information coming from those designing the SEparator for CApture Reactions (SECAR) another recoil separator, commonly called the ‘Big Brother’ of St. George, which will be located at the Facility for Rare Isotope Beams (FRIB) at Michigan State University has brought light to the fact that common practices for reproducing the same magnetic fields from quadrupoles may not be adequate. The typical procedure for reaching a specific magnetic field for both quadrupoles and dipoles has been to ramp each magnet from zero current up to within five percent of its max current capacity, allow it to sit for at least five minutes, then lower that current to the correct value to produce the desired magnetic field. It is necessary to ramp down to the value rather than going from a lower field to a higher field due to the magnetic hysteresis. While this procedure does seem to still hold true for dipoles, the information from SECAR shows that it might not be adequate for quadrupoles.

To determine the best possible procedure for reproducing magnetic fields from quadrupoles a gauss meter was installed onto Q5. The current within Q5 was then repeatedly

modified to determine how different waiting periods affected its ability to reproduce the same fields. This procedure, was often began after the magnet had been sitting unused and without current for several hours.

3. Results

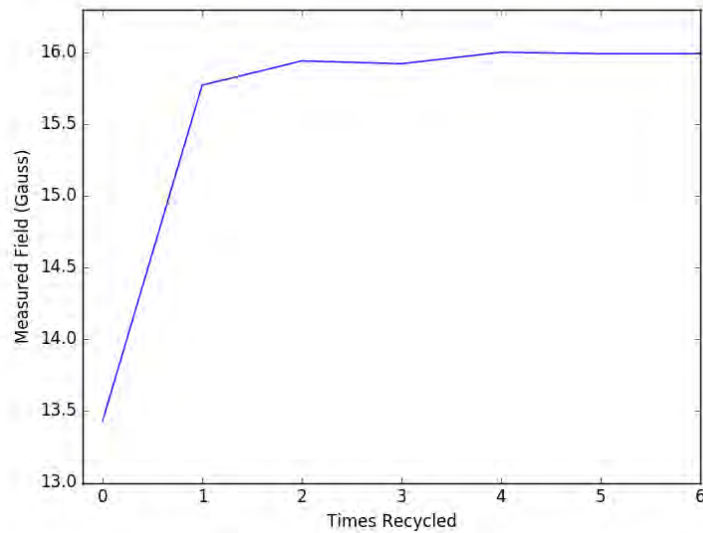
3.1 Angular Acceptance

Through testing various values for the quadrupole magnets a tune was found that allowed for an angular acceptance slightly larger than ± 40 mrad with the source alone. When tested with the actual He 2+ beam, this was found to not yield quite the same results. The tune allowed for complete transmission through the St. George beam line to the Faraday Cup located within the detector chamber. However, it did not allow for the complete angular acceptance. In three directions up, down, and right, complete transmission was detected with deflecting the beam up to 36 mrad however, when deflecting 36 mrad to the left only 45% transmission was detected.

3.2 Quadrupole Magnetic Field Reproducibility

Through studying the quadrupoles, patterns were recognized between magnetic field strength and the events proceeding it. It was determined, that the magnetic field produced by a quadrupole that has been sitting without current is consistent after the magnet has been recycled thrice, rather than the one iteration that is typically used, meaning the current is taken from zero to 95% to zero to 95% to zero to 95% and then lowered the desired value. Upon one recycling the magnetic field values produced were found to be vastly different, varying potentially by several gauss, particularly at lower currents. Upon recycling twice, the fields were much closer within several tenths of a gauss, and upon the third recycle the produced fields were found to be nearly identical.

Figure 2: The relationship between the amount of times that the quadrupole has been recycled in relationship to the measured magnetic field in the absence of an induced current.



4. Conclusion

4.1 Angular Acceptance

The angular acceptance testing discussed above, was nearly successful, with possible errors potentially explaining why 55% of the transmission was lost when deflecting left. When the beam was deflected 36 mrad to the left with the Faraday Cup removed the beam spot managed to stay visible on the two inch quartz viewer located at the rear of the detector chamber. This makes it likely, that the beam managed to be deflected 36 mrad, but instead of being detected by the Faraday Cup it was striking the outside of the cup.

During these tests, it was also shown that the triplet magnet was steering the beam as it entered St. George. The triplet is designed to help focus the beam as it exits the 5U and enters the St. George beam line, when it steers the beam line it makes it more difficult to ensure optimal positioning throughout the beam line. Realigning the triplet to eliminate the steering would likely make it easier to experimentally show angular acceptance in the future.

While not exactly an error, it should be noted that issues occurred with the 5U during these tests. Multiple times, when trying to determine the angular acceptance, the supplied beam slightly changed entry location within St. George requiring the lengthy process of obtaining non-steering through St. George to be performed multiple times. Moving forward, repeating the angular acceptance tests without the above issues would likely allow for the demonstration of complete angular acceptance.

4.2 Quadrupole Magnetic Field Reproducibility

Moving forward, it is strongly recommended that the quadrupole magnets be brought to the desired current value following the procedure outlined above. This has been demonstrated to be necessary when the quadrupole has been sitting without current for a period of time greater than a few hours.

References

- [1] M. Couder, G. Berg, J. Görres, P. LeBlanc, L. Lamm, E. Stech, M. Wiescher, J. Hinnefeld
Nucl. Instrum. Meth. A, 587 (2008), p. 35
- [2] Z. Meisel, M.T. Moran, G. Gilardy, J. Schmitt, C. Seymour, M. Couder
Nucl. Instrum. Meth. A, 850 (2017), p.48

Appendix

Shown below is the alpha transmission from the original tune and the final tune, along with their associated current values, in amps. The dipole and Wien Filter Values were unchanged during this experiment.

Component	Current	Field (Gauss)
B1	80.064	4167.7
B2	80.047	4192.2
B3	80.79	4210.8
B4	80.5	4177.1
B5	91.45	4024.5
B6	81.15	4142.5
WF	104.13	598.33

Component	Original	Final
Q1	37.9	31.56
Q2	52.5	54.05
Q3	29.55	33.04
Q4	21.3	41.37
Q5	35.086	35.88
Q6	12.2	13.23
Q7	0	0
Q8	30.9	27.31
Q9	49.36	52.83
Q10	59.7	62.62
Q11	48	48.58
Counts Per Second	0.071	2.46

Energy Resolution Difficulties of the Deep Underground Neutrino Experiment

James Frisby

2017 NSF/REU Program

Physics Department, University of Notre Dame

Advisor: John LoSecco

Abstract:

In this project, simulations were analyzed to determine energy uncertainties for the Deep Underground Neutrino Experiment due to unobserved neutrons produced from neutrino interactions. It was found that neutrons often carry a large amount of the total energy of an interaction but the amount varies considerably. This variation excludes the possibility of accounting for the neutron energy merely by relying on the simulations to calibrate the detector. As such, energy deposited in neutrons may complicate DUNE neutrino energy measurements.

Introduction:

The Deep Underground Neutrino Experiment (DUNE) is a proposed next generation neutrino oscillation experiment that will be based out of Fermilab. It will use the Fermilab particle accelerator to create the highest intensity neutrino beam yet built which will be directed to a detector approximately 1300 km away in South Dakota. The detector is planned to be a 40000 ton Liquid Argon Time Projection Chamber (LArTPC) located about 1.5 km underground to shield from cosmic rays. When a neutrino interacts inside the detector, a shower of particles is produced many of which leave ionization tracks which are detected by grids of wires. This means that LArTPCs are not well designed to detect neutrons, which do not leave ionization tracks.

Among the DUNE science goals is to study neutrino oscillation particularly as it relates to lepton CP violation. The 1300 km path length to the detector is ideal for studying the disappearance of muon neutrinos at 2.5 GeV. The beam is designed to maximize the number of muon neutrinos

at around that energy. There should be a drop in the number of muon neutrinos observed at this energy due to the initially muon neutrinos oscillating to electron and tau neutrinos. By measuring this muon neutrino disappearance and other related phenomena, the parameters governing neutrino oscillation can be more accurately determined. Knowing the values of these parameters may reveal CP violation if a particular parameter, δCP , is found to be non-zero.

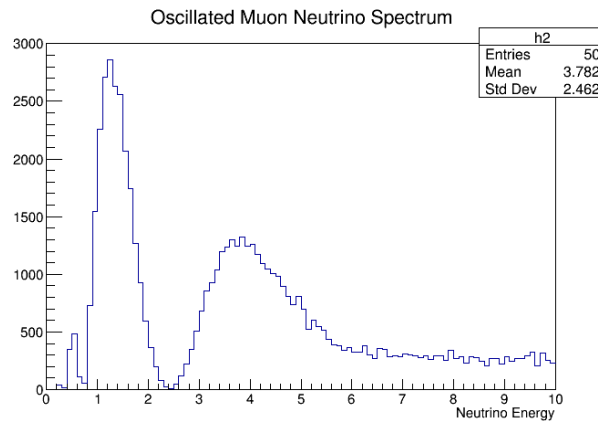


Figure 1. Oscillated Muon Neutrino Energy Spectrum

Since neutrinos oscillate as a function of their energy, the determination of the width of this muon neutrino disappearance will require knowledge of the neutrino energy in each event. However, the only way to know the energy of a neutrino is to measure the energies of all particles it produces when it interacts in the detector and refer to conservation of energy. This presents a major difficulty as the LArTPC detector relies on ionization and some of the daughter particles cannot be observed through this process. In this project, we investigate the effect of undetected neutrons on the neutrino energy measurements of the DUNE experiment.

Methods:

The experiment will not be operational for several years, but there do exist simulations of the detector. GENIE is a Monte Carlo neutrino event generator used by Fermilab which can be used to run simulations for the DUNE experiment by accounting for the neutrino spectrum of the DUNE experiment and the detector geometry. Simulations were run before the summer generating 100000 event samples for each of the neutrino flavors; during the summer, I analyzed the events produced from these simulations to investigate the potential energy measurement difficulties of the DUNE experiment. In simulations, one always can know the true energies of all the particles, a luxury obviously not available to the real experiment. If the simulation accurately models the experiment, then it could be used to attempt to calibrate the detector so that otherwise unseen particles are accounted for. I used ROOT to work with the data produced from the simulations.

At the beginning of the summer, we did not have convenient access to the width of the dip in muon detections shown in figure 1 above. We did however have access from the simulations to the spectrum as it would appear prior to oscillation. I used a program called Prob3++ to account for the oscillations which produced the spectrum shown in figure 1. Prob3++ generates neutrino oscillation probabilities which I multiplied the un-oscillated spectrum by to produce the oscillated spectrum.

Results:

The energy spectrum for neutrons produced during neutrino collisions in the detector is shown below in figure 2.

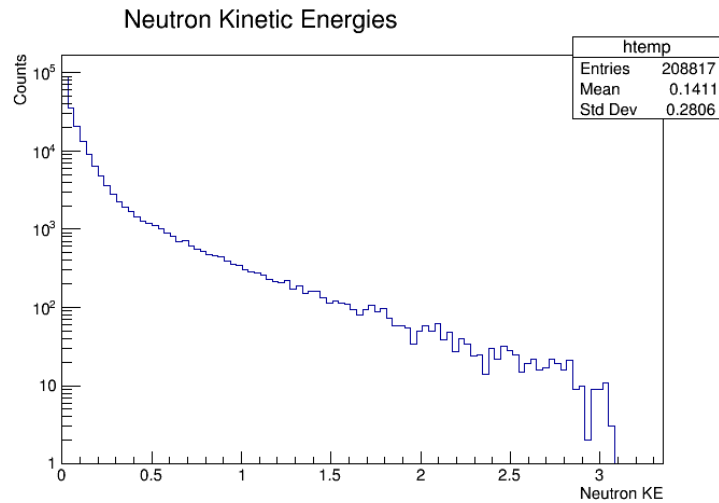


Figure 2. Neutron Kinetic Energies

Note that this is a log plot, so there are many more low energy neutron than high energy ones. However, the distribution is heavily skewed so the mean is 141 MeV with a standard deviation of 280 MeV. As most neutrinos are in between 2 and 3 GeV, missing 141 MeV of energy could be significant. However, those are the energies of individual neutrons. Figure 3 shows a histogram of the number of neutrons produced in each event.

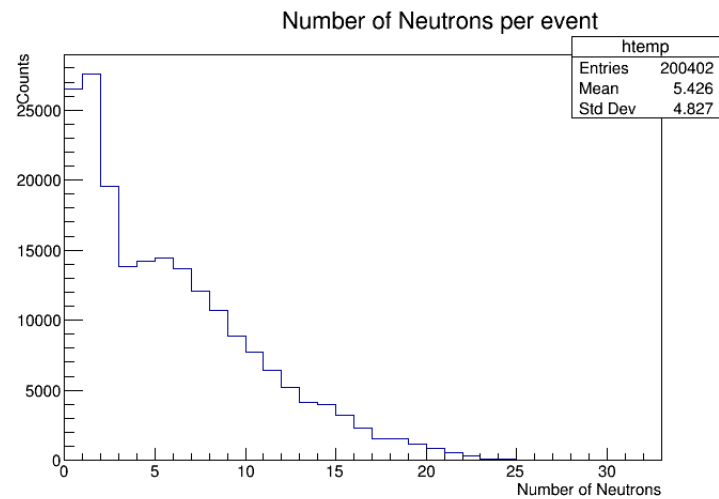


Figure 3. Neutron Multiplicities

Since there are many events which produce multiple neutrons, with a mean number of neutrons of 5.4, we then look at the sum of all energy that is deposited in neutrons for each event. From here on whenever I refer to “neutron energy” of an event I refer to this sum of all neutron kinetic energies in that event. Figure 4 shows a histogram of these energies.

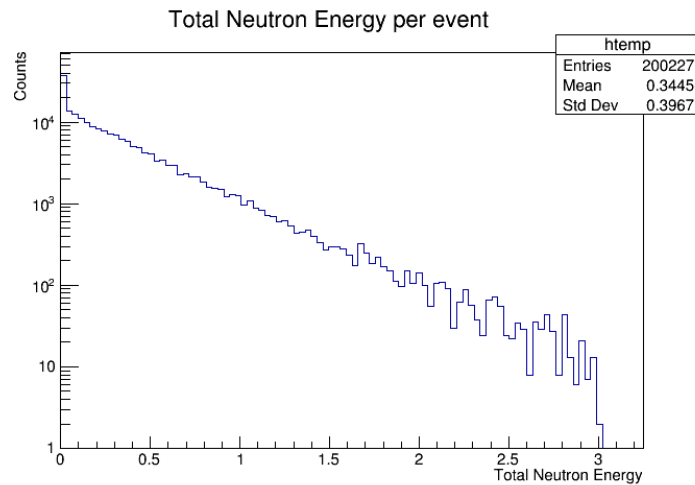


Figure 4. Sum of Neutron Energies

This is more worrying as the mean energy that is carried by neutrons is 345 MeV. This indicates perhaps up to 15% of a neutrino’s energy will be deposited as the kinetic energy of neutrons, which the DUNE LArTPC cannot directly detect.

Supposing that we trust that the simulation well approximates the amount of energy deposited in neutrons during these events, we could attempt to calibrate the detector to account for this average amount of lost energy. In each event we would have some observed energy from the particles other than neutrons and based on that energy we could add the mean amount of energy that was deposited in neutrons to estimate the true energy of the neutrino. Below is

shown the mean amount of neutron energy as a function of observed energy, where “observed energy” is the true neutrino energy minus the neutron energy.

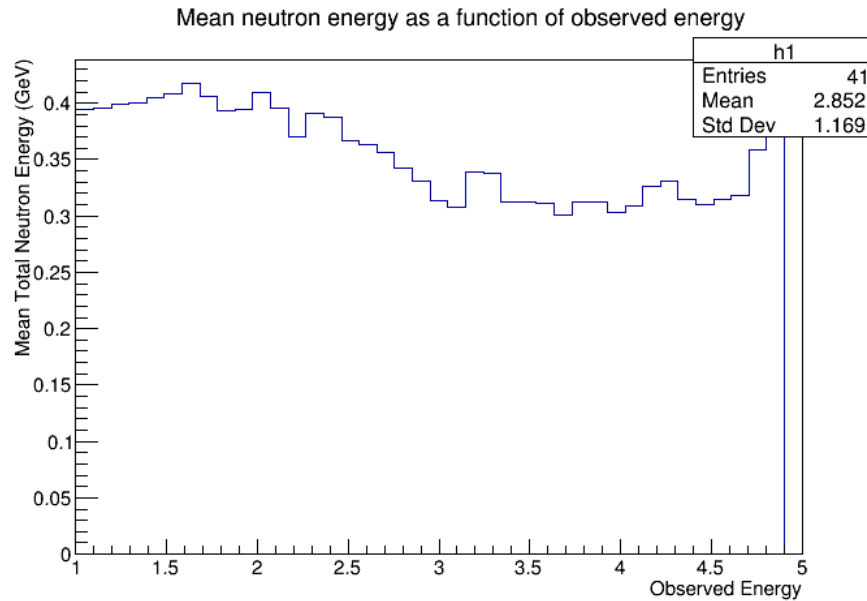


Figure 5. Mean Neutron Energies

This does assume near perfect measurement of the energies of all particles other than neutrons, which is of course highly unlikely but it is the best case scenario so long as neutrons are not observed. This shows the amount by which any one observation would be corrected by to attempt to account for unseen neutron energy.

However, there is of course variation in the neutron energies for each observed energy. The standard deviation of neutron energies was plotted as a function of observed energy, producing figure 6.

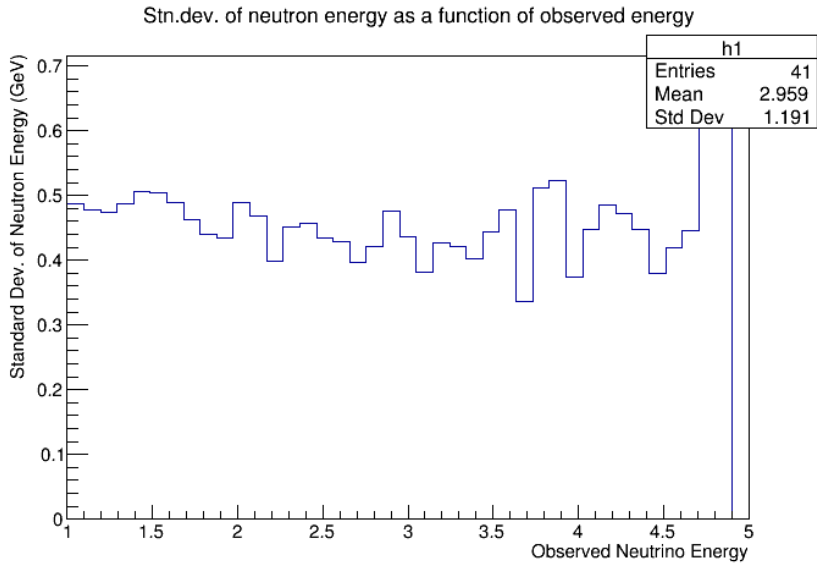


Figure 6. Standard Deviation of Neutron Energies

This shows that the standard deviation of the neutron energies for a given observed neutrino energy are approximately 400 to 500 MeV. That is the uncertainty associated with the attempt to account for unseen neutrons based on the simulation. This is very unfortunate for the DUNE experiment, as these uncertainties are on the order of 15% to 20% of the energies of the typical neutrinos.

We tried to get an idea for how damaging this would be by looking the resolution necessary to study muon neutrino disappearance at around 2.5 GeV. This is the dip shown in Figure 1. As mentioned previously, we did not initially have access to the approximate width of this dip. Prob3++ was used to produce the following estimation of oscillation probabilities for muon neutrinos staying muon neutrinos in the DUNE beam.

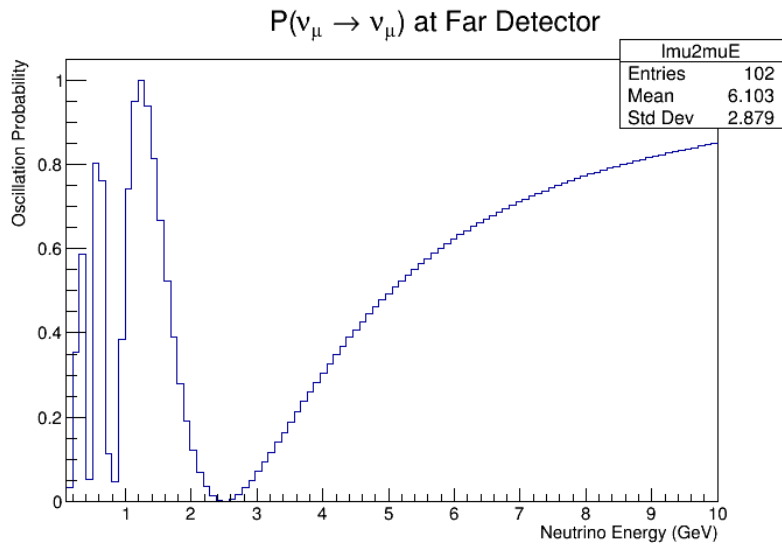


Figure 7. Muon neutrino survival probabilities

This was then multiplied by the un-oscillated neutrino spectrum (figure 8) obtained from Fermilab, shown below, to obtain the oscillated spectrum shown in figure 1.

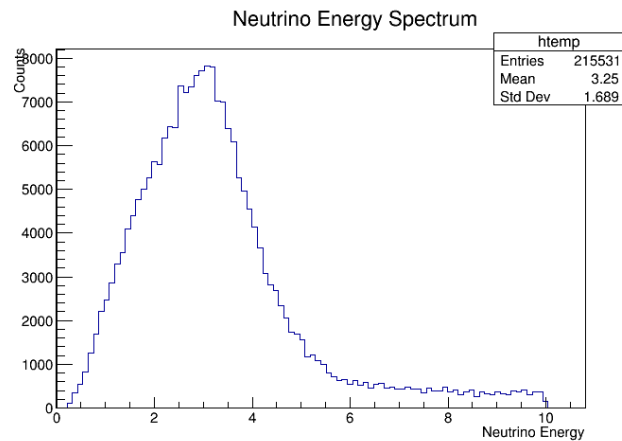


Figure 8. Un-oscillated neutrino energy spectrum

As the dip shown in figure 1 is a little under a GeV wide, but with many neutrino observations on either side, the uncertainties in neutrino energy caused by lack of neutron detection, approximately 400 to 500 MeV, would make fine investigation of muon disappearance

impossible. Events which belong on the left of the dip may be measured to be in the middle as would events which belong on the right.

Conclusion:

Accurate energy reconstruction will be necessary for DUNE to study neutrino oscillations. Since the DUNE detector will be a LArTPC, DUNE will have a weakness in measuring the energies of neutrons. Simulations indicate that the amount of energy deposited in neutrons varies significantly which prevents neutron energy being blindly accounted for from the simulation. The resulting uncertainty in energy resolution will provide a serious challenge for the experiment before it can accurately investigate neutrino oscillation and CP violation.

Acknowledgements and References:

Dr. LoSecco at Notre Dame for taking me as his research student and for his expertise in the field.

Drs. Tom Junk and Tingjun Yang at Fermilab for their assistance in the use of Fermilab software.

Dr. Umesh Garg and the Notre Dame physics for providing this REU opportunity.

LBNF/DUNE Conceptual Design Reports Vols. 1 and 2: <https://arxiv.org/abs/1601.05471>

<https://arxiv.org/abs/1512.06148>

COMMISSIONING OF A FARADAY CUP FOR THE
SOLENOID SPECTROMETER FOR NUCLEAR
ASTROPHYSICS (SSNAP)

EMMANUEL GARCIA

2017 NSF/REU Program
Physics Department, University of Notre Dame

ADVISOR:

Dr. Dan Bardayan

Abstract

The Solenoid Spectrometer for Nuclear Astrophysics (SSNAP) is a HELIOS-like helical orbit spectrometer being developed at the University of Notre Dame. Designed around position-sensitive silicon detectors set along the axis of the second *TwinSol* solenoid, it will improve our capacity to study nucleon transfer reactions. SSNAP will be sensitive to the charged light-ions produced in these reactions, improving our ability to understand the created residual nuclei. The study of nucleon transfer reactions gives us insight into many nucleosynthesis processes occurring in astrophysical events, such as novae bursts, neutron-star collisions, among others. This work focuses on the design and construction of a Faraday Cup detector that is part of recent developments of SSNAP. The preparation of titanium gas cell windows and deuterated-polyethylene targets to be used in *TwinSol* experiments is also reported.

1. Introduction

In the early stages of the universe, in the span of the first 10 to 1000 seconds after the Big Bang, only light nuclei up to lithium-7 were made [1]. Therefore, all the heavier elements that can be seen throughout the universe have since been made through multiple astrophysical nucleosynthesis processes. Among these we encounter neutron and proton capture processes, which open the door for the creation of a plethora of isotopes that then decay into heavier stable elements.

Through the use of transfer reactions, we are able to study the nuclear structure of the nuclei created by neutron and proton capture processes. By measuring the ejected light-ions produced by these reactions, we gain valuable information about the residual nuclei [2]. Understanding the structure and characteristics of these nuclei gives us insight into processes such as the s-process and r-process, and how they fit into our models of the astrophysical phenomena that initiate them.

Since the installment of *TwinSol* in 1998, it has been used for numerous experiments involving the use of Radioactive Ion Beams (RIB). A schematic of the current set-up is shown in Fig 1. The use of RIBs allows us to study reactions encompassing short-lived nuclei that would be unsuitable for targets since they would decay very rapidly. The RIBs produced by *TwinSol* are produced through the In-Flight method, in which a stable ion beam bombards a gas target and produces a “cocktail” beam with different nuclei, including the desired radioactive product [2]. The magnetic field of the solenoids is then used to focus the desired radioactive nuclei and separate it from the rest of the contaminants. However, since some of the nuclei share a similar momentum- to-charge ratio, and thus similar energies, it is possible that some of the contaminants remain in the beam.

SSNAP consists of an improvement to the current *TwinSol* device by outfitting the second solenoid as a helical spectrometer. This will broaden the scope of reactions in normal kinematics that can be studied with the device as well as providing several advantages such as better particle identification and large angular coverage.

A new Faraday Cup was commissioned as part of the SSNAP design in order to normalize the data. The design, installation and testing of the device, as well as the preparation of titanium gas cell windows and deuterated-polyethylene targets, is outlined in the present work.

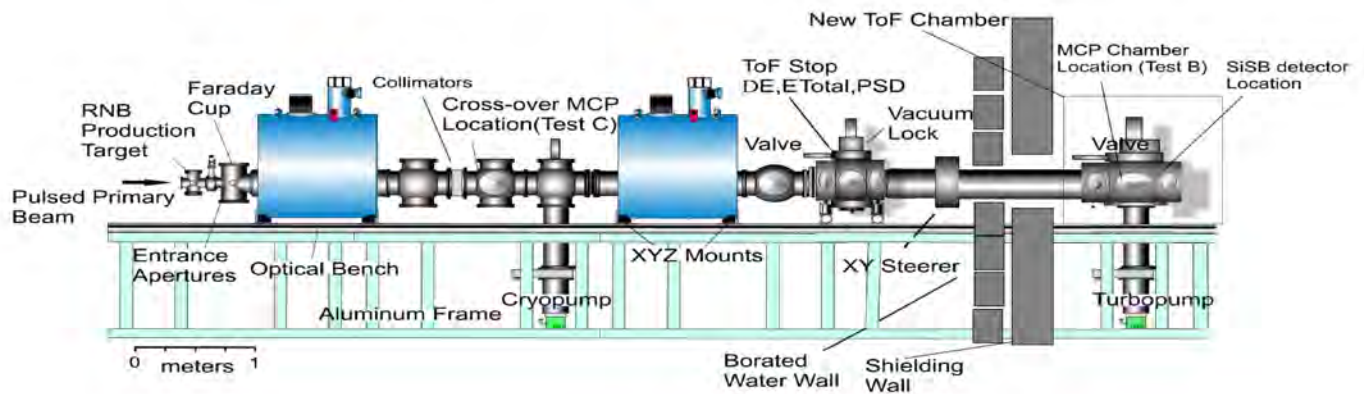


Fig. 1. Schematic representation of *TwinSol*, located at the University of Notre Dame Nuclear Science Laboratory.

2. Fundamentals of SSNAP

SSNAP is a helical spectrometer that would be located within the second solenoid of *TwinSol* system. Inspired by the HELIOS spectrometer located at the Argonne National Laboratory, it aims to study transfer reactions in the realm of normal kinematics. One of the main components of SSNAP consists of an aluminum frame holding a 0.76" x 0.76" square tubing, as seen in Fig. 2, to allow the beam to travel down axis. The frame can hold up to six Super-X3 position-sensitive silicon detectors and is devised to be inserted in the solenoid via the ISO-250 chamber that follows it. This was achieved by constructing the square tubing with the interlocking telescopic design shown in Fig 3, allowing the insertion in sequence of the individual pieces of the apparatus.

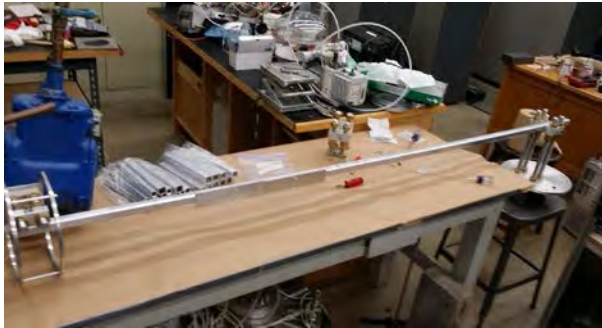


Fig. 2. Aluminum frame to be set inside the second solenoid of *TwinSol*.

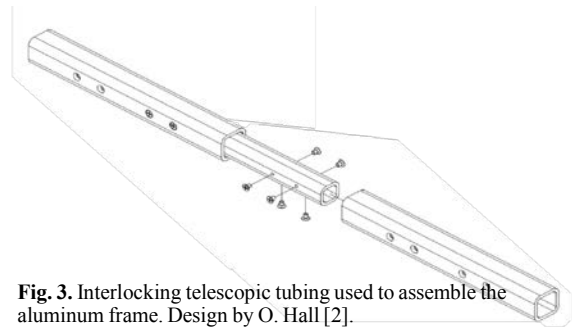


Fig. 3. Interlocking telescopic tubing used to assemble the aluminum frame. Design by O. Hall [2].

The target will be placed within the magnetic field produced by the solenoid. That way, when the RIB strikes the target, the ejected ions are subjected to the force of the field. This will cause the ions to travel in helical orbits around the solenoid in what is known as cyclotron motion. The path taken by the ejected ions is dependent on their charge-to-mass ratio, energy, and the ejected angle. As they travel in the helical orbit, the ejected particles will eventually strike one of the six position-sensitive silicon detectors located on the z-axis. A simplified depiction of this scenario is shown in Fig. 4.

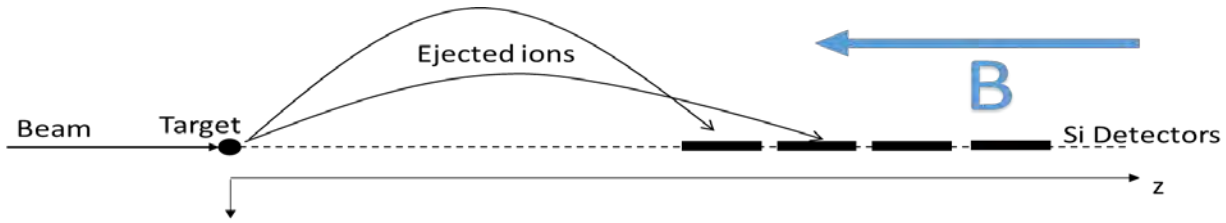


Fig. 4. Trajectory of the ejected ions after striking a target inside the solenoid. The ions will travel in a helical orbit until striking one of the six position-sensitive detectors located on the z-axis.

2.1 Advantages of SSNAP

Once the particles are detected by the position-sensitive silicon detectors, three quantities are measured by making use of the geometry of the system: the particle's energy in the laboratory frame E_{lab} , the position detected along the solenoid axis z , and the Time-of-Flight (ToF) of the ejected particle T_{OF} . From these measured quantities, the angle of emission θ_{lab} , and the energy

E_{cm} in the center-of-mass (CM) frame can be reproduced by the equations

$$\cos^2 \theta_{lab} = \left(\frac{E_{cm}}{E_{lab}} \sqrt{1 + \frac{2m_{target} E_{lab}}{m_{ion}^2 c^2}} \right) \quad (i)$$

$$E_{cm} = E_{lab} + \frac{1}{2} m_{ion} v_{cm}^2 \quad (ii)$$

where the value of the CM's velocity v_{cm} is fixed for a given beam energy and the magnetic field is fixed for the experiment.

Measuring the axial distance instead of the emitted angle provides its advantages by preventing kinematic compression of the excited states at higher angles. This allows for clearer separation of the states. It also allows for the full determination of the angular dependence of a reaction in one measurement [2]. In addition, with the new set-up the detectors are kept out of the path of the beam, reducing potential damage and providing large angular coverage.

Another advantage provided by SSNAP is easy particle identification. Since the orbital periods for different particles varies as a function of their mass-to-charge ratio, particle identification can be obtained by the ToF measurements. This is particularly useful for experiments

in which the particle energies are very low, as well as those that require high energy resolution, such as Q-value measurements, where traditional methods such as telescope detectors are not ideal [2]. However, it should be noted that this method is not without flaws; since various ions have the same mass-to-charge ratio, they will have the same ToF.

3. Faraday Cup

3.1 Theory

A Faraday Cup (FC) is a conductive cup designed to catch charged-particles in a vacuum. When a beam of ions hits the metal surface, the ions are neutralized while the cup gains a net charge. The FC can then be discharged, producing a small amount of current which is measured by an electrometer attached to the device. The amount of current measured is proportional to the amount of charge of the incident particle, which is quantized. Therefore, by measuring the electric current flowing through the metal cup, the number of ions being delivered by the ionized beam can be known. With proper design, a FC can measure currents as small as 10^{-14} A, which corresponds approximately to an ion flux of 10^5 ions/s [3].

In order to get an accurate reading, care must be taken for backscattered ions or secondary electrons that may be ejected from the cup when the ion beam strikes its surface. The escape of these ions results in a current overestimation for positively charged ion beams and current underestimation for negatively charged ones [4]. To avoid this problem, a suppressor with a negative voltage is usually placed in front of the FC. This induces an electro-static field which pushes the stray ions back to the cup.

3.2 Design Requirements

One of the requirements when designing the FC for SSNAP was the ability to be able to assemble and disassemble it from the beamline with ease, since the solenoids are still to be used for projects other than SSNAP. However, since it is to be placed in a chamber located after the solenoid, this did not present the same challenges as the other components of SSNAP, which are to be placed inside the solenoid and are therefore much more difficult to access and manipulate. Additionally, in order to get a good alignment with the beam, it had to be able to have linear vertical motion while limiting its rotational movement.

3.3 Design

Fig. 5 shows the mounted assembly of the FC. It consists of a cylindrical suppressor attached by insulating ceramic cylinders to the cup. It is essential that the suppressor and the cup are completely electrically isolated, otherwise voltage applied to the suppressor would impede the appropriate functioning of the cup. The cup is enclosed by a tantalum plate which receives the direct impact of the beam. Tantalum is characterized by its high conductivity and resistance to activation, making it an ideal choice for the FC. The whole ensemble was mounted in an aluminum frame that allows for the attachment to a linear drive. The linear drive consists of bellows of adjustable length, allowing suspension and alignment of the FC along the beam axis.

An ISO-250 flange was modified to attach the linear drive by using a CF (ConFlat) seal. Two BNC feedthroughs were also made in the flange for the suppressor and cup connections. Once the cup is installed into the ISO chamber, as shown in Fig. 5c, it can be easily set-up or removed from the beam axis by manipulating the actuator on the top of the chamber.

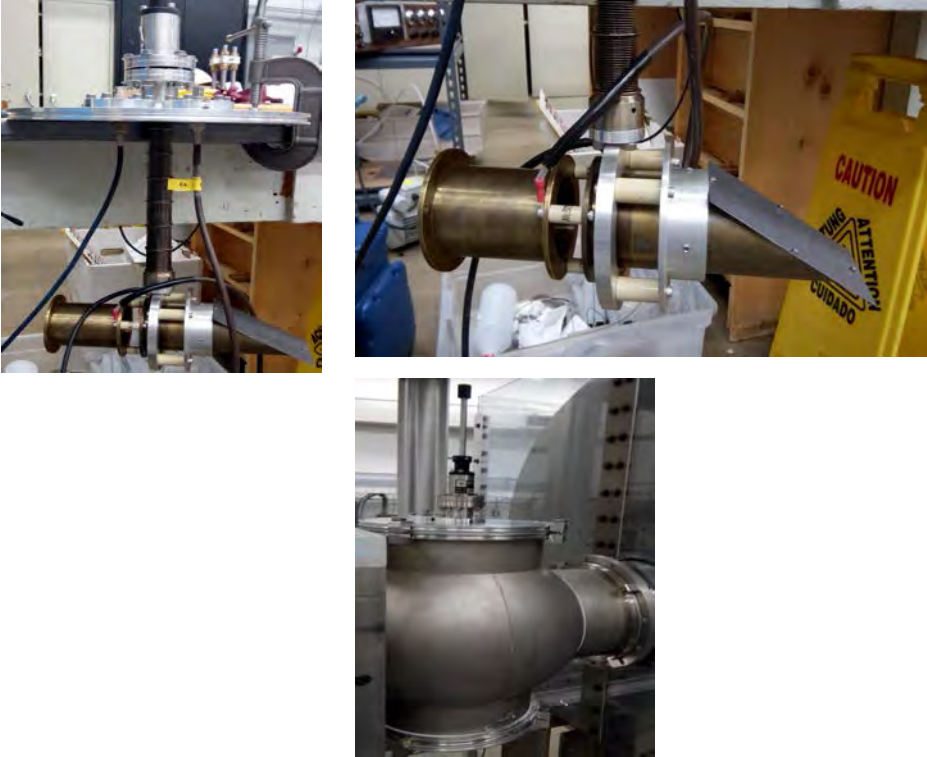


Fig 5. (a) FC fully assembled and attached to the modified ISO-250 flange. (b) Close-up of the FC. (c) FC assembled inside the ISO-250 chamber located after the solenoid.

3.4 Testing

The cup was assembled for testing in the four-way chamber located after the first solenoid. After proper alignment and pumping-down the whole ensemble into a vacuum, the solenoid was turned on and the RIB was focused into the FC. The electrometer connected to the cup picked up the electric current as the beam impinged on the cup, confirming that the FC was properly working. Afterwards, a voltage was applied to the suppressor, significantly increasing the amount of current measured by the cup. The voltage applied to the suppressor leveled off at 180V. This confirmed the proper functioning of the suppressor in redirecting stray ejectiles into the cup, as well as the proper insulation between the suppressor and the cup. The functioning of the FC was found not be affected by the magnetic field produced by the solenoid.

4. Gas Cell Windows

Many of the experiments carried out on the *TwinSol* facility involves the use of gas targets such deuterium to create RIBs. The gas is contained in gas cells enclosed by thin titanium foils. The foils have to thin enough so that the RIBs can pass through them with minimum scattering and energy loss, but strong enough to withstand the impact of the beam and pressure of the gas without breaking.

Following the procedure outlined in Ref. [5], circular and square titanium foils of initial thicknesses $5\mu\text{m}$ and $4\mu\text{m}$ respectively were rolled with a rolling mill down to thicknesses of $3\mu\text{m}$. We found that the $5\mu\text{m}$ circular foils produced a much better batch in comparison with the $4\mu\text{m}$ square foils, which were characterized by the presence of pinholes and lower reliability. It should be noted that the foils degrade over time, so a fresh batch have to be made for each experiment.

5. Preparation of deuterated-polyethylene targets

Although many of the low-energy nuclear physics experiments done with *TwinSol* employ gas deuterium targets for RIB production, some experiments benefit from the use of thin self- supported targets containing deuterium. The most commonly used deuterium-containing target is deuterated-polyethylene (C_2D_4) due to several favorable properties. It can be made into films with areal densities ranging from tens of $\mu\text{g}/\text{cm}^3$ to several mg/cm^3 . The thickness used requires a compromise between reaction yield and target-induced energy broadening. Furthermore, it ensures a favorable ratio (2:1) of deuterons to carbons, resulting in a favorable ratio of yield over energy loss. Finally, due to the relatively low Z of carbon, extraneous stopping power is minimized [6].

Various C_2D_4 targets were prepared using the technique described by M. Febraro, et al [6]. We used an alpha source of known energies to measure the energy loss of the alpha particles traversing the film. The thickness of the films was then calculated using the known stopping power of the alpha particles in C_2D_4 . The films prepared had areal densities ranging from $192\mu\text{g}/\text{cm}^3$ to $337\mu\text{g}/\text{cm}^3$, ideal for the energies used in our reaction studies.

6. Conclusions

The motivation and advantages of the helical spectrometer SSNAP were presented. The design, construction and testing of a new Faraday Cup to be used with SSNAP was introduced. The FC tests shows proper functioning in the measurement of current by the cup and the capture of stray ions by the suppressor. The magnetic field generated by the *TwinSol* was found to not interfere with the functioning of the FC. The preparation, uses and characterization of the titanium gas cell windows and deuterated-polyethylene targets to be used with *TwinSol* and/or SSNAP was presented. It was found that the $5\mu\text{m}$ circular foils rolled down to $3\mu\text{m}$ produced stronger and more reliable windows than the square $4\mu\text{m}$ foils.

7. Acknowledgments

I would like to thank Dr. Bardayan for having me as part of his team of researchers for the summer. I would also like to thank Dr. Patrick O'Malley for his invaluable help getting the project done and his patient and detailed explanations. Special thanks to Jerry Lingle for his help in designing the Faraday Cup, as well as Jacob Allen, Matthew Hall and Gabriel Brown for their assistance. Finally, special thanks Dr. Garg and the NSF for the hosting and funding of this REU program.

References

- [1] Keith A. Olive, Gary Steigman, Terry P. Walker, *Physics Reports* 333-334 (2000) 389 URL: <[https://doi.org/10.1016/S0370-1573\(00\)00031-4](https://doi.org/10.1016/S0370-1573(00)00031-4)>.
- [2] O. Hall "The Design of SSNAP and the implementation on an ion chamber for the characterization of radioactive ion beams", Master's dissertation, University of Surrey, 2016.
- [3] Robert B. Darling, Adi A. Scheidemann, K.N. Bhat, T.-C. Chen, *Sensors and Actuators A: Physical* 95 (2002) 84 URL: < [https://doi.org/10.1016/S0924-4247\(01\)00718-X](https://doi.org/10.1016/S0924-4247(01)00718-X)>.
- [4] A. Kashefian Naieni, F. Bahrami, N. Yasrebi, B. Rashidian, *Vacuum* 83 (2009) 1095 URL: <<https://doi.org/10.1016/j.vacuum.2009.01.005>>.
- [5] J.P. Greene and G.E. Thomas, Physics Div., Argonne National Lab. PHY-8557-HI-96 (1997) URL: <http://www.iaea.org/inis/collection/NCLCollectionStore/_Public/28/018/28018315.pdf>.
- [6] M. Febraro, D. Walter, S.C. Shadrick, S.D. Pain, K.A. Chipps, C. Thornsberry, E. Lesser, submitted for publication to *Nucl. Intr. and Meth. A* (2017) [Unpublished].

Identification of candidate metal-poor stars
from the HK survey by pruning with
the Gaia DR-1 data release

Notre Dame Physics REU

Jazmine Jefferson

Advisors:

Prof. Timothy Beers

Prof. Vinicius Placco

1. INTRODUCTION

It is widely known that details regarding the evolution of the Universe can be gleaned from studying the chemical composition of stars. Astronomers have been utilizing this knowledge for decades, studying stars to piece together information on the intrinsic properties of the Milky Way, such as its structure and origin. The chemical composition yields information concerning a star's formation era, since in their atmospheres, stars preserve information on the chemical and physical conditions of their natal clouds (Frebel et al. 2015). Studying the chemical composition of older, metal-poor stars has opened doors to a host of contemporary concepts in the field of astrophysics. This includes exploring the nature of the Big Bang and the nucleosynthetic processes that took place in the early Universe that lead to the formation of the first stars and galaxies.

1.1 METAL POOR STARS

Metal-poor stars are remnants of the early Universe. In its infancy, the Universe was composed of hydrogen and helium gases that compressed over a few hundred million years to form the very first generation of stars. These stars, denoted as population III stars, were massive and consequently lived short lives. In their death, these stars exploded into supernovae and dispersed the first metals into the interstellar medium. Population II, or metal-poor, objects are those with very low levels of metal relative to our Sun and were formed from the clouds of the first generation of stars. Population II as well as all subsequent generations of stars formed from chemically-enriched material from the previous generations'

nucleosynthetic processes. Metal-poor stars are therefore the oldest stars in the Universe and contain information about the chemical composition of their progenitor clouds in their atmosphere; these stars primarily exist in the inner and outer halo substructures in the Milky Way.

Stars are classified according to their abundance of metals (defined by astronomers as elements heavier than He) relative to our Sun. The abundance of an element uses the notation $[A/B] \equiv \log_{10} (N_A/N_B) - \log_{10} (N_A/N_B)_\odot$, where N_A and N_B denote the number of atoms of elements A and B. Fe has traditionally been taken as a reference element to enable comparisons of the metallicity of one star with another, quantified as $[\text{Fe}/\text{H}]$ (Beers et al. 2005). Metal-poor stars are classified as having a metallicity $[\text{Fe}/\text{H}] < -1$. A table of metallicity nomenclature as suggested by Beers et al. follows.

$[\text{Fe}/\text{H}]$	Term	Acronym
$> +0.5$	Super metal-rich	SMR
~ 0.0	Solar	—
< -1.0	Metal-poor	MP
< -2.0	Very metal-poor	VMP
< -3.0	Extremely metal-poor	EMP
< -4.0	Ultra metal-poor	UMP
< -5.0	Hyper metal-poor	HMP
< -6.0	Mega metal-poor	MMP

Table 1 Metallicity nomenclature suggestions by Beers et al. (2005)

1.2 CEMP STARS

Metal-poor stars with high carbon to iron ratios are considered carbon-enhanced. Carbon-enhanced metal-poor stars (CEMP) stars are defined by Beers et al. to have a carbon to iron abundance ratio $[\text{C}/\text{Fe}]$ of $> +1.0$. The fraction

of metal-poor stars that are carbon-enhanced increases at lower metallicities. CEMP stars constitutes roughly 20% of metal-poor stars with $[\text{Fe}/\text{H}] \leq -2.0$ while only a few percent of stars similar to the Sun are carbon-enhanced. The prevalence of CEMP stars at lower metallicities suggests that the chemical composition of the Universe had higher levels of carbon at the time of the star formation. Examples of current theories that explain this abundance of carbon include: a primordial process from massive progenitor stars, internal production from low mass, extremely metal-poor stars, or production from stars of intermediate mass, which was then transferred to a lower mass companion (Beers et al. 2005).

CEMP stars are further divided into subclasses based upon their neutron capture processes. Heavy nuclei beyond Fe are produced through neutrons merging with nuclei in high-energy astrophysical sites such as supernovae and neutron-star mergers. The subclasses of neutron capture for CEMP stars are depicted in Table 2.

Neutron-capture-rich stars	
r-I	$0.3 \leq [\text{Eu}/\text{Fe}] \leq +1.0$ and $[\text{Ba}/\text{Eu}] < 0$
r-II	$[\text{Eu}/\text{Fe}] > +1.0$ and $[\text{Ba}/\text{Eu}] < 0$
s	$[\text{Ba}/\text{Fe}] > +1.0$ and $[\text{Ba}/\text{Eu}] > +0.5$
r/s	$0.0 < [\text{Ba}/\text{Eu}] < +0.5$
Carbon-enhanced metal-poor stars	
CEMP	$[\text{C}/\text{Fe}] > +1.0$
CEMP-r	$[\text{C}/\text{Fe}] > +1.0$ and $[\text{Eu}/\text{Fe}] > +1.0$
CEMP-s	$[\text{C}/\text{Fe}] > +1.0$, $[\text{Ba}/\text{Fe}] > +1.0$, and $[\text{Ba}/\text{Eu}] > +0.5$
CEMP-r/s	$[\text{C}/\text{Fe}] > +1.0$ and $0.0 < [\text{Ba}/\text{Eu}] < +0.5$
CEMP-no	$[\text{C}/\text{Fe}] > +1.0$ and $[\text{Ba}/\text{Fe}] < 0$

Table 2 Definition of subclasses of CEMP stars

Most heavy elements can only form in a rapid neutron capture, or r-process. R-process occurs when neutrons are captured more rapidly than the rate of beta

decay. Similarly, s-process, or slow neutron capture, occurs when neutrons are captured at a slower rate than that of beta decay. Eu is used as a reference element because its abundance is one of the most readily available spectra to measure in metal-poor stars. It is necessary and useful to distinguish stars with “pure” r- or s-processed elements and stars that have element abundances with both, known as r/s-processed. CEMP stars with no strong overabundances of either r- or s-processed elements are dubbed CEMP-no stars.

2. SURVEYS OF THE STARS

2.1 HK OBJECTIVE PRISM SURVEY

In 1978, George Preston and Steve Sheckman of the Carnegie Observatory performed a survey in an effort to identify candidates for metal-poor stars in our Galaxy. This survey made use of an objective prism plate and an interference filter to successfully isolate CaII H and K lines and obtain low-resolution spectra of stars several magnitudes fainter than previously achieved (Beers 2015). Roughly 60 plates were visually scanned and followed up with medium-resolution spectroscopy for further analysis by Beers (Beers et al. 1985).

This survey was expanded by Beers with 240 additional prism plates from the northern and southern hemisphere using the Curtis and Burrell Schmidt telescopes. Each HK plate contains thousands of low-resolution spectra that were visually scanned to find the best metal-poor candidates; a large fraction of these plates have been followed up with medium-resolution spectroscopies.

2.2 GAIA-ESO SURVEY

The Gaia mission is to allow astronomers to investigate the origin and subsequent evolution of the Milky Way through providing an accurate astronomical census of over 1 billion stars. The first data release in 2013, DR-1, contained astrometric parameters and the average photometry from 1.14 billion stars surveyed in its first six months of operation (Mora et al. 2017). Stellar parameters logged in DR-1 include information on parallax, proper motions, distances from stars down to magnitude $V = 20$. The release has been made public and is readily available for cross-matching with other surveys.

3. IDENTIFYING CANDIDATE CEMP STARS

3.1 HK PLATES

The HK telescopes surveyed 2800 deg² and 4100 deg² of the northern and southern hemisphere, recording widened objective-prism spectra of up to thousands of stars at once. Prints of the plates were visually scanned with a 10-X microscope for CaII H and K lines in search for metal-poor candidates. Figure 1 illustrates the appearance of these lines as seen by the classifier.

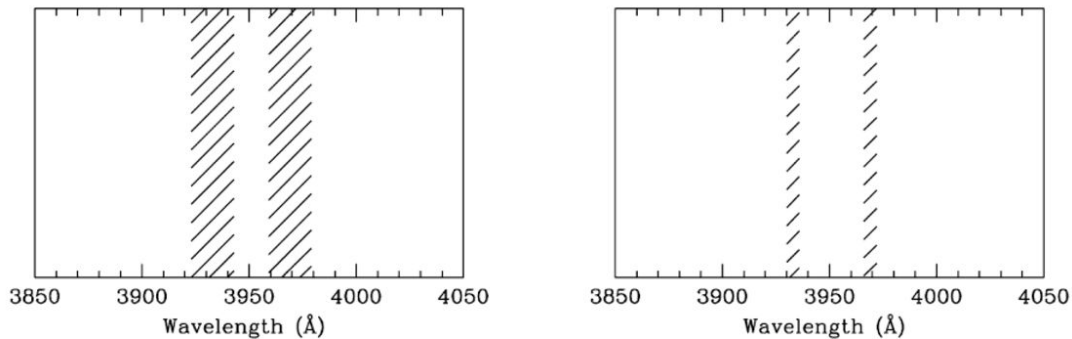


Figure 1 Illustration of appearance of CaII H and K lines as seen by visual classifier (Beers 2017)

Candidates of metal-poor stars as well as stars used for calibration of the coordinate system were marked and indexed by hand onto the plate prints. An example of one of these prints is shown in Figures 2 and 3.

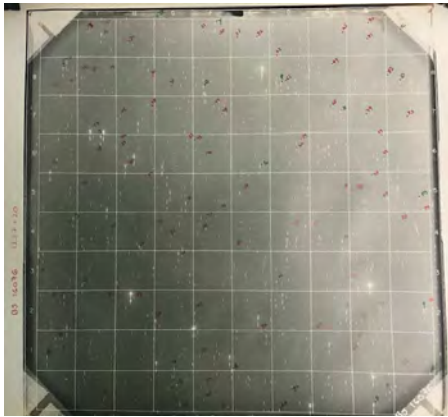


Figure 2 Full prism plate print

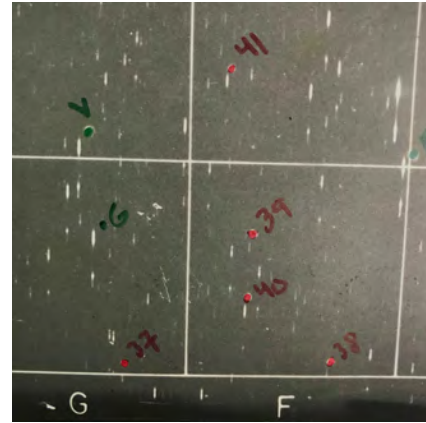


Figure 3 Portion of plate with marked candidate (red) and calibration (green) stars

The positions of the targets from the HK survey are relatively inaccurate, with some plates having over 10 arcseconds of error. The curvature of the telescope lens also creates a parabolic fit onto the plate and further distorts the coordinates of the targets. To obtain more accurate positions of the stars, .fit files of each individual target were created and analyzed through SAOImage DS9. Right ascension and declination in decimal degrees were logged for roughly 14,000 targets. The updated coordinates were uploaded to Centre de Données astronomiques de Strasbourg (CDS) X-match Service to crossmatch HK targets to stars obtained from Gaia DR-1.

3.2 ANALYSIS

Data compiled from the CDS X-Match Service included photometry and information on astrometric parameters such as the parallax, proper motions, and distance from the galactic center in addition to the positions of each candidate. The catalogue of candidates are then pruned to locate those most likely to be CEMP stars. Stars in the foreground of the survey are those within the galactic disk and are therefore less likely to be metal-poor. To increase the efficiency of locating CEMP stars, calculations were made to locate stars above the galactic plane (Z).

$$Z = d\sin(b) \tag{1}$$

Where d denotes distance from the galactic center, b denotes the galactic latitude, and μ denotes total proper motion that is used in calculating the transverse velocity; metal-poor stars exist primarily in the halo system and will consequently have higher relative transverse velocities.

$$V_T = 4.74\mu d \tag{2}$$

4. RESULTS AND CONCLUSIONS

4.1 RESULTS

The CDS X-match service successfully matched roughly 1200 stars with all necessary data for calculations. Many of the candidate stars have been observed since the HK selection process; stars that have been observed were logged. Stars were further classified according to their metal-poor candidacy, with 1 being best.

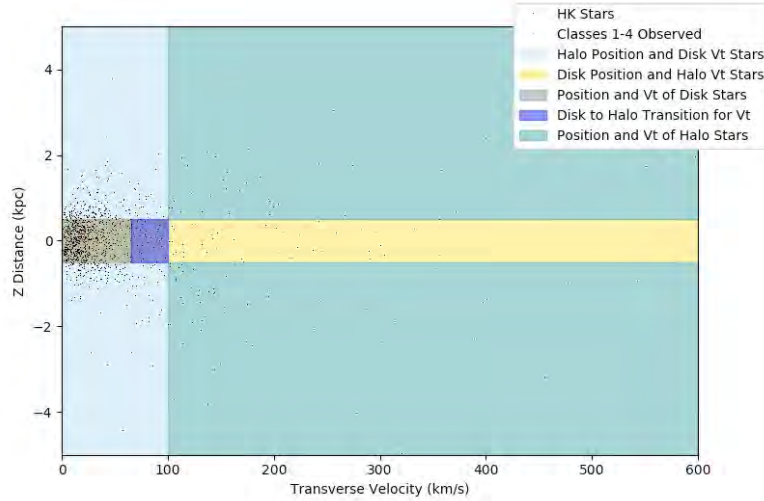


Figure 4 Plot of all HK stars (black) and stars of classes I-IV Z vs V_T that have been observed

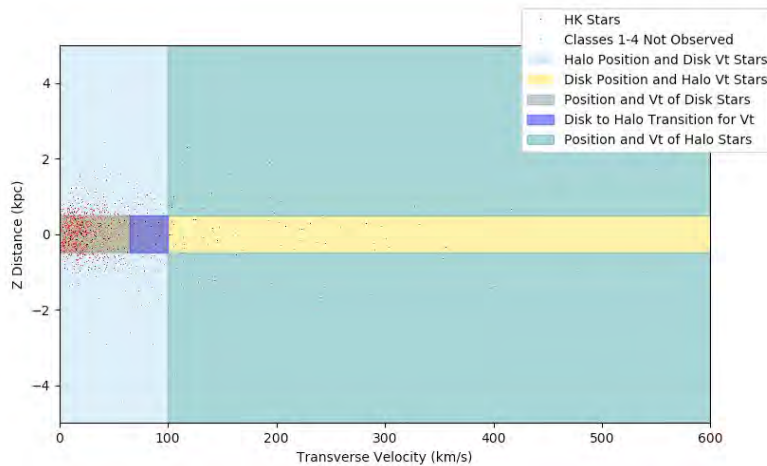


Figure 5 Plot of all HK stars (black) and stars of classes I-IV Z vs V_T that are not yet observed

Plots of the stars' distances from the galactic plane as a function of their transverse velocities is ideal for quickly eliminating foreground objects as candidates. The face of the plot is color-coded according to the positions and transverse velocities of both the halo and disk of the Galaxy. The stars remaining in the HK survey will undergo a similar identification process before both sets of data will have metallicities

assigned. The success rate of finding CEMP stars through the reported pruning method will then be determined.

REFERENCES

Beers, T. C. *et al.* The Discovery and Analysis of Very Metal-Poor Stars in the Galaxy. *Annual Review of Astronomy and Astrophysics* **43**, 531–580 (2005).

Beers, T. C. Back to the Future: The Calcium HK Survey of Beers, Preston and Shectman. *Fifty Years of Wide Field Studies in the Southern Hemisphere: Resolved Stellar Populations of the Galactic Bulge and Magellanic Clouds* **491**,140 (2015).

Frebel, A *et al.* Near-Field Cosmology with Metal-Poor Stars. *Annual Review of Astronomy and Astrophysics* (2015).

Mora, A *et al.* The Gaia Archive. *Astrometry and Astrophysics in the Gaia Sky. Proceedings IAU Symposium No. 330* (2017).

Beers, T. C. “The Oldest Stars.” *Astrophysics Update 2*, Springer Berlin Heidelberg, 2017.

Beers, T. C., Preston, G. W., & Shectman, S. A. 1985, *AJ*, 90, 2089

Determining the Effect of Stellar Evolution on Carbon Abundances

David Kalamarides

University of Notre Dame

Email: dkalamar@nd.edu

Carbon-Enhanced Metal-Poor (CEMP) stars are believed to be the direct descendants of the first generation of stars to be formed in the universe. Detailed chemical abundances of CEMP stars are important inputs for theoretical models, and the effects of stellar evolution on some of these abundances must be accounted for. Since the carbon content of these stars can decline as they age, it is necessary to correct observed measurements back to the initial conditions. We have refined the procedure for which we estimate corrections for carbon and nitrogen abundance ratios ([C/Fe] & [N/Fe]) from a large sample of observed stars from the Sloan Digital Sky Survey. After adjusting the models to match the observed data, new estimations were made from a Locally Weighted Scatterplot Smoothing (LOESS) regression function, which estimates [C/Fe] & [N/Fe] from a number of other parameters that are easier to identify in stars, such as surface gravity, effective temperature, and metallicity. An online tool was created so the public can run these calculations for any data.

Received 10 August 2017

1. INTRODUCTION

Metal-poor stars, especially those with high concentrations of carbon, have been identified by recent studies to be central to the understanding the chemical evolution of our galaxy.

Carbon-Enhanced Metal-Poor (CEMP) stars are classified as having a low iron-to-hydrogen (i.e. $[\text{Fe}/\text{H}] < -2.0$) and a high carbon-to-iron ratio (i.e. $[\text{C}/\text{Fe}] > +1.0$) [2]

CEMP stars can be subdivided based on the source of their enrichment. CEMP star whose heavy elements were produced by r-process are classified as CEMP-r stars and identified by $[\text{Eu}/\text{Fe}] > +1$. Enrichment can also come from a mass transfer by a binary red-giant. These stars are classified as CEMP-s stars and identified by $[\text{Ba}/\text{Fe}] > +1$ and $[\text{Ba}/\text{Eu}] > +0.5$. When $0 < [\text{Ba}/\text{EU}] < +0.5$, the CEMP star can be enriched by both r- and s- processes and classified as CEMP-r/s.[2] The final classification of CEMP stars are those whose enrichment must have come from carbon abundant natal gas clouds.

In this paper, we revisit the depletion of surface carbon abundances occurring in CEMP-no stars during the upper red-giant branch stage of evolution as originally done in Placco et Al. 2014 [6]. Figures 1 and 2 demonstrate the depletion of carbon and

enrichment of nitrogen as CN processing occurs. Using the same stellar evolution models [3], we improve the accuracy and efficiency of the online calculator as well as add $[\text{N}/\text{Fe}]$ to the stellar parameters used to calculate these carbon corrections. In addition, we now provide corrections for the change in surface nitrogen that occur concurrently with the carbon depletion.

This paper is structured as followed. Section 2 discusses the original work, Placco et Al. 2014, which this work is correcting. It outlines the original procedure and the errors that it faced. Section 3 discusses the new procedure which successfully corrects for both carbon depletion and nitrogen enhancement in the red-giant branch. Section 4 analyzes the possible errors. We discuss the online calculator and our results in Section 5.

2. ORIGINAL WORK

Placco et Al (2014) began by creating an array of models using the STARS stellar evolution code [3]. This array set parameters for metallicity, carbon, and nitrogen abundances. $[\text{Fe}/\text{H}]$ was set to -1.3, -2.3, -3.3, and -4.3. $[\text{C}/\text{Fe}]$ ranged from -1.0 to 3.0 in steps of 0.5. $[\text{N}/\text{Fe}]$ ranged from -1.0 to 2.0 also in steps of 0.5. These models were then evolved through the pre main-sequence to the end of the red-giant branch.

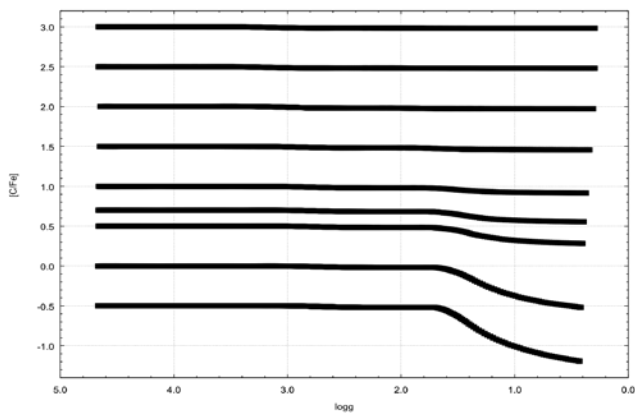


FIGURE 1. The carbon abundances of simulated stars against $\log g$ show the depletion of carbon through the red-giant branch. $[\text{Fe}/\text{H}]$ is held at -1.3 and $[\text{N}/\text{Fe}]$ at 0.0 .

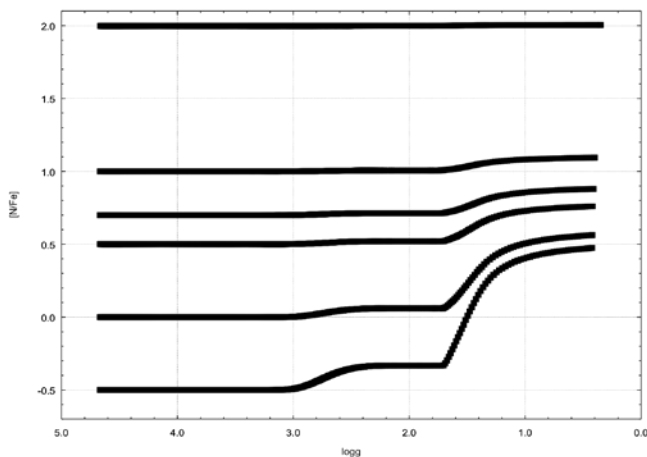


FIGURE 2. The nitrogen abundances of simulated stars are shown against $\log g$. $[\text{Fe}/\text{H}]$ is held at -1.3 and $[\text{C}/\text{Fe}]$ at 0.0 . The spike in nitrogen is due to the CN processing.

Placco et Al then collected a sample of metal-poor stars with high-resolution spectroscopies from the most recent SAGA database [7] and data assembled by Frebel et Al (2010)[5]. Stars which had already been identified as CEMP-s or CEMP-r/s were excluded from this data. After comparing the literature data and the observed, Placco et Al noticed a disparity between the surface gravity of the two. $\log g$ was shifted in all models by 0.5 to account for this difference.

Placco et Al's method for correcting carbon depletions is as follows. They began by taking four of the simulated models: those with the closest metallicity $[\text{Fe}/\text{H}]$ and carbon abundance $[\text{C}/\text{Fe}]$. Surface gravity ($\log g$) and nitrogen ($[\text{N}/\text{Fe}]$) were matched as closely as possible. The appropriate correction for each of these models was then determined. The final correction was calculated through a linear interpolation of these four models. This method is visualized in figure 3

This method ran into two main issues. First, any star outside of the simulated models' original parameters

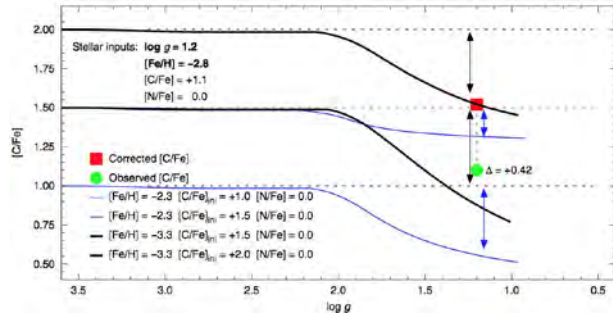


FIGURE 3. Procedure use in Placco et al (2015) [6]. Each vertical line represents the correction for a certain chosen model. The final correction is interpolated from these four lines.

(i.e. $[\text{Fe}/\text{H}] > -1.3$ or < -4.3 , $[\text{C}/\text{Fe}] > 3.0$ or < -1.0 , or $\log g > 4.5$ or < 0.3) would have an increasing potential error the further it was from the models. In other words, this method could accurately interpolate, but could not extrapolate. Second, nitrogen abundances were rounded off to the nearest 0.5 , causing a large increase in uncertainty. In addition, the change in nitrogen as a function of change in surface gravity through each model's evolution is entirely ignored. It is for these two reasons that we create a new procedure for calculating both carbon and nitrogen corrections.

3. PROCEDURE

To predict the changes in carbon and nitrogen, we use two locally weighted scatter plot smoothing (LOESS) regression models[4]. These models take a least squares regression from subsets of data of the stellar models from the STARS Stellar Evolution code [7], that is it fits a curve to minimized the uncertainty for each data point in the subset. These subsets are parameterized by a certain span set for each model. This span is for the carbon correction model and for the nitrogen. Then once given the observed parameters of surface gravity ($\log g$), iron abundance ($[\text{Fe}/\text{H}]$), carbon abundance ($[\text{C}/\text{Fe}]$), and nitrogen abundance ($[\text{N}/\text{Fe}]$), we predict the changes in carbon and nitrogen through the two LOESS regression curves. Figures 7 and 8 depict the calculated corrections for a grid of given parameters.

4. UNCERTAINTY

1000 points of sample data to test the carbon and nitrogen corrections were randomly selected from the simulated models. Seen in figure 4, the carbon corrections are calculated for each point and compared. Figure 5 shows the distribution of error between the calculated initial carbon abundance and the set parameter for initial carbon. The mean error is $8.663116\text{e-}4$ with a standard deviation of $1.649867\text{e-}2$. Nitrogen similarly has a mean error of $6.076169\text{e-}4$ and

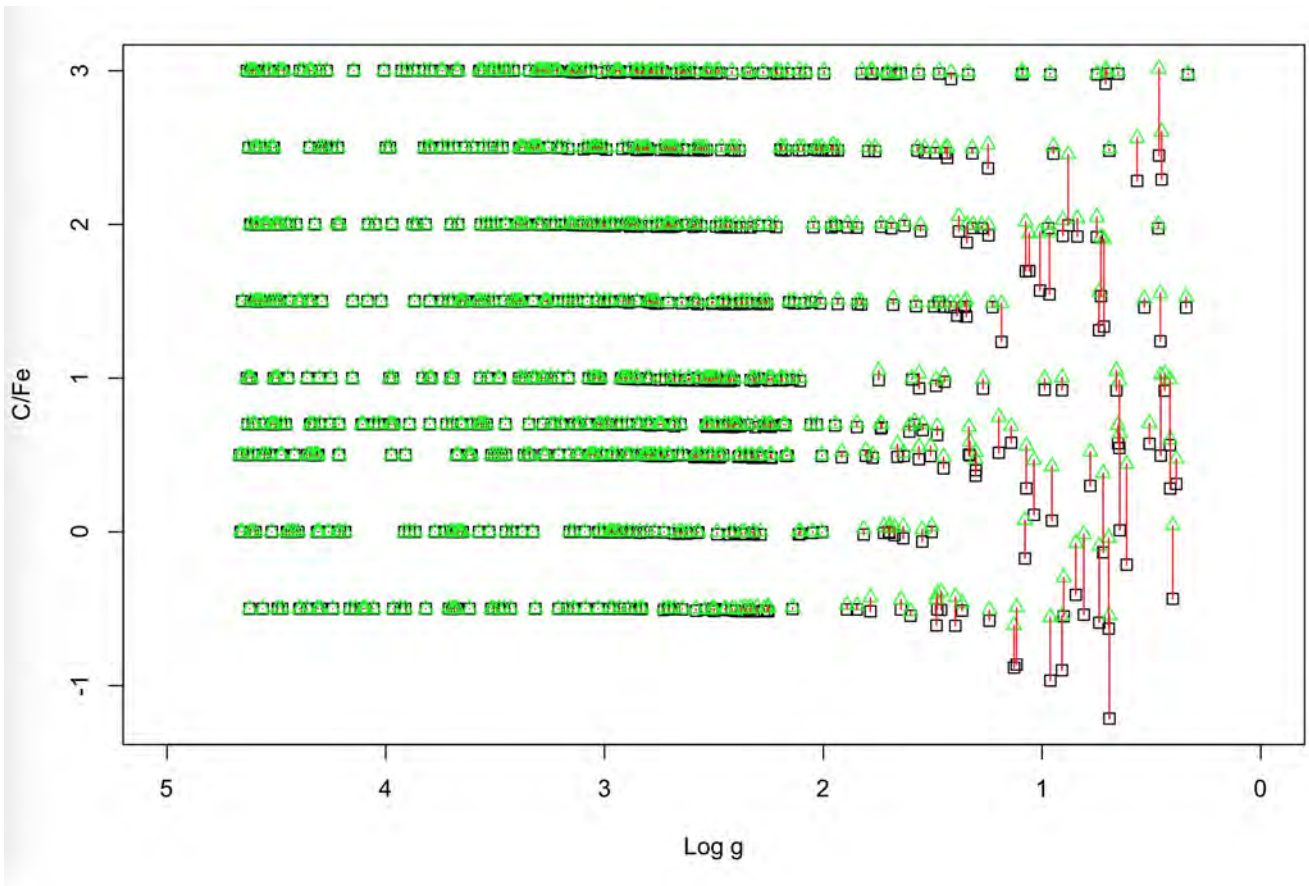


FIGURE 4. Carbon abundance corrections for sample data. Black squares indicate the observed carbon. The red lines represent the calculated correction while the green triangles show the final returned carbon abundances.

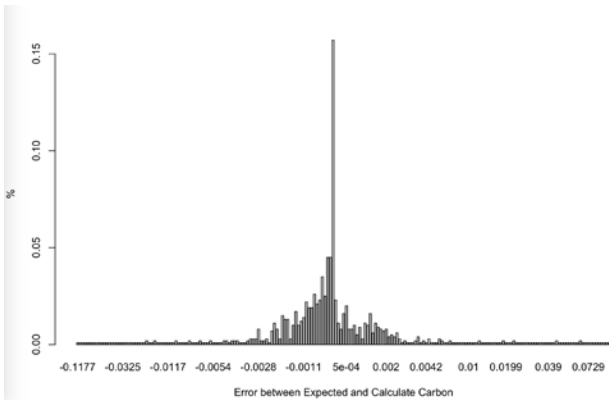


FIGURE 5.

a standard deviation of $7.187593e-2$.

This sample indicates that calculations indeed match the simulated models from the STARS evolution code.

5. CONCLUSIONS

This new method for calculating corrections for carbon and nitrogen through the red-giant branch allows for further work to occur with increased accuracy. One subject in particular that will benefit from these

updated corrections is the estimated frequency of carbon enhanced stars within our galaxy. These frequencies are vital as inputs for chemical evolution models of our galaxy. In addition, stars with carbon abundance slightly less $+1.0$ than can be confirmed as CEMP-no stars. There have been disputes over whether the lower limit to classify stars as carbon enhanced or not should be at $+1.0$ or $+0.7$ [1], as many stars between the range of these numbers exhibit properties of CEMP stars. It is likely that when carbon depletion is accounted for, it will be revealed that these stars were indeed carbon-enhanced at their creation. One star from the literature data that was processed in Figure, CS30322-023, has an observed carbon abundance of $[C/Fe] = 0.67$, but a calculated initial carbon abundance of $[C/Fe] = 1.688$. This drastic shift indicates that many stars that previously were ignored ought to be considered for CEMP frequencies within our galaxy.

In order to allow these future studies to occur, we have also created an online tool so anyone may correct their observed carbon and nitrogen measurements. The tool takes all needed parameters in through an uploaded .csv file, and processes them through an Rscript running on the server's terminal.

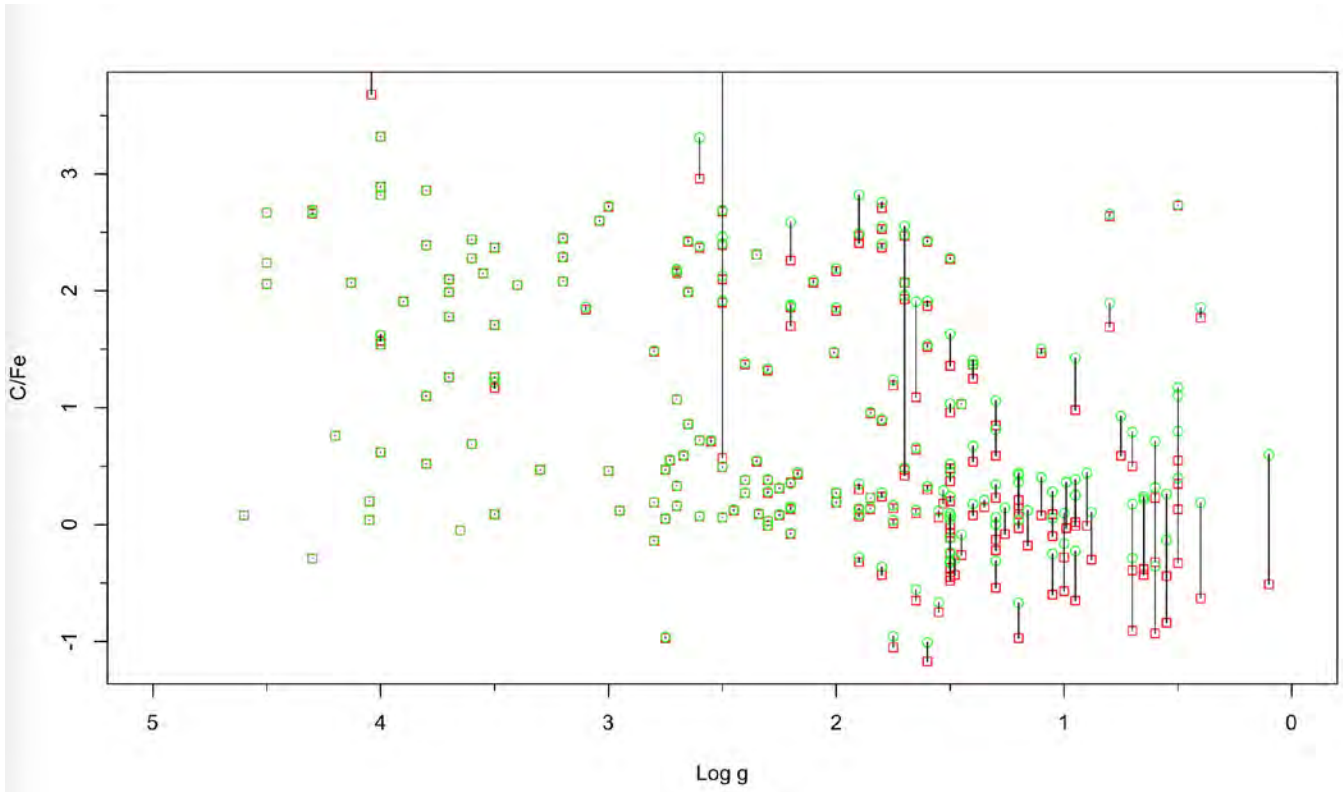


FIGURE 6. Carbon abundance corrections for literature data[5, 7]. Red squares indicate the observed carbon. The black lines represent the calculated correction while the green circles show the final returned carbon abundances.

6. FINAL THOUGHTS

This paper represents the culmination of my summer research with the University of Notre Dame's summer Research Experience for Undergraduate program. Additional work is still required to smooth the nitrogen corrections, prepare this paper for publishing, and releasing the public online tool. Since I am still a Notre Dame student, I will continue to work on these three projects in the coming semester.

While re-designing a method for correcting carbon and nitrogen was the main project I independently worked on, I also assisted in three other projects. First, I compiled a pipeline from UVES, a high resolution spectrograph of the Very Large Telescope (VLT) array located in Cerro Paranal, Chile. Throughout the summer, I was then responsible for reducing spectrum for which the Galactic Archeology team needed. Second, I assisted in creating the GQ index, an updated for calculating the carbon abundances in stars by integrating over the g-band in an observed spectrum. This is an improvement on the previously used GP and GPE indices as this new method first subtracts out any dip in flux in the g-band found in spectra of stars with near-zero carbon. Third, I have begun work on developing a pipeline for the South African Large telescope. This data reducing program will allow other astronomers from all over the world to analyze working spectra from this telescope.

Finally, the online web tool should be published at <https://www3.nd.edu/~vplacco/carbon-cor.html> within the coming year, dependent on the Office of Information Technologies' clearance to add back-end processing to Dr. Vinicius Placco's web page.

REFERENCES

- [1] Aoki, W., Beers, T. C., Christlieb, N., et al. 2007, ApJ, 655, 492
- [2] Beers, T. C., & Christlieb, N. 2005, ARA&A, 43, 531
- [3] Eggleton, P. P., Tout, C., Pols, O., et al. 2011, Astrophysics Source Code Library, ascl:1107.008
- [4] Cleveland, W. S. , Grosse, E. and Shyu, W. M. (1992) Local regression models. Chapter 8 of Statistical Models in S eds J.M. Chambers and T.J. Hastie, Wadsworth & Brooks/Cole.
- [5] Frebel, A., Kirby, E. N., and Simon, J. D. 2010, Natur, 464, 72
- [6] Placco, V. M. et Al (2014). Carbon-Enhanced Metal-Poor Star Frequencies in the Galaxy: Corrections for the Effect of Evolutionary Status on Carbon Abundances. Astrophysics Journal, 797, 21
- [7] Suda, T., Katsuta, Y., Yamada, S., et al. 2008, PASJ, 60, 1159(Page 19).

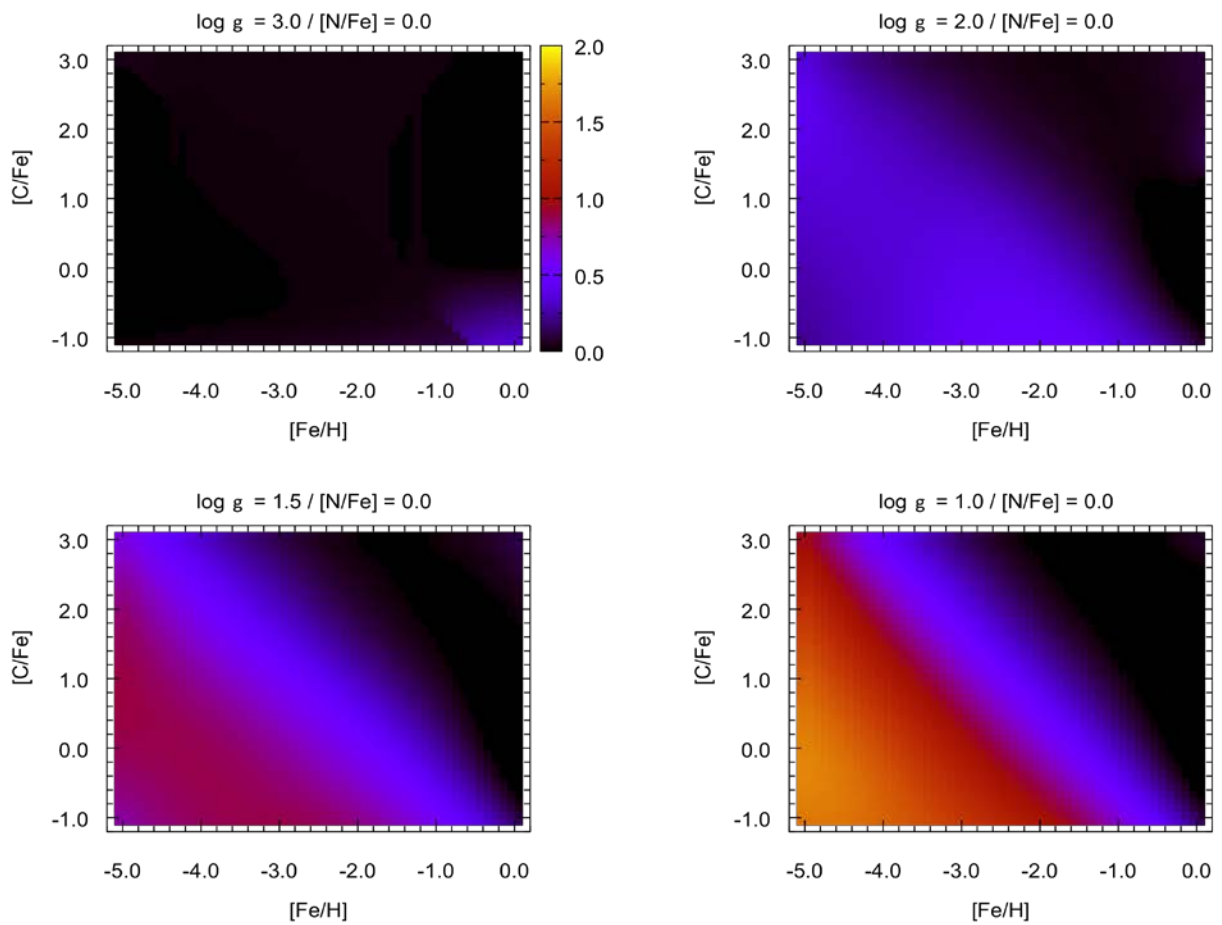


FIGURE 7. $[C/Fe]$ correction map for $\log g = 3.0, 2.0, 1.5,$ and 1.0 with $[N/Fe]$ fixed at 0.0

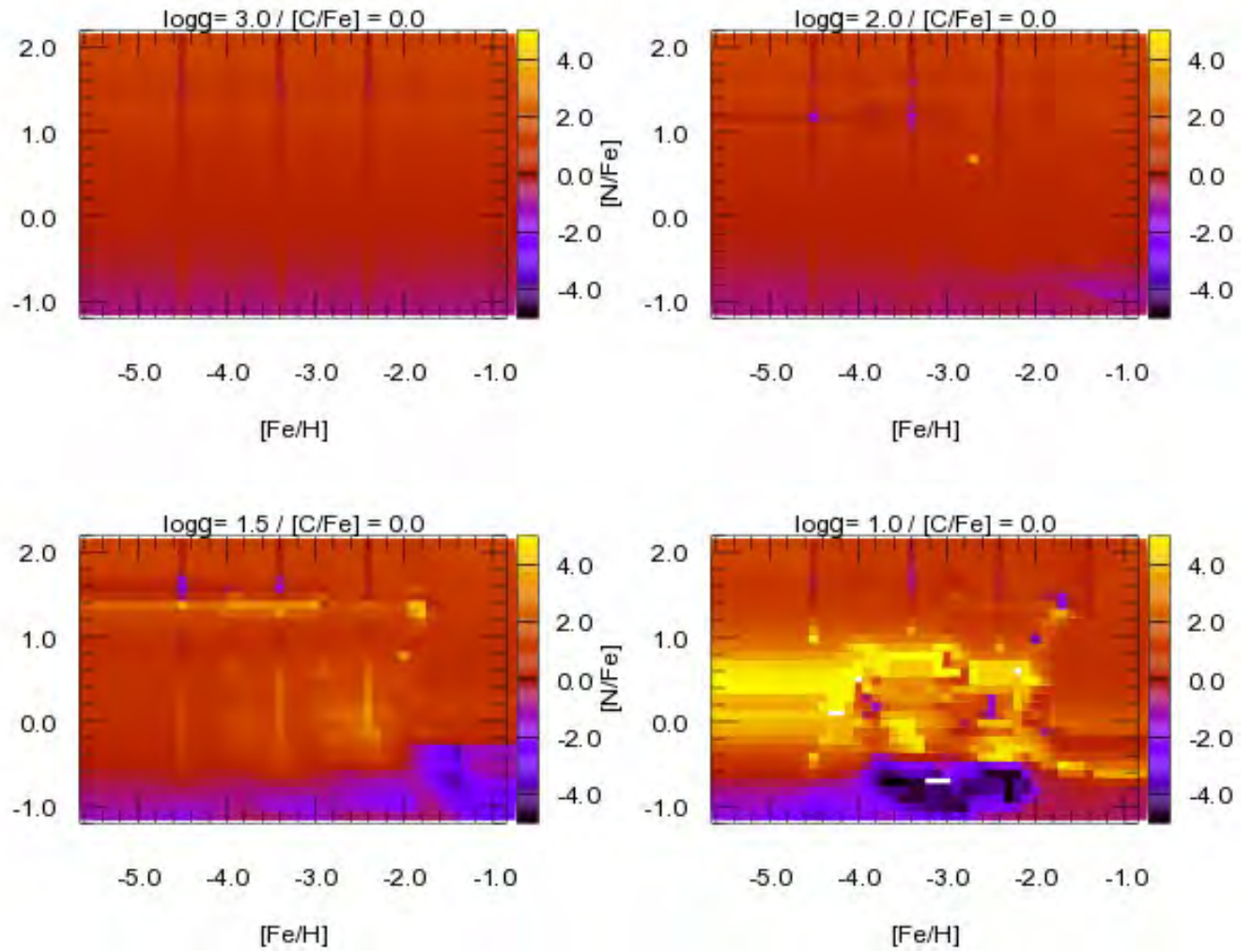


FIGURE 8. $[N/Fe]$ correction map for $\log g = 3.0, 2.0, 1.5,$ and 1.0 with $[C/Fe]$ fixed at 0.0

Analysis of Colonial Paper Currency

Michael Kurkowski, Catherine Cangany, Louis Jordan, Khachatur Manukyan, Zachary Schultz,
Michael Wiescher

Abstract

This project entailed studying the cellulose in paper, the ink, colorants, and other materials used to produce American colonial currency. The technique primarily used in this project was X-Ray Fluorescence Spectroscopy (XRF). XRF mapping was used to provide both elemental analysis of large-scale objects as well as microscopic examination of individual pigment particles in ink, in addition to the inorganic additives used to prepare paper. The combination of elemental mapping with Fourier Transform Infrared (FTIR) and Raman Spectroscopies permits an efficient analysis of the currency. These spectroscopic methods help identify the molecular composition of the pigments. This combination of atomic and molecular analytical techniques provided an in-depth characterization of the paper currency on the macro, micro, and molecular levels. We have identified several of pigments that were used in the preparation of inks and colorants. Also, different inorganic crystals, such as alumina-silicates, have been detected in different papers. The FTIR spectroscopy allowed us to determine the type of cellulose fiber used in the production of paper currency. Our future research will be directed toward revealing important historical relationships between currencies printed by different printers throughout the colonies.

Introduction

Throughout the eighteenth century, paper making was a growing profession. Standardized currency in the American Colonies did not exist yet, so individual printers

purchased their paper from paper mills in the same way as everyone else. Original paper manufacturing methods involved linen and cotton rags as the raw materials. Not until late in American colonial times were mica crystals used in banknote paper production as an anti-counterfeit strategy.¹

Once printers had the paper, they needed to turn it into viable currency. The very first bills were printed by the Massachusetts Bay Colony to prevent bankruptcy due to military expeditions.² Without any tough-to-replicate designs, bills were relatively quickly and easily counterfeited. One of the first printers to establish anti-counterfeiting methods was Benjamin Franklin, with ink designs from leaves. Another common technique to prevent counterfeiting was interspersing small mica crystals throughout the banknote paper.

Our method of analysis involved XRF Spectroscopy, which bombards a sample with a beam of x-rays. The secondary x-rays produced by the sample are specific to the elements within it; thus, the energies detected from the secondary x-rays identify the elements producing them. This was very useful in identifying the composition of many of the written inks, especially red ink.

FTIR spectra were taken on each of the currency bills to confirm the XRF spectra and to detect lighter elements (additives, etc.) that were undetectable by XRF. It was also used to confirm the presence of mica crystals in certain papers. FTIR is a technique similar to XRF, but uses a different electromagnetic wavelength. It shines a beam of infrared light at the sample, and detects the resultant energy produced by the vibration of the molecules.

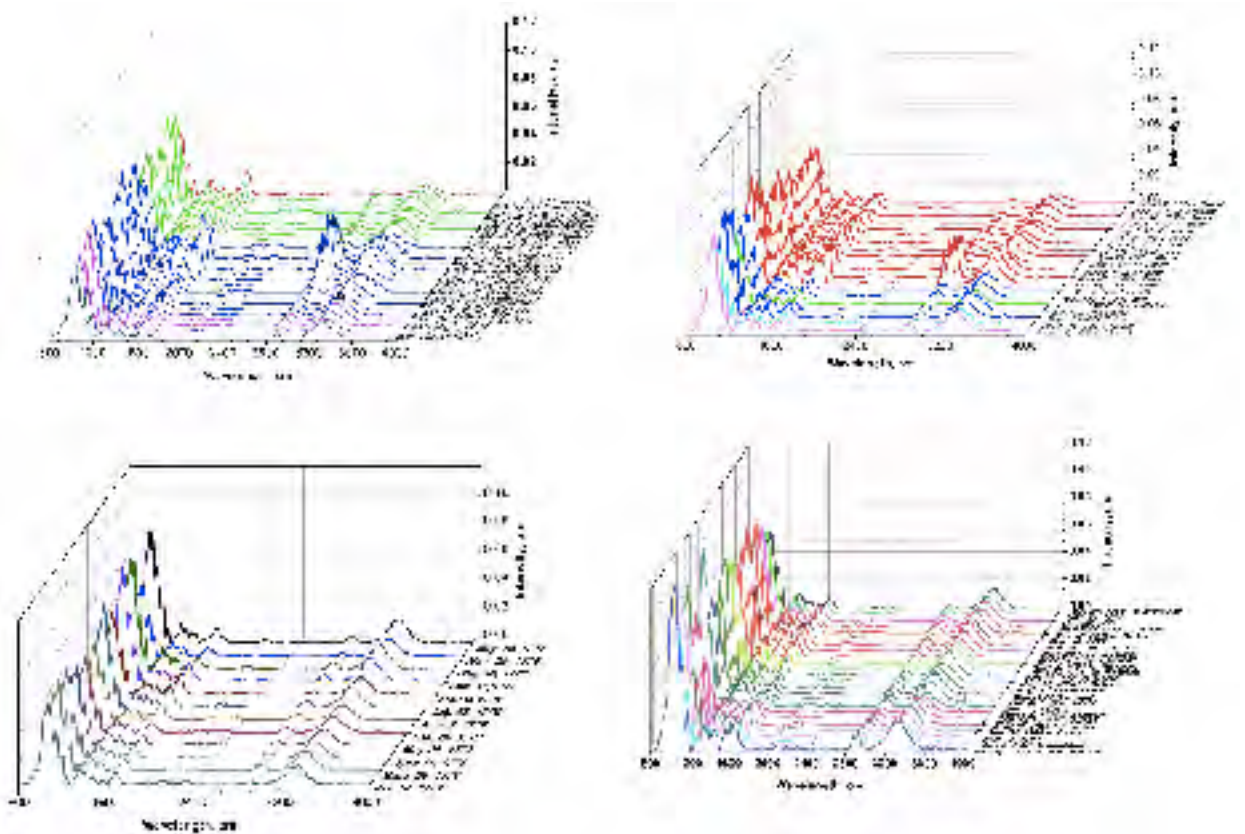
One of the inks that couldn't be fully analyzed by just XRF due to the presence of lighter elements was the printed black ink. To confirm the existence of carbon (which is expected to be found in bone black ink), I performed Raman spectroscopy on the bills, and found the characteristic carbon peaks. Raman is a sister technique to FTIR, the difference between them being that Raman shines a different wavelength of light: visible light (a red laser).

¹ American Paper Mills, 1690-1832

² <https://www.uscurrency.gov/content/history-american-currency>

To this end, the project was born, and was mostly conducted during the months of June and July 2017 at the University of Notre Dame.

Data & Findings



FTIR scans of paper over the years: Pennsylvania (top left), New Jersey (top right), Continental Currency (bottom left), and New York (bottom left).

Over the eighteenth century, the additives used in banknote paper changed depending on the source the currency printers used. One notable difference can be seen in the New Jersey graphs (top right), in which the paper contained an additive that manifested itself for only a couple of years, 1762-1765. This same additive can also be seen in the Pennsylvania graphs (top left) immediately after Franklin stopped printing currency, from 1769-1772, shortly after New Jersey. Other more subtle changes in the paper can be seen, which give deeper insight into currency printing and paper making methods of the time.

Conclusion

The ability to use all three techniques, XRF, Raman, and FTIR, allowed us to gain a new insight into the ways currency was produced in the colonies throughout the eighteenth century. XRF single-point analysis gave clearer knowledge as to the contents of banknote ink, providing a map of the contents of the various inks used in the production of a single bill of currency. Coupling this technique with Raman and FTIR allowed us to verify the data the XRF gave us, and to see the history and progression of materials used alongside with the full contents of each single currency.

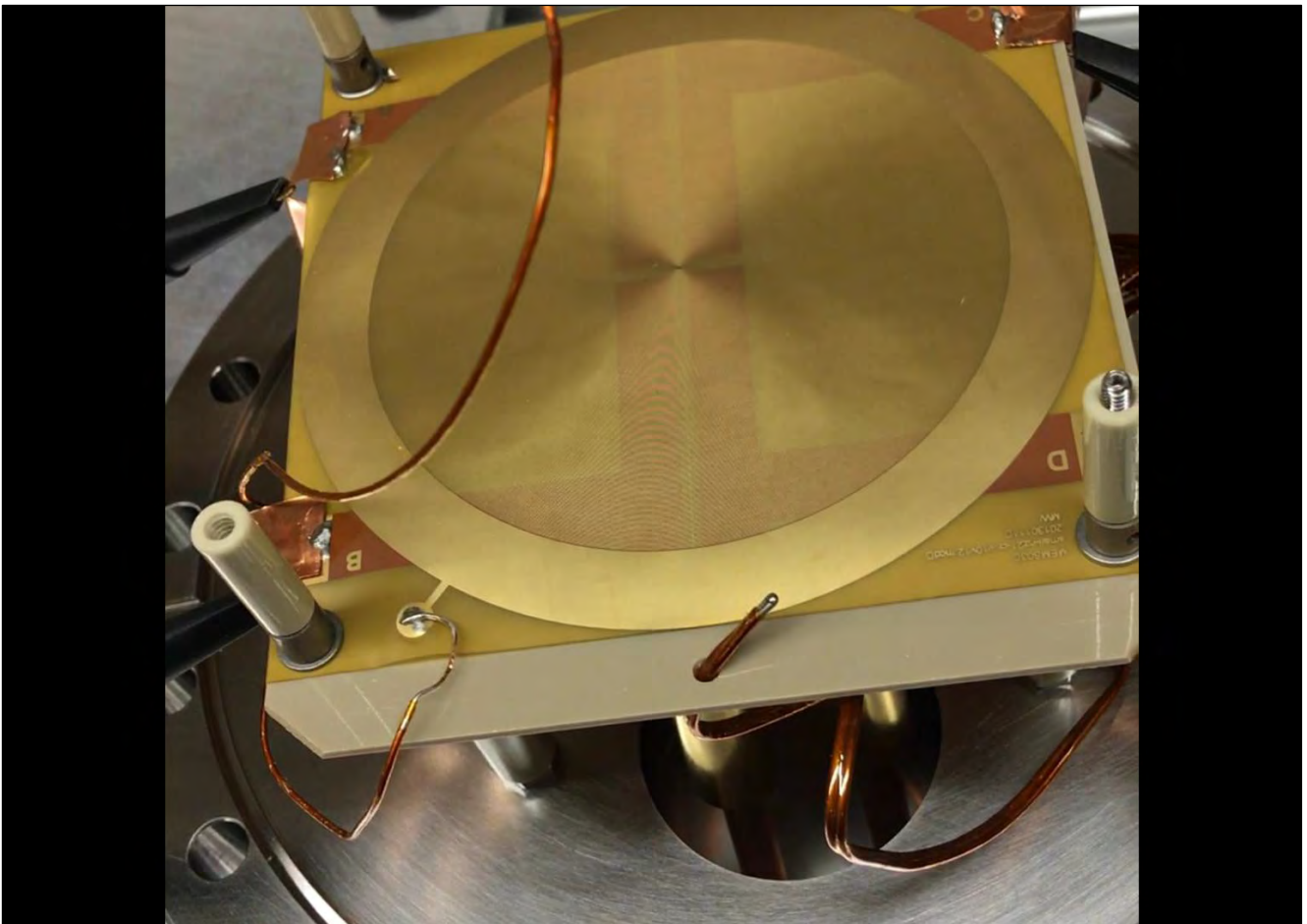
This project promises to yield new results and better insight into colonial currency making, with a more detailed analysis of the spectra and data taken over the course of this summer. At the end of the project, there will be a physics database of one of the Library's special collections, and a confirmation of historical literature.

Acknowledgements

I would like to thank the Institute for Scholarship in the Liberal Arts, University of Notre Dame, for making this project possible by its support from the Da Vinci Grant. I would also like to thank the College of Science, University of Notre Dame, for hosting the 2017 Physics REU, and its support otherwise in this research endeavor.

The use of RF carpets in Helium gas

Keenan Lambert - July 26, 2017



1. Introduction

The use of Radio-Frequency (RF) carpets in nuclear physics laboratories has been proven to be an effective means of transporting ions. Low energy nuclear physics programs use large RF carpets to transport ions in large volume gas cells. These cells are used to thermalize the fast-radioactive ion beam produced in flight, such that they can later either be used in precision experiment or reaccelerated. Gas cells are usually linear however a circular cyclotron gas stopper as been developed at the National Superconducting Cyclotron Laboratory of MSU. The RF carpets in those gas cells vary in size and design and can either be linear or circular. However, they all serve a similar purpose: to prevent the loss of ions and guide ions to an extraction orifice connecting to an ion guide and a beam line where the ion beam is transported at low energy.

The REU project presented in this report aimed at improving the RF carpet test setup in use at the University of Notre Dame by adding a circuit to allow a traveling wave to be implemented onto the RF carpet in addition to the RF. After this was accomplished the transport efficiency under various conditions was studied.

2. Working principle of a RF carpet

RF Carpets are formed by a series of co-centric conductive rings on which an alternating potential (in the radio-frequency range) is applied with opposite polarity on adjacent rings resulting in a strong repelling force that keeps the ion a certain distance from the carpet. The traditional method of transporting the ions consists of superimposing a potential gradient along the segments to drag the ions towards the desired direction. A more recent method, called ion surfing, replaces the potential gradient with a traveling wave, which is a signal at a lower frequency. The traveling wave is generated by applying a sinusoidal potential phase-shifted by 90 degrees on adjacent electrodes and shown on Figure

1. This figure also shows schematically describes how the combination of both signals results in the repulsion and transport of the ions by the carpet.

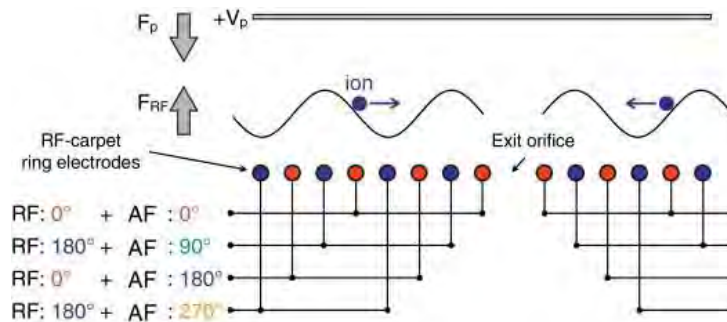


Figure 1: Schematic of a RF carpet used in the “ion surfing” transport method. The two opposite RF phases are indicated by colors red and blue. A plate situated above the carpet and biased at a higher potential V_p brings the ions down to the carpet. From Figure [1].

The RF carpet test setup at Notre Dame is comprised of one such carpet as well as a surface ion source that produces potassium ions. The ions are first attracted by an electric field produced by the potential difference between the ion source and a plate underneath it, which serves as an anode that pulls them out. Then, the voltage difference (V_p in figure 1) between the plate and the carpet creates an electric field, which pushes ions onto the RF carpet. An outer ring electrode around the edge of the carpet is used to collect ions that are transported either using the travelling wave or simply by diffusion. The ions transported are measured as an electrical current. The higher the current, the more ions are being transported. However, some ions will splatter onto the carpet. Finally, if more charge is being dumped on the carpet, it will start to screen the alternating RF field creating more ion loss. The possibility of such *space charge* effect has been studied and will be presented in this report.

3. Generating alternating sin waves

For the travelling wave signal to be transposed onto the RF carpet, it is important to first generate a signal and split it into four different phases and feed them to the corresponding electrodes (see figure 1). As shown in figure 1 each phase is shifted by ninety degrees with respect to the phase of the adjacent electrode. As part of my REU project, I created such circuit using a fast-operational amplifier (op-amp), capacitors, resistors, and potentiometers. The zero and 90 degrees LF phases were generated out of a dual output arbitrary function generator (AFG). To produce the 180 and 270 degrees phases, we fed these outputs to a phase inverting op-amp circuit such as the one shown on the left-hand side of Figure 2. The op-amp was also used to increase the amplitude of the signal produced by the AFG. Hence the zero and 180 degree phases were also sent to a non-inverting op-amp circuit like the one on the right-hand side of Figure 2.

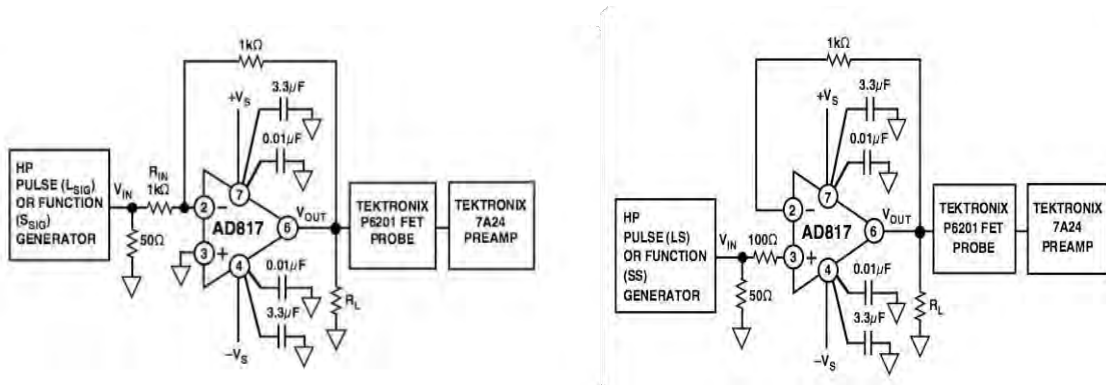


Figure 2: (left) Inverting op-amp circuit and (right) non-inverting op-amp circuit used to produce the traveling waves. Figures from [2].

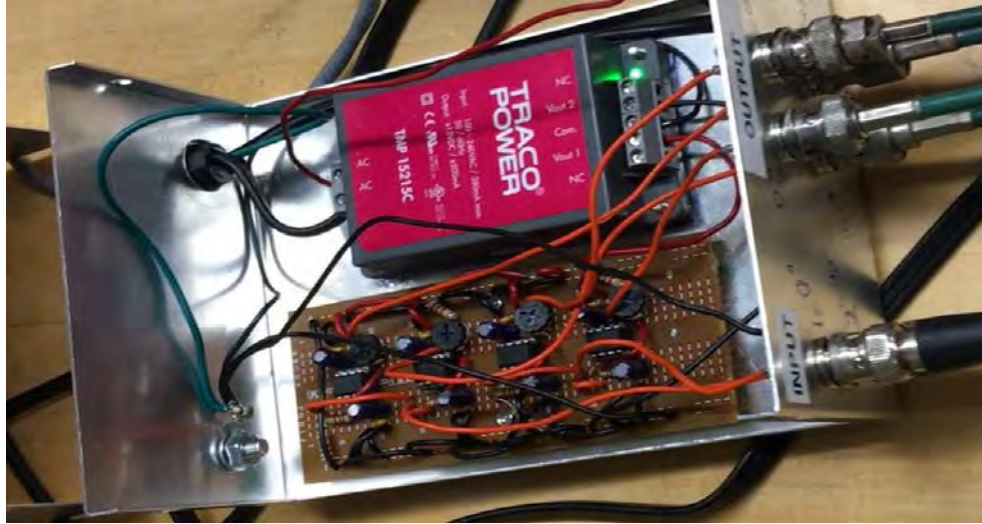


Figure 3: Photo of the op-amp circuitry used to produce the four phases of the traveling wave signal.

The circuit (Figure 3) includes potentiometers to adjust the amplitudes of the low frequency from each op-amp to be equal to each other on the various RF carpet stripes, and to compensate for any unforeseen surges from the RF signal.

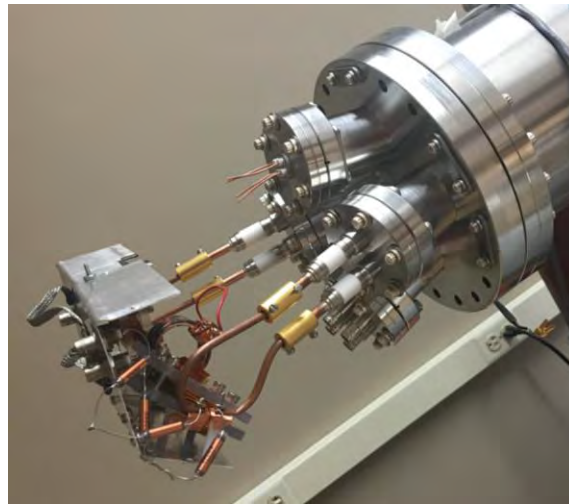


Figure 4: Photo of the of the new RF circuit that combines the RF signal with the traveling wave connected to the ultra-high vacuum feedthroughs that leads to the RF carpet inside the vacuum chamber.

Finally, the RF signal, provided by an RF amplifier, had to be impedance-matched to a resonant circuit in which the RF carpet is the conductive part. This was accomplished using a transformer with only one turn of a copper tube on the secondary side and 9 turns of copper wire on the primary side. The secondary part of the circuit also naturally creates the 0 and 180 phases of the RF signal. In order to combine the RF signal with the traveling wave, we had to add capacitors for the coupling and inductors to prevent the RF from leaking toward the AFG providing the wave signal. Figure 4 shows a photo of the new circuit.

4. Testing the carpet for efficiency

There are many parameters that can be changed to study the transport efficiency of an RF carpet. These include: the RF amplitude and frequency, the travelling wave amplitude and frequency, the electric field pushing the ions to the carpet, the gas pressure, the ion current, and the mass of the ion. In our study, however, several parameters were held fixed: we used a gas pressure of 60 mbar, potassium ions, and a RF of 12.3 MHz. Hence, only the RF amplitude, the ion beam current, and the wave amplitude and frequency were varied.

The efficiency was determined by dividing the total current going to the carpet by the current transported all the way to the outer ring. The total amount of current hitting the carpet in the absence of RF and travelling wave was measured directly using a high-precision electrometer that can measure sub-pA. Throughout our studies we kept the current hitting the carpet to be 100 ± 1 pA. This was achieved by changing the ion source potential for a given voltage on the plate above the carpet.

5. Experimental Results

The effects of varying the RF amplitude for different wave speeds is shown in Figure 5. As the amplitude of the traveling wave V_w increases, there is a noticeable drop in efficiency. This is especially

true when V_w is increased from 3V to 5V, when a large drop in efficiency is observed. This could be attributed to the ions getting closer to the carpet as V_w increases, resulting in more of them hitting the carpet due to collision with helium atoms. The efficiency is also increasing with larger RF amplitude (given here in terms of the RF generator gain in %). This is because at low RF amplitude the ion is less affected by the oscillating potential that kicks it away from the carpet, resulting in a lower transport efficiency. Finally, it is interesting to observe how at low RF amplitudes, having a traveling wave is mandatory to observe transport efficiency. This might be due to the traveling wave being able to carry the ions faster along the carpet, hence reducing the chances of a collision that would direct them towards the carpet.

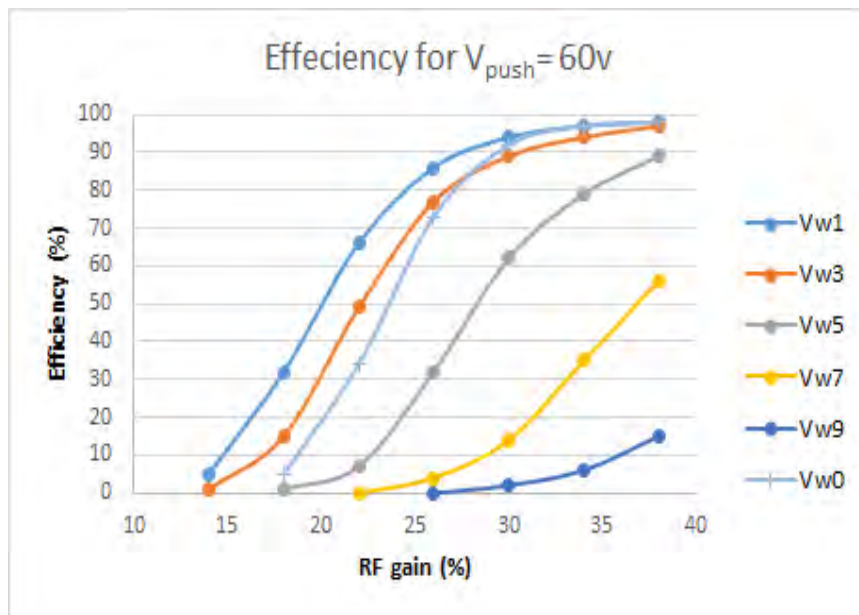


Figure 5: Variation of the RF carpet transport efficiency as a function of the gain of the RF generator used for a 10 kHz wave and a potential of 60 V on the plate. The curves of different colors indicate the amplitude of the traveling wave used. e.g. Vw1 is related to a 1 V wave and Vw0 to no wave.

The graph in Figure 6 illustrates how the RF carpet is able to maintain efficiency at higher V_w amplitudes when the frequency of the V_w is also increased. The higher frequency carries the ions faster above the carpet, allowing a larger V_w to be used.

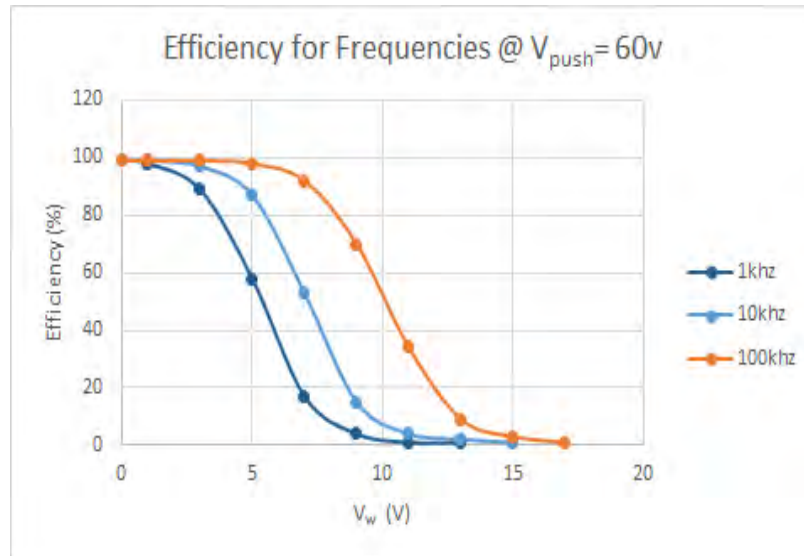


Figure 6: Variation of the RF carpet transport efficiency as a function of the traveling used for 38% gain and a potential of 60 V on the plate. The curves of different colors indicate the frequency of the traveling wave used.

Figure 7 shows how the electric field pushing the ions from the source has an effect on the transport efficiency. As the plate potential is increased, the ions feel a stronger force F_p pushing them towards the carpet (see Figure 1). At a certain point the repelling force from the RF carpet F_{RF} cannot sustain it anymore and a loss in efficiency is observed. We also looked at the effect of increasing the ion beam current hitting the carpet from 10 pA up to 1 nA. Having a traveling wave of 3 V has a positive effect on the efficiency for 10pA, 100pA, and 1000pA currents. Increasing the ion source current from 100 pA to 1000 pA does not seem to have an effect on the transport efficiency. The

efficiency at 10 pA appears to be lower, but it should be noted that there is also a larger uncertainty due to the measurement process.

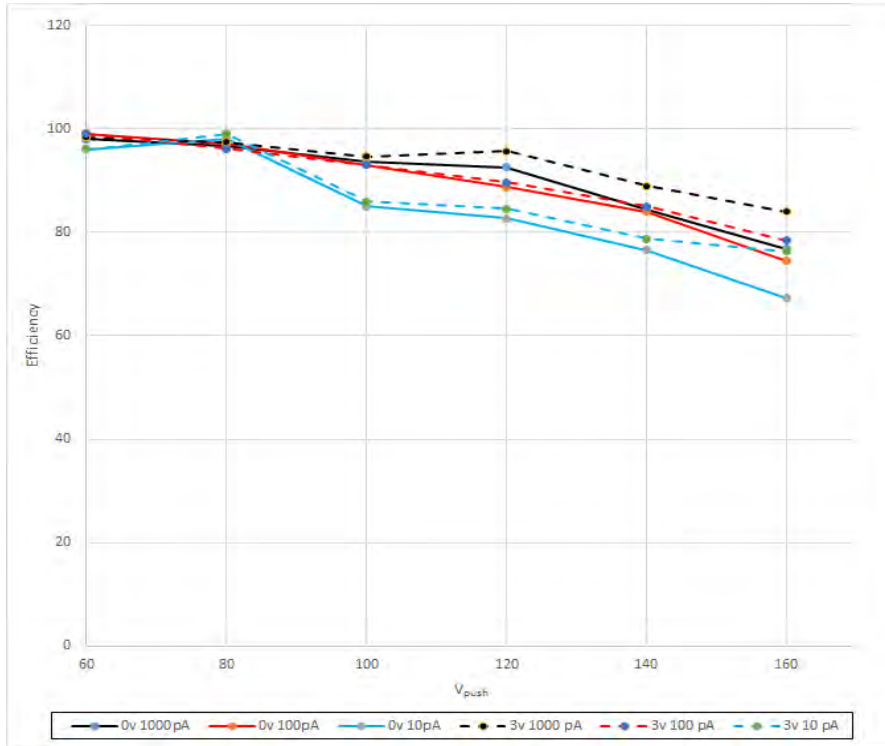


Figure 7: Variation of the RF carpet transport efficiency as a function of the potential on the plate for 38% gain and a 100 kHz wave. The curves of different colors indicate the ion beam current hitting the carpet. The solid lines are without a traveling wave while the dashed lines are for a 3V wave.

6. Conclusion

As part of this REU project a circuitry was developed to produce a traveling wave that can be applied on the RF carpet of the University of Notre Dame RF carpet test chamber. The RF circuitry was also updated to allow for the coupling of the traveling wave to the RF carpet. We observed that the application of a traveling wave with a non-zero amplitude V_w imposed on top of the RF signal does

improve the transport efficiency. The transport efficiency was always observed to be better if a low amplitude traveling wave is used rather than no wave. For potential on the plate exceeding 100 V it appears to be mandatory to implement a traveling wave in order to transport ions. It is possible to transport ions efficiently at larger wave amplitude under the condition that the frequency of the wave is also increased. In order to utilize the full potential of RF carpets we must use the highest RF amplitude below the discharge limit, a plate potential of less than 100V, and a frequency for the traveling wave greater than or equal to 100kHz. With these conditions satisfied it has been observed that the RF carpet can transport ions via the ion surfing method with near perfect efficiency independently of the incoming beam current.

References

[1]. F. Arai, Y. Ito, M Wada, P. Schury, T. Sonoda, H. Mita. *Investigation of the ion surfing transport method with a circular rf carpet, Int. J. of mass spectrom.* **362**, 56 (2014)

[2] <http://studylib.net/doc/11672895/a-high-speed--low-power-wide-supply-range-amplifier-ad817> and <http://studylib.net/doc/11672895/a-high-speed--low-power-wide-supply-range-amplifier-ad817>